



THE HONG KONG  
POLYTECHNIC UNIVERSITY

香港理工大學

Pao Yue-kong Library

包玉剛圖書館

---

## Copyright Undertaking

This thesis is protected by copyright, with all rights reserved.

**By reading and using the thesis, the reader understands and agrees to the following terms:**

1. The reader will abide by the rules and legal ordinances governing copyright regarding the use of the thesis.
2. The reader will use the thesis for the purpose of research or private study only and not for distribution or further reproduction or any other purpose.
3. The reader agrees to indemnify and hold the University harmless from and against any loss, damage, cost, liability or expenses arising from copyright infringement or unauthorized usage.

### IMPORTANT

If you have reasons to believe that any materials in this thesis are deemed not suitable to be distributed in this form, or a copyright owner having difficulty with the material being included in our database, please contact [lbsys@polyu.edu.hk](mailto:lbsys@polyu.edu.hk) providing details. The Library will look into your claim and consider taking remedial action upon receipt of the written requests.

**AN ADAPTIVE DEGREES-OF-FREEDOM  
MULTI-PHYSICS NUMERICAL MODEL FOR  
ANALYSIS AND DESIGN OF NANOFUID-  
FILLED POWER TRANSFORMERS**

**ZHANG YUNPENG**

**PhD**

**The Hong Kong Polytechnic University**

**2019**



The Hong Kong Polytechnic University  
Department of Electrical Engineering

An Adaptive Degrees-of-freedom Multi-Physics  
Numerical Model for Analysis and Design of Nanofluid-  
filled Power Transformers

ZHANG Yunpeng

A thesis submitted in partial fulfillment of the requirements  
for the degree of Doctor of Philosophy

May 2019

## **Certificate of Originality**

I hereby declare that this thesis is my own work and that, to the best of my knowledge and belief, it reproduces no material previously published or written, nor material that has been accepted for the award of any other degree or diploma, except where due acknowledgement has been made in the text.

---

Name: ZHANG Yunpeng

Dated: 01/05/2019

*Abstract of dissertation entitled:*

**An Adaptive Degrees-of-freedom Multi-Physics Numerical Model for Analysis and Design of Nanofluid-filled Power Transformers**

*submitted*

by ZHANG Yunpeng

*for the degree of Doctor of Philosophy in*

Electrical Engineering

*at The Hong Kong Polytechnic University in (05/2019)*

**Abstract**

Power transformer is one of the key equipment in power systems, and higher requirements on the capacity, efficiency, size, and stability are generated from the utilities. An accurate and efficient design process, especially the thermal design, is crucial to fulfill these requirements. In order to tackle the existing problems in transformer cooling, the transformer analysis and design methods are investigated along with the application of a novel coolant, namely, nanofluid.

An adaptive degrees-of-freedom (DoFs) finite element method (FEM) solver is developed for the 3-dimensional (3D) coupled magneto-thermal field analysis, which is based on the independent solvers for the magnetic field and thermal field. In the adaptive DoFs FEM, the system size reduction is realized by eliminating the redundant DoFs from the unknown list rather than removing the corresponding nodes, which is adopted in conventional adaptive FEMs. Hence the rearrangement of mesh data and the storage space for the former mesh are avoided. The slave-master technique is employed in the elimination process in combination with the constraint proposed for 3D field. One set of FEM mesh is used in the coupled magneto-thermal analysis to build the finite element (FE) spaces for these two fields, and the DoFs in each field are adjusted separately according to the field's requirement in discretization. Hence, the different discretization requirements of these two fields are met with one set mesh, and the mapping algorithms for different meshes are no longer required. Several numerical

examples are solved to showcase the effectiveness of this method in terms of efficiency and accuracy.

Excessive temperature rises of hot-spots, which are commonly located in the windings, accelerate the aging of insulating materials and reduce the transformer service life. In addition, the electrification of oil is exacerbated by the increased flow velocity. The novel coolant, i.e. nanofluid, has the potential to reduce the hot-spot temperature rise by improving the thermal conductivity. In order to apply the nanofluid in transformer cooling, the convective heat transfer of oil/SiC nanofluid in disc-type transformer windings is numerically investigated. The computational fluid dynamics (CFD) model and numerical method used in the study are validated with the existing results of oil cooled transformer windings. One pass of the winding is modelled numerically, in which two different inlet position are concerned. It is the first time to use the multi-phase mixture model to analyze such a nanofluid flow. In addition, the single-phase model is also employed for mutual authentication and comparison. Although the effects that the oil/SiC nanofluid of 1% concentration has on the flows in passes of different inlet positions vary, comprehensive temperature drop over these two types of passes is observed after adding the nanoparticles. For the pass with inlet in the internal vertical duct, the ameliorative mass flow rate distribution further improves the heat transfer performance. In addition, the relation between the volume fraction of nanoparticles and the effect on the thermal and fluidic field is positive. To further investigate the nanofluid flow in disc-type transformer windings, a numerical mode is built for the entire winding with four passes. The results show that there is an overall reduction on the disc average temperature after adding nanoparticles, and the temperature distribution along the passes is maintained. It can be concluded that the heat transfer improvement after using nanofluid is mainly produced by the enhanced thermal conductivity, and the mass flow rate distribution changes produce the inhomogeneous temperature reduction of discs. In addition, the lower coolant temperature enhances the effect of nanofluid in the fourth pass.

Since the numerical analysis process is exceedingly time-consuming, a response surface optimization method is proposed to improve the efficiency of oil-immersed

transformers cooling system design. Based on the accurate CFD modeling and the central composite design method, surrogate models, which are used to replace the initial CFD model in the optimization, are produced by these two adopted response surface methods, namely, the Kriging method and the second order polynomial method. Refinement points are gradually added into the set of design points until the derived surrogate models meet the predefined criterion. The surrogate model obtained with the Kriging method, which is validated to be more accurate, is adopted in the response surface optimization process, and the direct optimization method combined with the CFD model is also adopted for comparison. An oil-immersed transformer optimization problem is employed to showcase the effectiveness of this proposed optimization method, in which roughly 40% of the computational resources used in the direct optimization method are saved by the proposed method.

## List of Publications

### Journal Papers:

- [1] **Yunpeng Zhang**, Siu-lau Ho, and Weinong Fu\*, "Applying response surface method to oil-immersed transformer cooling system for design optimization," *IEEE Trans. Magn.*, vol. 54, no. 11, Nov. 2018, pp. 8401705, 1-5.
- [2] **Yunpeng Zhang**, Siu-lau Ho, and Weinong Fu\*, "Heat transfer comparison of nanofluid filled transformer and traditional oil-immersed transformer," *AIP Advances*, no. 8, 2018, pp. 056724, 1-5.
- [3] **Yunpeng Zhang**, Siu-lau Ho, and Weinong Fu\*, "A dynamic multi-level optimal design method with embedded finite-element modeling for power transformers," *AIP Advances*, no. 8, 2018, pp. 056610, 1-6.
- [4] **Yunpeng Zhang**, Siu-lau Ho, Weinong Fu\*, and Huihuan Wu, "An adaptive degrees-of-freedom finite element method for 3-D nonlinear magneto-thermal field analysis," *Numer. Heat Tr. A-appl.*, vol. 75, no. 8, Apr. 2019, pp. 523-532.
- [5] **Yunpeng Zhang**, Siu-lau Ho, Weinong Fu\*, Xinsheng Yang, and Huihuan Wu, "Numerical study on natural convective heat transfer of nanofluids in disc-type transformer windings," *IEEE Access*, vol. 7, 2019, pp. 51267-51275.
- [6] Xinsheng Yang, S. L. Ho, Weinong Fu\*, **Yunpeng Zhang**, Guizhi Xu, Qingxin Yang et al., "An adjustable degrees-of-freedom numerical method for computing the temperature distribution of electrical devices," *Electr. Eng.*, 2019, pp. 1-10.
- [7] **Yunpeng Zhang**, Siu-lau Ho, Weinong Fu\*, and Xinsheng Yang, "3-D nonlinear magnetic field analysis using adaptive degrees-of-freedom finite element method," *IET Sci. Meas. Technol.*, under revision.

### Conference Papers:

- [1] **Yunpeng Zhang**, Siu-lau Ho, and Weinong Fu\*, "Optimization of cooling ducts in nanofluid-filled power transformer windings," in *Proc. APMRC*, Shanghai, China, Jan. 2019, pp. 1-2.

## Acknowledgements

I would like to express my heartfelt gratitude to my supervisors, Prof. Siu-lau Ho and Prof. Weinong Fu, for their continuous guidance, generous encourage and endless support in the past three years. I have learnt a lot from my supervisors, endeavor in career, devotion to research, attitude towards life, and the experience will benefit me for my whole life. I am forever grateful to both of them.

Secondly, I would like to thank all the group members in Applied Electromagnetic Laboratory, Dr. Shuangxia NIU, Dr. Yanpu Zhao, Dr. Longnv li, Dr. Gaojia Zhu, Dr. Lei Liu, Dr. Wei Li, Dr. Ningning Chen, Dr. Xiaoyu Liu, Huihuan Wu, Wenjia Yang, Xinsheng Yang, Yiduan Chen, Dr. Yulong Liu, Qifang Lin, Yue Ma, Yuan Mao, Yiming Shen, Dr. Tiantian Sheng, Sigao Wang, Dr. Yuncong Wang, Xu Weng, Dr. Hui Yang, Xing Zhao for their valuable inspirations and suggestions. My thanks are extended the Department of Electrical Engineering.

Finally, I want to convey my deepest thanks to my family: thank you so much for understanding and supports for my academic pursuit. I would like to thank my parents, Lihe Zhang and Yijun Feng, for bring me to life, raising me up, and endless love. I would like to thank my sister Lingyan Zhang and brother-in-law Fei Mo for their constant support and assistance. Special thanks to my wife Xie Pan for her precious love, company, understanding, and support, which I could never fully repay.

This study was supported by the Research Grant Council of the Hong Kong SAR Government under projects PolyU 152118/15E.

## Table of Contents

Abstract.....	I
List of Publications.....	IV
Acknowledgements.....	V
Table of Contents.....	VI
List of Figures.....	VIII
List of Tables.....	XI
Chapter 1 Introduction.....	1
1.1 Background and Motivation of the Thesis.....	1
1.2 Research Objectives and Contributions.....	4
1.3 Thesis Organization.....	4
1.4 References-Part A.....	5
Chapter 2 Literature Review.....	12
2.1 The FEM for Low-frequency Electromagnetic Problems.....	12
2.1.1 Maxwell Equations.....	12
2.1.2 The $A - \varphi$ Formulation for the Eddy Current Problems.....	13
2.1.3 The Galerkin Finite Element Method.....	19
2.1.4 Calculation of the Element Matrices.....	30
2.1.5 Handling Nonlinear Materials.....	34
2.1.6 Numerical examples.....	36
2.2 The FEM for Thermal Field Analysis and Coupled Magneto-Thermal Field Analysis.....	38
2.2.1 Thermal Field Analysis.....	38
2.2.2 Coupled Field Analysis.....	41
2.3 The Analysis and Design of Power Transformers.....	44
2.3.1 The Analysis of Power Transformers.....	44
2.3.2 Power Transformer Design Optimization.....	50
2.4 Literature Review of Nanofluid.....	52
2.5 Summary.....	57
2.6 Reference-Part B.....	57
Chapter 3 The Adaptive Degrees-of-Freedom Finite Element Method.....	67
3.1 Introduction to Adaptive Finite Element Method.....	67
3.2 The Adaptive DoFs FEM for 3D Nonlinear Magnetic Field Analysis.....	69
3.2.1 The Proposed Constraint.....	70
3.2.2 Adaptive DoFs Adjustment.....	74
3.2.3 Numerical Examples.....	76
3.3 The Adaptive DoFs FEM for Thermal and Magneto-Thermal Field Analysis.....	82
3.3.1 The Extension of Adaptive DoFs FEM.....	82
3.3.2 Numerical Examples.....	83
3.4 Summary.....	88
3.5 Reference-Part C.....	89
Chapter 4 Convective Heat Transfer of Nanofluids in Transformers.....	93

4.1 Introduction to the Heat Transfer in Transformer.....	93
4.2 Numerical Study for One Pass of the Winding .....	95
4.2.1 The Numerical Model .....	95
4.2.2 The Nanofluid Model .....	98
4.2.3 The Validation of Numerical Model and the Grid Independence Study.....	101
4.2.4 Results and Discussion.....	104
4.3 Numerical Study for the Entire Winding.....	112
4.3.1 The Numerical Model .....	112
4.3.2 Results and Discussion.....	113
4.4 Experiment Study for the Nanofluid-filled Transformer.....	117
4.5 Summary .....	118
4.6 Reference-Part D.....	119
Chapter 5 A Response Surface Optimization Method for Oil-immersed Transformer Cooling System Design.....	122
5.1 Introduction to the Optimization Methods Applied in Power Transformers Cooling System Design .....	122
5.2 The Response Surface Optimization Method.....	124
5.2.1 CFD Modeling.....	124
5.2.2 RSM and Optimization.....	127
5.2.3 Solutions of the Original Transformer.....	129
5.2.4 Analysis of RSMs and Optimization Results .....	131
5.3 Summary .....	133
5.4 Reference-Part E .....	134
Chapter 6 Conclusion and Future Work.....	136
6.1 Conclusion.....	136
6.2 Future Work.....	137

# List of Figures

## Chapter 2:

Fig. 2.1. A typical computational domain for eddy current problems.....	14
Fig. 2.2. The tetrahedron element.....	30
Fig. 2.3. (a) The geometry of the solenoid with an air core. (b) The magnetic vector potential derived by the FEM.....	37
Fig. 2.4. The magnetic flux density along the axis of the air core.....	37
Fig. 2.5. The coupled magneto-thermal field analysis.....	42
Fig. 2.6. Front view of the transformer.....	45

## Chapter 3:

Fig. 3.1. The edge classification and the recursive refinement by bisecting (a) the diagonal, (b) one of the face diagonals and (c) one of the edges.....	75
Fig. 3.2. The magnetic flux density along the axis of the air core.....	79
Fig. 3.3. The geometry of TEAM problem 20.....	79
Fig. 3.4. (a) The magnetic flux density and (b) the vector potential derived with the adaptive DoFs FEM.....	80
Fig. 3.5. The geometry of TEAM workshop problem 7.....	80
Fig. 3.6. Z-components $B_z$ of magnetic flux densities along the line A1-B1.....	81
Fig. 3.7. The eddy current density in the aluminum plate at time instant $t$ .....	81
Fig. 3.8. The geometry and temperature of the cylinder.....	84
Fig. 3.9. The convergence curve of the calculated copper loss.....	85
Fig. 3.10. The magnetic flux density obtained by the coupled analysis.....	86
Fig. 3.11. The temperature of (a) the yoke, (b) the center pole and (c) the coil.....	86
Fig. 3.12. Z-components $B_z$ of magnetic flux densities along the line A1-B1 (coupled).....	87
Fig. 3.13. The temperature contours of the aluminum plate at time instant $t$ .....	88
Fig. 3.14. The eddy current density in the aluminum plate at time instant $t$ (coupled).....	88

## Chapter 4:

Fig. 4.1 The model of one pass of the low-voltage windings.....	96
Fig. 4.2. The temperature contours of the referenced winding.....	101
Fig. 4.3. The mass flow rate distribution of the referenced winding.....	102
Fig. 4.4. (a) The temperature contours of the pass with inlet on the outer vertical duct and part of the mesh. (b) The temperature contours of the pass with inlet on the inner vertical duct.....	103
Fig. 4.5. The flow and temperature distribution for these two passes.....	104
Fig. 4.6. (a) The maximum temperature-rise reduction and (b) relative mass flow rate increment for the pass with inlet on the outer vertical duct and nanofluid cooling....	105
Fig. 4.7. (a) The distribution of nanoparticles volume fraction and (b) temperature contours derived by the mixture model for the pass with inlet on the outer vertical duct and nanofluid cooling.....	106
Fig. 4.8. Pressure drop of nanofluids in different volume fraction.....	108
Fig. 4.9. (a) The maximum temperature-rise reduction and (b) relative mass flow rate increment for the pass with inlet on the inner vertical duct and nanofluid cooling...	109
Fig. 4.10. (a) The maximum temperature-rise reduction and (b) relative mass flow rate increment for the pass with inlet on the outer vertical duct and cooled by nanofluids in different volume fraction.....	110
Fig. 4.11. (a) The maximum temperature-rise reduction and (b) relative mass flow rate increment for the pass with inlet on the inner vertical duct and cooled by nanofluids in different volume fraction.....	111
Fig. 4.12. The configuration of the low-voltage winding.....	113
Fig. 4.13. The Contours of the temperature of the winding cooled by nanofluid.....	114
Fig. 4.14. The average disc temperature cooled by transformer oil and nanofluid.....	115
Fig. 4.15. The normalized mass flow rate through the horizontal ducts.....	115
Fig. 4.16. The area-weighted average heat transfer coefficient of nanofluid cooling and its change relative to oil cooling.....	116

Fig. 4.17. The detailed mass flow rate at the joints of passes.....	116
Fig. 4.18. The experiment set up for a nanofluid-filled transformer.....	117
Fig. 4.19. The locations of thermocouples.....	117

## **Chapter 5:**

Fig. 5.1. The CFD model of the oil-immersed transformer.....	125
Fig. 5.2. Mesh of (a)core, windings, and (b) oil.....	126
Fig. 5.3. The calculated residuals and temperature at origin.....	129
Fig. 5.4. The calculated temperature of active parts with (a) the first mesh, (b) the second mesh, and (c) the last mesh.....	130
Fig. 5.5. Goodness of fit for (a) the initial SOP model, (b) the final SOP model, (c) the initial Kriging model (d) the final Kriging model.....	132

# List of Tables

## Chapter 3:

Table 3.1. Neighboring information for the master nodes.....	72
Table 3.2. The MVP at master nodes and the constraint coefficients.....	73
Table 3.3. Error analysis of these two constraints.....	74
Table 3.4. The convergence test for mesh refinement algorithm.....	77
Table 3.5. Error analysis of these two constraints in the second example.....	78
Table 3.6. Comparison of the temperature for three fixed points.....	84
Table 3.7. The parameters in the fourth example.....	85

## Chapter 4:

Table 4.1. Material properties.....	98
Table 4.2. Mass Flow Rate Distribution.....	107

## Chapter 5:

Table 5.1. Material properties.....	125
Table 5.2. Details of the mesh.....	126
Table 5.3. Error analysis of the surrogate models.....	131
Table 5.4 Optimized solutions.....	132



# Chapter 1 Introduction

## 1.1 Background and Motivation of the Thesis

Electromagnetic devices, such as generators, transformers, power electronics, motors and so on, build the modern energy conversion system. With the advancement of industry and the improvement of environmental awareness, increasing requirements are raised on the performance of electromagnetic devices. In China, ultra-high voltage (UHV) power transmission is constructed to connect the energy resources in the northern and western areas with the power utilization in the central and eastern areas [A1]. Large capacity power transformers with high insulation level and good cooling performance are needed to fulfill the practical application. In addition, miniaturization is the major concern for transformers used in downtown. In order to meet these targets, both electromagnetic design and thermal design should be included in the design process [A2].

With the advantages in convenience and efficiency, analytical equations based design methods are widely used in the transformer industry in combination with empirical coefficients [A3-A5]. Computer was introduced into the transformer design for the first time in 1955 [A6], followed by many studies on computer aided transformer design [A7-A12]. The manufacturing cost and the operating cost are two common objective functions for transformer design[A3], while the obtained optimal design should satisfy the utility's requirements and the transformer standards, such as *ANSI/IEEE* standards, *CENELEC* standards, and *IEC* standards. In order to achieve the best utilization of existing materials, optimization algorithms are employed in the design process. Several optimization methods, such as geometric programming [A13], genetic algorithm [A14-A16], neural network [A17, A18], gamma differential evolution approach [A19] and so on [A20-A22], are applied in the transformer design

optimization (TDO). According to the number of object functions, optimization algorithms are classified into two categories, the single-objective optimization method and the multi-objective optimization method.

Benefitting from the advancement of computer technology and simulation tools, it is common to conduct a numerical analysis of one separate field in transformers to derive the electromagnetic or thermal performance [A3]. The finite element method (FEM), which was applied to solve the electromagnetic field since 1960s [A23], is the dominant algorithm in low-frequency electromagnetics. Potentials are introduced to transform the Maxwell equations to facilitate the computation, and the generated formulations are classified to the magnetic vector potential (MVP) formulation [A24-A29] and the magnetic scalar potential (MSP) formulation [A30-A36]. Compared with the MVP formulations, the number of unknowns in the MSP formulations are dramatically reduced. However, complicated treatments are required for MSP formulations when solving eddy current problems with multiply-connected conductors [A35-A38]. The nonlinear materials can be handled with the Newton-Raphson (NR) method, and the resulted sparse linear system is solved by linear solvers, such as Pardiso solver and ICCG solver. Similarly, several numerical methods, such as the finite difference method (FDM) and the FEM, are applied to solve the heat conduction problem of thermal field [A39, A40]. In addition, co-simulation for the coupled magneto-thermal field was introduced to the analysis and design of transformers to obtain a more accurate solution [A2, A41, A42], while the computational burden is increased dramatically. Two common coupling strategies are adopted for the magneto-thermal field analysis. The first strategy is generating a sufficiently refined mesh for both fields, and two meshes are generated separately for each field in the other strategy [A43]. Additional mapping algorithms are needed for two different meshes, while unnecessary cost of computational resources is produced in the first strategy [A44, A45].

Since analytical equations have poor accuracy and extensibility, FEM was introduced to the design process to validate the performance estimated by analytical equations [A46, A47] or to compute some parameters, such as no-load losses [A48]

and load losses [A49]. Limited by the computational resources, TDO fully based on numerical models is very rare [A50, A51], and the design process is exceedingly time-consuming. In the numerical analysis tools, the device to be designed is parameterized, and the design variables values are changed according to the feedbacks from optimization algorithms. To improve the optimization efficiency, response surface methods are introduced into the optimization process to generate a surrogate model to replace the numerical model [A52].

In addition to improving the comprehensive utilization of materials with optimization algorithms, the development of new materials, which may have superior properties compared to existing materials, is critical. The concept of enhancing the thermal conductivity of liquid by adding solid particles with high thermal conductivity, which was proposed in 1873 by Maxwell, was realized with nanoparticles in 1995 [A53]. For this reason, this type of multi-phase mixture is named as nanofluid. Several types of transformer oil based nanofluids are prepared and measured [A54-A56], and it is reported that the thermal conductivity is improved dramatically after dispersing nanoparticles, which indicates the potential application in transformer cooling. The nanofluid flows in simple containers are investigated numerically and experimentally [A57-A60], and models are proposed to estimate or predict the nanofluid properties [A61]. In addition, the multi-phase model and the single-phase model are used in the numerical study to investigate the nanofluid flow, and the multi-phase model is reported to be more accurate [A58-A60].

In the challenges involved to improve the transformer cooling performance, this thesis mainly focuses on numerical method, design algorithm and the application of nanofluid. For real-life engineering optimization problems with many design parameters, the design points needed to be estimated with simulation tools are tremendous even with efficient evolutionary algorithms. Moreover, a large scale system may be produced to ensure the accuracy, and highly nonlinear materials may be included in the problem. Hence, the entire transformer design process will be exceedingly time-consuming. Secondly, coupled magneto-thermal field analysis is becoming increasingly critical for the analysis and design of transformers, and the

existing solvers for coupled magneto-thermal field analysis is either time-consuming or complicated. Lastly, most of the former studies of transformer oil based nanofluids were focused on the material properties, and there is no experimental study or numerical analysis on the flow and temperature distribution in nanofluid cooled transformers.

## **1.2 Research Objectives and Contributions**

This study focuses to tackle the existing problems of transformer cooling through proposing efficient analysis and design methods, and applying the novel coolants, i.e. nanofluids, in the transformer cooling system. The contributions of this study are:

- 1) An adaptive degrees-of-freedom (DoFs) FEM solver is developed for the 3-dimensional (3D) nonlinear magnetic field analysis with the objective oriented C++ programming language, and this method is then extended to solve the heat conduction problem of thermal field.
- 2) Based on the adaptive DoFs FEM, a coupled solver is developed for the magneto-thermal field analysis. One set of FEM mesh is used for both fields, while meeting the different discretization requirements.
- 3) A response surface optimization algorithm is proposed for the transformer cooling system optimization, in which the numerical model of transformer built with computational fluid dynamics (CFD) tools is included.
- 4) The natural convective heat transfer of nanofluid-filled transformer windings is numerically studied with the 2-dimensional (2D) models of one pass and the entire winding.

## **1.3 Thesis Organization**

The remainder of this thesis is organized in the following manner. Chapter 2

reviews the computational electromagnetics, the computational heat conduction, and the coupled analysis of these two fields. Detailed discretization equations of the governing equations derived by the FEM are given in this chapter. In addition, the analysis and design methods of power transformers are introduced along with the transformer oil based nanofluid. In Chapter 3, the adaptive DoFs FEM is introduced and is developed to solve the 3D nonlinear magnetic field, thermal field, and coupled magneto-thermal field. The natural convective heat transfer of nanofluid-filled transformer windings is studied with the numerical models of windings in Chapter 4. In Chapter 5, a response surface optimization method, which is proposed for the cooling system design optimization, is presented. Finally, Chapter 6 gives conclusion of this thesis and scope for future work.

## 1.4 References-Part A

- [A1] S. Yinbiao and Z. Wenliang, "Research of key technologies for UHV transmission," *Proceedings of the CSEE*, vol. 27, no. 31, pp. 1-6, 2007.
- [A2] L. N. Li, S. X. Niu, S. L. Ho, W. N. Fu, and Y. Li, "A Novel Approach to Investigate the Hot-Spot Temperature Rise in Power Transformers," *IEEE Trans. Magn.*, vol. 51, no. 3, Mar 2015.
- [A3] E. I. Amoiralis, M. A. Tsili, and A. G. Kladas, "Transformer Design and Optimization: A Literature Survey," *IEEE Trans. Power Del.*, vol. 24, no. 4, pp. 1999-2024, Oct 2009.
- [A4] P. S. Georgilakis, *Spotlight on modern transformer design*. Springer Science & Business Media, 2009.
- [A5] Shenyang Transformer LLC. *Design handbook of oil-immersed power transformer*. Shenyang: Shenyang Transformer LLC, 1999, pp. 162-203.
- [A6] S. B. Williams, P. A. Abetti, and E. F. Magnusson, "How digital computers aid transformer designer," in *Gen. Elect. Rev.*, Schenectady, NY, vol. 58, pp. 24–25, May 1955.

- [A7] S. B. Williams, P. A. Abetti, and E. F. Magnusson, "Application of digital computers to transformer design," *AIEE Trans. Power App. Syst.*, vol. 75, pt. III, pp. 728–735, 1956.
- [A8] W. Sharpley and J. V. Oldfield, "The digital computer applied to the design of large power transformers," *Proc. Inst. Elect. Eng.*, vol. 105, pt. A, pp. 112–125, 1958.
- [A9] S. B. Williams, P. A. Abetti, and H. J. Mason, "Complete design of power transformers with a large size digital computer," *AIEE Trans. Power App. Syst.*, vol. 77, pt. III, pp. 1282–1291, 1959.
- [A10] O. W. Andersen, "Optimum design of electrical machines," *IEEE Trans. Power App. Sys.*, vol. PAS-86, no. 6, pp. 707–711, Jun. 1967.
- [A11] H. H. Wu and R. Adams, "Transformer design using time-sharing computer," *IEEE Trans. Magn.*, vol. MAG-6, no. 1, p. 67, Mar. 1970.
- [A12] P. Odessey, "Transformer design by computer," *IEEE Trans. Manuf. Technol.*, vol. 3, no. 1, pp. 1–17, Jan. 1974.
- [A13] R. A. Jabr, "Application of geometric programming to transformer design," *IEEE Trans. Magn.*, vol. 41, no. 11, pp. 4261–4269, Nov. 2005.
- [A14] L. Hui, H. Li, H. Bei, and Y. Shunchang, "Application research based on improved genetic algorithm for optimum design of power transformers," in *Proc. 5th Int. Conf. Electrical Machines and Systems*, vol. 1, pp. 242–245, 2001.
- [A15] S. Elia, G. Fabbri, E. Nistico, and E. Santini, "Design of cast-resin distribution transformers by means of genetic algorithms," in *Proc. Int. Symp. Power Electronics, Electrical Drives, Automation and Motion*, pp. 1473–1477, 2006.
- [A16] N. Tutkun and A. Moses, "Design optimization of a typical strip-wound toroidal core using genetic algorithms," *J. Magn. Magn. Mater.*, vol. 277, no. 1–2, pp. 216–220, 2004.
- [A17] E. I. Amoiralis, P. S. Georgilakis, T. D. Kefalas, M. A. Tsili, and A. G. Kladas, "Artificial intelligence combined with hybrid FEM-BE techniques for global transformer optimization," *IEEE Trans. Magn.*, vol. 43, no. 4, pp. 1633–1636, Apr. 2007.

- [A18] L. H. Geromel and C. R. Souza, "The applications of intelligent systems in power transformer design," in *Proc. IEEE Canadian Conf. Electrical and Computer Engineering*, 2002, vol. 1, pp. 285–290.
- [A19] L. D. Coelho, V. C. Mariani, M. V. F. da Luz, and J. V. Leite, "Novel Gamma Differential Evolution Approach for Multiobjective Transformer Design Optimization," *IEEE Trans. Magn.*, vol. 49, no. 5, pp. 2121-2124, May 2013.
- [A20] H. V. H. Ayala, L. D. Coelho, V. C. Mariani, M. V. F. da Luz, and J. V. Leite, "Harmony Search Approach Based on Ricker Map for Multi-Objective Transformer Design Optimization," *IEEE Trans. Magn.*, vol. 51, no. 3, Mar 2015.
- [A21] L. D. Coelho, V. C. Mariani, F. A. Guerra, M. V. F. da Luz, and J. V. Leite, "Multiobjective Optimization of Transformer Design Using a Chaotic Evolutionary Approach," *IEEE Trans. Magn.*, vol. 50, no. 2, Feb 2014.
- [A22] H. V. H. Ayala, E. H. D. Segundo, L. Lebensztajn, V. C. Mariani, and L. D. Coelho, "Multiobjective Wind Driven Optimization Approach Applied to Transformer Design," *2016 IEEE Congress on Evolutionary Computation*, pp. 4642-4647, 2016.
- [A23] A. M. Winslow, "Magnetic field calculation in an irregular triangular mesh," Lawrence Radiation Laboratory Report, UCRL-7784-T, Rev. 1, 1965.
- [A24] O. Biro, K. Preis, and K. R. Richter, "On the use of the magnetic vector potential in the nodal and edge finite element analysis of 3D magnetostatic problems," *IEEE Trans. Magn.*, vol. 32, no. 3, pp. 651-654, May 1996.
- [A25] H. Igarashi, and T. Honma, "On convergence of ICCG applied to finite-element equation for quasi-static fields," *IEEE Trans. Magn.*, vol. 38, no. 2, pp. 565-568, Mar. 2002.
- [A26] B. Weiß, and O. Bíró, "On the convergence of transient eddy-current problems," *IEEE Trans. Magn.*, vol. 40, no. 2, pp. 957-960, Mar. 2004.
- [A27] B. Weiß, and O. Bíró, "Multigrid for time-harmonic 3-D eddy-current analysis with edge elements," *IEEE Trans. Magn.*, vol. 41, no. 5, pp. 1712-1715, May 2005.
- [A28] J. Gyselinck, P. Dular, C. Geuzaine, and R. V. Sabariego, "Surface-impedance boundary conditions in time-domain finite-element calculations using the

magnetic vector-potential formulation,” *IEEE Trans. Magn.*, vol. 45, no. 3, pp. 1280-1283, Mar. 2009.

[A29] P. Dular, N. Sadowski, J. P. A. Bastos, and W. Legros, “Dual complete procedures to take stranded inductors into account in magnetic vector potential formulations,” *IEEE Trans. Magn.*, vol. 36, no. 4, pp. 1600-1605, Jul. 2000.

[A30] J. P. Webb, and B. Forghani, “A single scalar potential method for 3D magnetostatics using edge elements,” *IEEE Trans. Magn.*, vol. 25, no. 5, pp. 4126-4128, Sep. 1989.

[A31] J. P. Webb, and B. Forghani, “T-method using hierarchical edge elements,” *IEE Proc. Sci. Meas. Technol.*, vol. 142, no. 2, pp. 133-141, Mar. 1995.

[A32] A. G. Kladas, and J. A. Tegopoulos, “A new scalar potential formulation for 3-D magnetostatics necessitating no source field calculation,” *IEEE Trans. Magn.*, vol. 28, no. 2, pp. 1103-1106, Mar. 1992.

[A33] H. T. Luong, Y. Marechal, and G. Meunier, “Computation of 3-D current driven eddy current problems using cutting surfaces,” *IEEE Trans. Magn.*, vol. 33, no. 2, pp. 1314-1317, Mar. 1997.

[A34] A. T. Phung, O. Chadebec, P. Labie, Y. L. Floch, and G. Meunier, “Automatic cuts for magnetic scalar potential formulations,” *IEEE Trans. Magn.*, vol. 41, no. 5, pp. 1668-1671, May 2005.

[A35] Z. Ren, “T-formulation for eddy-current problems in multiply connected regions,” *IEEE Trans. Magn.*, vol. 38, no. 2, pp. 557-560, Mar. 2002.

[A36] P. Zhou, Z. Badics, D. Lin, and Z. J. Cendes, “Nonlinear T-formulation including motion for multiply connected 3-D problems,” *IEEE Trans. Magn.*, vol. 44, no. 6, pp. 718-721, Jun. 2008.

[A37] P. Dłotko, R. Specogna, and F. Trevisan, “Automatic generation of cuts on large-sized meshes for the T-geometric eddy-current formulation,” *Comput. Methods Appl. Mech. Engrg.*, vol. 198, pp. 3765-3781, 2009.

[A38] R. Specogna, “Optimal cohomology generators for 2-D eddy-current problems in linear time,” *IEEE Trans. Magn.*, vol. 49, no. 4, pp. 1299-1304, Apr. 2013.

- [A39] W. Minkowycz, E. M. Sparrow, G. Schneider, and R. Pletcher, "*Handbook of numerical heat transfer*," New York, Wiley-Interscience, 1988.
- [A40] A. S. Franca and K. Haghighi, "Adaptive Finite-Element Analysis of Transient Thermal Problems," *Numer. Heat Tr. B-fund.*, vol. 26, no. 3, pp. 273-292, Oct-Nov 1994.
- [A41] J. Smolka, O. Biro, and A. J. Nowak, "Numerical Simulation and Experimental Validation of Coupled Flow, Heat Transfer and Electromagnetic Problems in Electrical Transformers," *Arch. Comput. Method E.*, vol. 16, no. 3, pp. 319-355, Sep 2009.
- [A42] C. Liu, J. J. Ruan, W. Wen, R. H. Gong, and C. B. Liao, "Temperature rise of a dry-type transformer with quasi-3D coupled-field method," *IET Electr. Power App.*, vol. 10, no. 7, pp. 598-603, Aug 2016.
- [A43] Magnet & Thermnet, version 7.5, Montreal: Infolytica, May 6, 2014.
- [A44] ANSYS, version 18.2, Pittsburgh: ANSYS, Aug. 2017.
- [A45] Y. J. Zhang, W. N. Qin, and J. J. Ruan, "Variable mapping method with nonmatching meshes in 3-d finite-element analysis of coupled electromagnetic-structural fields," *IEEE Trans. Plasma Sci.*, vol. 43, no. 5, pp. 1288-1292, May 2015.
- [A46] C. Hernandez, M. A. Arjona, and S.-H. Dong, "Object-oriented knowledge-based system for distribution transformer design," *IEEE Trans. Magn.*, vol. 44, no. 10, pp. 2332–2337, Oct. 2008.
- [A47] E. I. Amoiralis, P. S. Georgilakis, M. A. Tsili, and A. G. Kladas, "Global transformer optimization method using evolutionary design and numerical field computation," *IEEE Trans. Magn.*, vol. 45, no. 3, pp. 1720–1723, Mar. 2009.
- [A48] T. D. Kefalas, P. S. Georgilakis, A. G. Kladas, A. T. Souflaris, and D. G. Paparigas, "Multiple grade lamination wound core: A novel technique for transformer iron loss minimization using simulated annealing with restarts and an anisotropy model," *IEEE Trans. Magn.*, vol. 44, no. 6, pp. 1082–1085, Jun. 2008.
- [A49] J. C. Olivares, R. Escarela, S. V. Kulkarni, F. de León, E. MelgozaVasquez, and O. Hernández-Anaya, "Improved insert geometry for reducing tank-wall losses in pad-mounted transformers," *IEEE Trans. Power Del.*, vol. 19, no. 3, pp. 1120–1126, Jul.

2005.

[A50] J. Smolka, "CFD-based 3-D optimization of the mutual coil configuration for the effective cooling of an electrical transformer," *Appl. Therm. Eng.*, vol. 50, no. 1, pp. 124-133, Jan 10 2013.

[A51] J. Smolka and A. J. Nowak, "Shape Optimization of Coils and Cooling Ducts in Dry-Type Transformers Using Computational Fluid Dynamics and Genetic Algorithm," *IEEE Trans. Magn.*, vol. 47, no. 6, pp. 1726-1731, Jun 2011.

[A52] S. R. Cove, M. Ordonez, F. Luchino, and J. E. Quaioco, "Applying Response Surface Methodology to Small Planar Transformer Winding Design," *IEEE Trans. Ind. Electron.*, vol. 60, no. 2, pp. 483-493, Feb 2013.

[A53] S. Choi and J. Eastman, "Enhancing thermal conductivity of fluids with nanoparticles," *ASME-Publications-Fed*, vol. 231, pp. 99-106, 1995.

[A54] C. Choi, H. S. Yoo, and J. M. Oh, "Preparation and heat transfer properties of nanoparticle-in-transformer oil dispersions as advanced energy-efficient coolants," *Curr. Appl. Phys.*, vol. 8, no. 6, pp. 710-712, Oct. 2008.

[A55] S. C. Pugazhendhi, "Experimental evaluation on dielectric and thermal characteristics of nano filler added transformer oil," in *Proc. ICHVE*, Shanghai, China, 2012, pp. 207-210.

[A56] D. L. Liu, Y. X. Zhou, Y. Yang, L. Zhang, and F. B. Jin, "Characterization of High Performance AlN Nanoparticle-Based Transformer Oil Nanofluids," *IEEE Trans. Dielectr. Electr. Insul.*, vol. 23, no. 5, pp. 2757-2767, Oct. 2016.

[A57] V. Bianco, F. Chiacchio, O. Manca, and S. Nardini, "Numerical investigation of nanofluids forced convection in circular tubes," *Appl. Therm. Eng.*, vol. 29, no. 17-18, pp. 3632-3642, Dec. 2009.

[A58] M. Kalteh, A. Abbassi, M. Saffar-Avval, A. Frijns, A. Darhuber, and J. Harting, "Experimental and numerical investigation of nanofluid forced convection inside a wide microchannel heat sink," *Appl. Therm. Eng.*, vol. 36, pp. 260-268, Apr. 2012.

[A59] M. H. Fard, M. N. Esfahany, and M. R. Talaie, "Numerical study of convective heat transfer of nanofluids in a circular tube two-phase model versus single-phase model," *Int. J. Heat Mass Transf.*, vol. 37, no. 1, pp. 91-97, Jan. 2010.

[A60] R. Lotfi, Y. Saboohi, and A. M. Rashidi, "Numerical study of forced convective heat transfer of Nanofluids: Comparison of different approaches," *Int. J. Heat Mass Transf.*, vol. 37, no. 1, pp. 74-78, Jan. 2010.

[A61] Z. Haddad, H. F. Oztop, E. Abu-Nada, and A. Mataoui, "A review on natural convective heat transfer of nanofluids," *Renew. Sust. Energ. Rev.*, vol. 16, no. 7, pp. 5363-5378, Sep 2012.

# Chapter 2 Literature Review

## 2.1 The FEM for Low-frequency Electromagnetic Problems

### 2.1.1 Maxwell Equations

Nowadays, numerical analysis of electromagnetic fields has become a powerful tool for industrial application, such as transformer analysis and design [B1]. The numerical analysis process includes a series of procedures, such as building the numerical model, discretizing the field and the computational domain, solving the resulting algebraic equations, and post-processing the derived results [B2]. The most widely used numerical method in the electromagnetic field analysis is the FEM, which is based on the differential form of Maxwell equations,

$$\begin{cases} \nabla \times \mathbf{H} = \mathbf{J} + \frac{\partial \mathbf{D}}{\partial t} & (a) \\ \nabla \times \mathbf{E} = -\frac{\partial \mathbf{B}}{\partial t} & (b) \\ \nabla \cdot \mathbf{B} = 0 & (c) \\ \nabla \cdot \mathbf{D} = \rho & (d) \end{cases} \quad (2-1)$$

where;  $\mathbf{H}$  is the magnetic field intensity (A/m),  $\mathbf{J}$  is the current density (A/m<sup>2</sup>),  $\mathbf{D}$  is the electric displacement vector (C/m<sup>2</sup>),  $\mathbf{E}$  is the electric field intensity (V/m),  $\mathbf{B}$  is the magnetic flux density (T),  $t$  is the time (s) and  $\rho$  is the charge density (C/m<sup>3</sup>). The second term of the right-hand-side of equation (2-1a) is named as displacement current density, which is generally neglected in the low-frequency electromagnetic field analysis. These four equations are not independent, as the latter two equations can be derived from the first and second equations. Three more constitutive relations are needed for the definite solution of Maxwell equations,

$$\begin{cases} \mathbf{B} = \mu\mathbf{H} & (a) \\ \mathbf{J} = \sigma\mathbf{E} & (b) \\ \mathbf{D} = \varepsilon\mathbf{E} & (c) \end{cases} \quad (2 - 2)$$

where,  $\mu$ ,  $\sigma$ ,  $\varepsilon$  are, respectively, the magnetic permeability, the electrical conductivity, and the permittivity of the dielectric. In addition, the current continuity equation, which is critical for the following numerical computation, can be derived from equation (2 – 1a) and (2 – 1d),

$$\nabla \cdot \mathbf{J} + \frac{\partial \rho}{\partial t} = 0 \quad (2 - 3)$$

In the low-frequency electromagnetic field, the wavelength is much longer than the size of devices, and the field varies instantaneously with the source rather than lagging behind the source. Thus, the displacement current is very small when compared with the conducting current, and it can be ignored in the electromagnetic field analysis for low frequency devices, such as power transformers, electric motors, sensors, induction heating devices and so on. This type of problems, in which the displacement current is neglected, are named as eddy current problems. The governing equations for the eddy current problem can be further modified for specific problems to simplify the computation. Besides, it is quite difficult to solve the Maxwell equations directly, since it involves five vector unknowns. A general pattern is to introduce electric and magnetic potentials to replace the field functions, and there are several types of combinations for these two potentials, such as the MVP ( $\mathbf{A}$ ) form and the MSP or the electric vector potential (EVP,  $\mathbf{T}$ ) form.

### 2.1.2 The $\mathbf{A} - \varphi$ Formulation for the Eddy Current Problems

In eddy current problems, the computational domain is generally divided into two parts, the eddy current free region and the eddy current region [B3]. Components filled with non-conducting material, such as air, insulation, non-conducting ferromagnet, and some special components, in which the eddy current is negligible, are assigned to

the eddy current free region with  $\sigma = 0$ . The corresponding governing equations are given by

$$\begin{cases} \nabla \times \mathbf{H} = \mathbf{J} & (a) \\ \nabla \cdot \mathbf{B} = 0 & (b) \end{cases} \quad (2-4)$$

Other components, including the solid conductors, conducting ferromagnet, and steel structure, are assigned to the eddy current part with  $\sigma > 0$ , and the governing equations are given by

$$\begin{cases} \nabla \times \mathbf{H} = \sigma \mathbf{E} & (a) \\ \nabla \times \mathbf{E} = -\frac{\partial \mathbf{B}}{\partial t} & (b) \\ \nabla \cdot \mathbf{B} = 0 & (c) \end{cases} \quad (2-5)$$

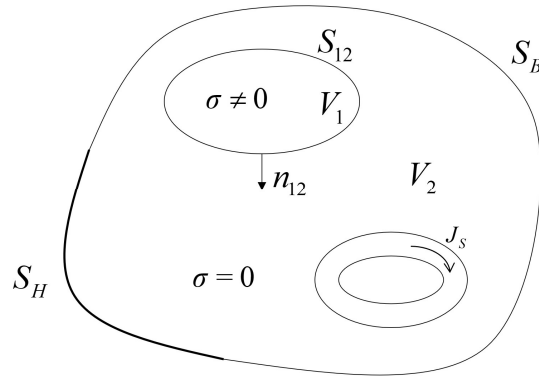


Fig. 2.1. A typical computational domain for eddy current problems.

As shown in Fig. 2.1, a typical computational domain for eddy current problems is divided into two parts, the eddy current region  $V_1$  without source current and the eddy current free region  $V_2$ , which contains the source current. The definite conditions for the differential governing equations are also given, including the decomposed external boundary conditions ( $S_B, S_H$ ) and the internal boundary condition ( $S_{12}$ ). The normal component of the magnetic flux density is predefined on  $S_B$ , and the predefined parameter on  $S_H$  is the tangential component of the magnetic field intensity [B3, B4]. For simplicity, the boundary conditions on  $S_B$  and  $S_H$  are assumed to be homogenous. The internal boundary  $S_{12}$  is the interface between the conducting material and the non-conducting material. Across this interface, the

continuity of the tangential component of the magnetic field intensity and the continuity of the normal component of the magnetic flux density hold. Thus, these three boundary conditions are given as follows:

$$\begin{aligned} \mathbf{B} \cdot \mathbf{n}|_{S_B} &= 0 \\ \mathbf{H} \times \mathbf{n}|_{S_H} &= \mathbf{0} \\ S_{12}: \begin{cases} \mathbf{B}_1 \cdot \mathbf{n}_{12} = \mathbf{B}_2 \cdot \mathbf{n}_{12} \\ \mathbf{H}_1 \times \mathbf{n}_{12} = \mathbf{H}_2 \times \mathbf{n}_{12} \end{cases} \end{aligned} \quad (2-6)$$

Where;  $\mathbf{n}$  is the unit normal vector of boundary  $S$ ;  $\mathbf{n}_{12}$  is the unit normal vector of boundary  $S_{12}$ . For a simple-connected domain with determined initial conditions, the uniqueness of  $\mathbf{B}$  and  $\mathbf{E}$  can be ensured by the equations listed above.

In the 3D eddy current field analysis, there are totally six unknown functions in the electromagnetic field ( $\mathbf{B}$  and  $\mathbf{E}$ ). To reduce the computational effort, different potential formulas, which are derived from the field governing equations, are widely adopted in the numerical analysis of eddy current problems. The potential formulations are classified into two types, the  $\mathbf{A}$  form [B3, B5-B9] and the  $\mathbf{T}$  form [B10-B16]. Generally, the eddy current problem is formulated with the vector potential of one field and the scalar potential of the other field, such as the  $\mathbf{A} - \varphi$  formula and the  $\mathbf{T} - \Omega$  formula. Although the combinations are different from each other, a vector potential and a scalar potential are required to model the eddy current, while either a scalar potential or a vector potential is used for the eddy current free region. Thus, the number of the unknown functions in the eddy current region is four, and it is fixed for each form. The number of the unknown functions in the eddy current free region varies, one for the  $\mathbf{T}$  formula, three for the  $\mathbf{A}$  formula. Therefore, the total unknowns of the  $\mathbf{A}$  formula are much larger than that of the  $\mathbf{T}$  formula. Even though the number of the unknowns involved in the  $\mathbf{A}$  formula is relatively large, the  $\mathbf{A}$  formula has many merits [B17]:

- 1) The boundary condition on the internal interface is natural boundary condition, which is automatically satisfied in the finite element analysis.
- 2) The source current density is readily handled.
- 3) Most of the  $\mathbf{A}$  formulas apply to the multiple-connected conductor problem.

Meanwhile, the  $\mathbf{T}$  formula has several demerits:

- 1) The source current density is included in the governing equations by a newly defined magnetic flux density, which is calculated according to the current density distribution and the Biot-Savart Law.
- 2) To ensure the current continuity at the surface of conductors, the tangential component of the EVP at the conductor surface should be preset to zero.
- 3) It is complicated for the  $\mathbf{T}$  formula to deal with the multiply-connected domains. Surface cuts or volume cuts are required to ensure the monodromy of the computed MSP.

In this thesis, a high precision  $\mathbf{A}$  form, the  $\mathbf{A} - \varphi$  formula, is adopted. From the Gauss's law or equation (2 – 1c), the divergence of the magnetic flux density equals to zero. Since the divergence of curl field equals to zero, a new vector function  $\mathbf{A}$ , namely, the MVP, is defined

$$\mathbf{B} = \nabla \times \mathbf{A} \quad (2 - 7)$$

Substitute this equation into the equation (2 – 5b) and adjust the sequence of the curl and the time derivative, which gives

$$\nabla \times \left( \mathbf{E} + \frac{\partial \mathbf{A}}{\partial t} \right) = 0 \quad (2 - 8)$$

From equation (2 – 8), it is noted that the term  $\left( \mathbf{E} + \frac{\partial \mathbf{A}}{\partial t} \right)$  construct an irrotational field. Since an irrotational field can be formulated as the gradient of a scalar function,

$$\nabla \times (\nabla \varphi) = 0 \quad (2 - 9)$$

Thus, the  $\mathbf{E}$  can be expressed by the MVP  $\mathbf{A}$  and a scalar potential  $\varphi$ , which is named the electric scalar potential (ESP),

$$\mathbf{E} = -\frac{\partial \mathbf{A}}{\partial t} - \nabla \varphi \quad (2 - 10)$$

Then the governing equations (2 – 5a) and (2 – 4a) can be rewritten with the potentials,

$$V_1: \nabla \times (v \nabla \times \mathbf{A}) + \sigma \left( \frac{\partial \mathbf{A}}{\partial t} + \nabla \varphi \right) = 0 \quad (2-11)$$

$$V_2: \nabla \times (v \nabla \times \mathbf{A}) = \mathbf{J} \quad (2-12)$$

And the boundary conditions given in equation (2-6) are rewritten for the potentials,

$$\begin{aligned} S_B: \mathbf{n} \cdot \nabla \times \mathbf{A} &= 0 & (a) \\ S_H: v(\nabla \times \mathbf{A}) \times \mathbf{n} &= \mathbf{0} & (b) \\ S_{12}: \begin{cases} \mathbf{n}_{12} \cdot \nabla \times \mathbf{A}_1 = \mathbf{n}_{12} \cdot \nabla \times \mathbf{A}_2 & (c) \\ v_1 \nabla \times \mathbf{A}_1 \times \mathbf{n}_{12} = v_2 \nabla \times \mathbf{A}_2 \times \mathbf{n}_{12} & (d) \end{cases} & & (2-13) \end{aligned}$$

Owing to the introduced MVP, the equation  $\nabla \cdot \mathbf{B} = 0$  is satisfied automatically. To ensure the uniqueness of the MVP, its divergence and boundary conditions should be predefined. The following homogenous boundary conditions are defined for the MVP [B18]

$$\begin{aligned} S_B: \mathbf{n} \times \mathbf{A} &= \mathbf{0} & (a) \\ S_H: \mathbf{n} \cdot \mathbf{A} &= 0 & (b) \end{aligned} \quad (2-14)$$

Two typical gauges, Coulomb Gauge and Lorentz Gauge, were proposed to define the divergence of the magnetic vector potential. In the relatively more convenient Coulomb Gauge, the divergence of MVP is defined as

$$\nabla \cdot \mathbf{A} = 0 \quad (2-15)$$

In addition, there are some further treatments for the boundary conditions and the governing equations. The equation (2-14a) implies the equation (2-13a), which does not need to be listed again. If the MVP is continuous across the internal interface, the (2-13c) will be satisfied automatically,

$$S_{12}: \mathbf{A}_1 = \mathbf{A}_2 \quad (2-16)$$

The eddy current cannot flow through the interface  $S_{12}$  between conducting region and non-conducting region,

$$S_{12}: \mathbf{n} \cdot \left( -\sigma \frac{\partial \mathbf{A}}{\partial t} - \sigma \nabla \varphi \right) = 0 \quad (2-17)$$

The next step is to integrate the Coulomb Gauge into these governing equations

through adding the item  $-\nabla(v\nabla \cdot \mathbf{A})$  [B3],

$$V_1: \begin{cases} \nabla \times (v\nabla \times \mathbf{A}) - \nabla(v\nabla \cdot \mathbf{A}) + \sigma \left( \frac{\partial \mathbf{A}}{\partial t} + \nabla \varphi \right) = 0 & (a) \\ \nabla \cdot \left( -\sigma \frac{\partial \mathbf{A}}{\partial t} - \sigma \nabla \varphi \right) = 0 & (b) \end{cases} \quad (2-18)$$

$$V_2: \nabla \times (v\nabla \times \mathbf{A}) - \nabla(v\nabla \cdot \mathbf{A}) = \mathbf{J} \quad (2-19)$$

Since the eddy current continuity is no longer implied in the equation (2-18a), the current continuity equation is explicitly listed for the eddy current region  $V_1$ . In order to meet the Coulomb Gauge, the added item should identically equal to zero in the domain, and homogeneous boundary conditions are defined for this term. A homogeneous Dirichlet boundary condition is given on  $S_B$ ,

$$S_B: v\nabla \cdot \mathbf{A} = 0 \quad (2-20)$$

The boundary  $S_H$  is specified with a homogeneous Neumann boundary condition, which is implicitly implied in the equation (2-19)

$$S_H: \frac{\partial}{\partial n} v\nabla \cdot \mathbf{A} = 0 \quad (2-21)$$

In addition, this item should be continuous across the internal interface,

$$S_{12}: v_1 \nabla \cdot \mathbf{A}_1 = v_2 \nabla \cdot \mathbf{A}_2 \quad (2-22)$$

To conclude, all the boundary conditions are listed as below:

$$S_B: \begin{cases} \mathbf{n} \times \mathbf{A} = \mathbf{0} \\ v\nabla \cdot \mathbf{A} = 0 \end{cases} \quad (2-23)$$

$$S_H: \begin{cases} \mathbf{n} \cdot \mathbf{A} = 0 \\ v(\nabla \times \mathbf{A}) \times \mathbf{n} = 0 \end{cases} \quad (2-24)$$

$$S_{12}: \begin{cases} \mathbf{A}_1 = \mathbf{A}_2 \\ v_1 \nabla \cdot \mathbf{A}_1 = v_2 \nabla \cdot \mathbf{A}_2 \\ v_1 \nabla \times \mathbf{A}_1 \times \mathbf{n}_{12} = v_2 \nabla \times \mathbf{A}_2 \times \mathbf{n}_{12} \\ \mathbf{n} \cdot \left( -\sigma \frac{\partial \mathbf{A}}{\partial t} - \sigma \nabla \varphi \right) = 0 \end{cases} \quad (2-26)$$

From the equation (2-10), it is worth noting that once the reference value is given, the unique solution of  $\mathbf{E}$  can be determined after solving the  $\mathbf{A}$ .

### 2.1.3 The Galerkin Finite Element Method

In numerical analysis, the computational domain is discretized into tons of cells, and the initial problem, which attempts to derive an analytical solution for infinite DoFs, is simplified to solving the equations of finite DoFs, which locate on the nodes or the edges of the mesh. The solution of other infinite DoFs are formulated with the calculated solution and the interpolation functions. The weighted residual method is a popular approximation method for solving differential equations. A set of linearly independent weighting functions  $W_i(i = 1, 2, \dots, n)$ , which has the same size as the set of unknowns, is constructed, and the weighted integral of the residual of the equation  $(Lu = f)$  in the computational domain  $\Omega$  is set to zero,

$$\int_{\Omega} W_i(Lu^* - f) = 0 \quad (2 - 27)$$

The unknown function  $u^*$  in the integral is expanded with the chosen basis functions, and an equation set with  $n$  equations and  $n$  unknowns are constructed. If the weighting function and the basis function are consistent, a proprietary name, i.e. the Galerkin method, is used to distinguish this type of weighted residual method from others. The widely adopted Galerkin FEM is a combination of the Galerkin method and the finite element discretization.

In this thesis, the nodal element is adopted in the finite element discretization, thus the MVP and the ESP are all defined on the nodes. For a FEM mesh with  $n$  nodes, the ESP  $\varphi$  is approximately formulated as

$$\varphi \approx \sum_{j=1}^n \varphi_j N_j \quad (2 - 28)$$

where;  $\varphi_j$  is the ESP at node  $j$ , and  $N_j$  is the global basis function of node  $j$  [B19].

Apply the Galerkin FEM to the eddy current continuity function (2 – 18b) with

the scalar weighting function  $W$ , and the weighted integral of the residual reads

$$\int_{V_1} W \nabla \cdot \left( -\sigma \frac{\partial \mathbf{A}}{\partial t} - \sigma \nabla \varphi \right) dV = 0 \quad (2-29)$$

With the vector identity  $\nabla \cdot (f\mathbf{A}) = f(\nabla \cdot \mathbf{A}) + \mathbf{A} \cdot (\nabla f)$ , the equation (2-29) can be rewritten as

$$\int_{V_1} \nabla \cdot \left[ W \left( -\sigma \frac{\partial \mathbf{A}}{\partial t} - \sigma \nabla \varphi \right) \right] dV + \int_{V_1} \nabla W \cdot \left( \sigma \frac{\partial \mathbf{A}}{\partial t} + \sigma \nabla \varphi \right) dV = 0 \quad (2-30)$$

Transform the first term to surface integral with the Gauss theorem,

$$\int_{S_{12}} W \left( -\sigma \frac{\partial \mathbf{A}}{\partial t} - \sigma \nabla \varphi \right) \cdot \mathbf{n}_{12} dS + \int_{V_1} \nabla W \cdot \left( \sigma \frac{\partial \mathbf{A}}{\partial t} + \sigma \nabla \varphi \right) dV = 0 \quad (2-31)$$

According to the boundary condition (2-17) on the internal interface, the surface integral equals to zero, and the weighted residual finally reads

$$\int_{V_1} \nabla W \cdot \left( \sigma \frac{\partial \mathbf{A}}{\partial t} + \sigma \nabla \varphi \right) dV = 0 \quad (2-32)$$

Compared to the straightforward expansion of the ESP, the interpolation of the MVP and the following transformation of the governing equations, equation (2-18a) and (2-19), are a bit complicated. Actually, three scalar equations for the three directions ( $x$ ,  $y$  and  $z$ ) are included in these two equations. Each scalar weighting function forms three vector weighting functions,  $N_j \mathbf{i}$ ,  $N_j \mathbf{j}$  and  $N_j \mathbf{k}$ , to isolate the scalar equation for each direction. Like the ESP, the MVP can be expanded by the basis function as

$$\mathbf{A} = [A_x \quad A_y \quad A_z] \approx \sum_{j=1}^n \mathbf{A}_j N_j = \left[ \sum_{j=1}^n A_{xj} N_j \quad \sum_{j=1}^n A_{yj} N_j \quad \sum_{j=1}^n A_{zj} N_j \right] \quad (2-33)$$

For those known potential components at the boundary, the corresponding weighting function should be set to zero to ensure that the number of equations is equal to the number of DoFs. According to the boundary conditions (2-14), the following

equations are defined for the weighting functions,

$$\begin{aligned} S_B: \mathbf{n} \times \mathbf{W} &= \mathbf{0} & (a) \\ S_H: \mathbf{n} \cdot \mathbf{W} &= 0 & (b) \end{aligned} \quad (2-34)$$

Dislike the current continuity equation (2-18b), there is a second derivative in the governing equation (2-18a) and (2-19), which are summarized into a general form

$$\nabla \times (v\nabla \times \mathbf{A}) - \nabla(v\nabla \cdot \mathbf{A}) + \sigma \left( \frac{\partial \mathbf{A}}{\partial t} + \nabla\varphi \right) - \mathbf{J} = 0 \quad (2-35)$$

In the following steps, the weighted integral of the residual of this equation is transformed into the Galerkin Weak Formulation (GWF) [B20], which only has first derivative. The weighted integral of the residual of equation (2-35) reads,

$$\int_V \mathbf{W} \cdot \left[ \nabla \times (v\nabla \times \mathbf{A}) - \nabla(v\nabla \cdot \mathbf{A}) + \sigma \left( \frac{\partial \mathbf{A}}{\partial t} + \nabla\varphi \right) - \mathbf{J} \right] dV = 0 \quad (2-36)$$

With the vector identity  $\nabla \cdot (\mathbf{A} \times \mathbf{B}) = \mathbf{B} \cdot (\nabla \times \mathbf{A}) - \mathbf{A} \cdot (\nabla \times \mathbf{B})$ , the first item in the integral are transformed to

$$\begin{aligned} \int_V \mathbf{W} \cdot \nabla \times (v\nabla \times \mathbf{A}) dV &= \int_V (v\nabla \times \mathbf{A} \cdot \nabla \times \mathbf{W}) dV \\ &- \int_V \nabla \cdot [\mathbf{W} \times (v\nabla \times \mathbf{A})] dV \end{aligned} \quad (2-37)$$

Then the second term on the right-hand-side is transformed to the surface integral by using Gauss theorem,

$$\begin{aligned} \int_V \mathbf{W} \cdot \nabla \times (v\nabla \times \mathbf{A}) dV &= \int_V (v\nabla \times \mathbf{A} \cdot \nabla \times \mathbf{W}) dV \\ &- \left[ \int_{S_H} [\mathbf{W} \times (v\nabla \times \mathbf{A})] \cdot \mathbf{n} dS + \int_{S_{12}} [\mathbf{W} \times (v_1\nabla \times \mathbf{A}_1)] \cdot \mathbf{n}_{12} dS \right. \\ &\left. + \int_{S_B} [\mathbf{W} \times (v\nabla \times \mathbf{A})] \cdot \mathbf{n} dS - \int_{S_{12}} [\mathbf{W} \times (v_2\nabla \times \mathbf{A}_2)] \cdot \mathbf{n}_{12} dS \right] \end{aligned} \quad (2-38)$$

With the vector identity  $\nabla \cdot (f\mathbf{A}) = f(\nabla \cdot \mathbf{A}) + \mathbf{A} \cdot (\nabla f)$  and the Gauss theorem, the second term of the equation (2-36) is transformed to

$$\begin{aligned}
\int_V \mathbf{W} \cdot \nabla(v \nabla \cdot \mathbf{A}) dV &= \int_V \nabla \cdot [(v \nabla \cdot \mathbf{A}) \mathbf{W}] dV - \int_V (v \nabla \cdot \mathbf{A}) \nabla \cdot \mathbf{W} dV \\
&= \int_{S_H} (v \nabla \cdot \mathbf{A}) \mathbf{W} \cdot \mathbf{n} dS + \int_{S_{12}} (v_1 \nabla \cdot \mathbf{A}_1) \mathbf{W} \cdot \mathbf{n}_{12} dS \\
+ \int_{S_B} (v \nabla \cdot \mathbf{A}) \mathbf{W} \cdot \mathbf{n} dS &- \int_{S_{12}} (v_2 \nabla \cdot \mathbf{A}_2) \mathbf{W} \cdot \mathbf{n}_{12} dS - \int_V (v \nabla \cdot \mathbf{A}) \nabla \cdot \mathbf{W} dV \quad (2-39)
\end{aligned}$$

Substitute the equations (2-38) and (2-39) into the equation (2-36),

$$\begin{aligned}
\int_V \left[ (v \nabla \times \mathbf{A} \cdot \nabla \times \mathbf{W}) + (v \nabla \cdot \mathbf{A}) \nabla \cdot \mathbf{W} + \sigma \mathbf{W} \cdot \left( \frac{\partial \mathbf{A}}{\partial t} + \nabla \varphi \right) - \mathbf{W} \cdot \mathbf{J} \right] dV \\
- \int_{S_{12}} [\mathbf{W} \times (v_1 \nabla \times \mathbf{A}_1)] \cdot \mathbf{n}_{12} dS + \int_{S_{12}} [\mathbf{W} \times (v_2 \nabla \times \mathbf{A}_2)] \cdot \mathbf{n}_{12} dS \\
- \int_{S_{12}} (v_1 \nabla \cdot \mathbf{A}_1) \mathbf{W} \cdot \mathbf{n}_{12} dS + \int_{S_{12}} (v_2 \nabla \cdot \mathbf{A}_2) \mathbf{W} \cdot \mathbf{n}_{12} dS \\
- \int_{S_H} [\mathbf{W} \times (v \nabla \times \mathbf{A})] \cdot \mathbf{n} dS - \int_{S_B} [\mathbf{W} \times (v \nabla \times \mathbf{A})] \cdot \mathbf{n} dS \\
- \int_{S_H} (v \nabla \cdot \mathbf{A}) \mathbf{W} \cdot \mathbf{n} dS - \int_{S_B} (v \nabla \cdot \mathbf{A}) \mathbf{W} \cdot \mathbf{n} dS \quad (2-40)
\end{aligned}$$

With the scalar triple product  $\mathbf{F} \cdot (\mathbf{B} \times \mathbf{C}) = \mathbf{B} \cdot (\mathbf{C} \times \mathbf{F}) = \mathbf{C} \cdot (\mathbf{F} \times \mathbf{B})$  and the boundary condition (2-13d) on the internal interface  $S_{12}$ , the first term and the second term offset. From the boundary condition (2-22) on  $S_{12}$ , it is noted that the sum of the third term and the fourth term equals to zero. According to the boundary condition (2-13b) on the  $S_H$  and the boundary condition (2-20) on  $S_B$ , the fifth term and the eighth term are zero. The sixth term and the seventh term are also equal to zero based on the boundary conditions of the basis function (2-34). Thus, the equation (2-40) can be rewritten as

$$\int_V \left[ (v \nabla \times \mathbf{A} \cdot \nabla \times \mathbf{W}) + (v \nabla \cdot \mathbf{A}) \nabla \cdot \mathbf{W} + \sigma \mathbf{W} \cdot \left( \frac{\partial \mathbf{A}}{\partial t} + \nabla \varphi \right) - \mathbf{W} \cdot \mathbf{J} \right] dV = 0 \quad (2-41)$$

It is noted that the time derivative of MVP is involved in the integral equations (2-41) and (2-32). Unlike the space derivative, the time derivative is generally discretized by the FDM, which includes several forms with different characteristics

[B21]. The forward difference method, also known as the explicit method, construct a simple but unstable equation set. The system formed by the backward difference method is unconditionally stable. These two difference methods are first order accurate. The central difference method is second order accurate, while the resulted algebraic system is conditionally stable. In this thesis, the time derivative is approximated with the backward difference method,

$$\frac{\partial \mathbf{A}}{\partial t} = \frac{\mathbf{A}^{(k+1)} - \mathbf{A}^{(k)}}{\Delta t} \quad (2 - 42)$$

These two governing equations (2 - 41) and (2 - 32) are rewritten after expanding the time derivative,

$$\int_V [(v \nabla \times \mathbf{A}^{(k+1)} \cdot \nabla \times \mathbf{W}) + (v \nabla \cdot \mathbf{A}^{(k+1)}) \nabla \cdot \mathbf{W} + \sigma \mathbf{W} \cdot \left( \frac{\mathbf{A}^{(k+1)}}{\Delta t} + \nabla \varphi^{(k+1)} \right)] dV = \int_V \mathbf{W} \cdot \mathbf{J} + \sigma \mathbf{W} \cdot \left( \frac{\mathbf{A}^{(k)}}{\Delta t} \right) dV \quad (2 - 43)$$

$$\int_{V_1} \nabla W \cdot \left( \sigma \frac{\mathbf{A}^{(k+1)}}{\Delta t} + \sigma \nabla \varphi^{(k+1)} \right) dV = \int_{V_1} \nabla W \cdot \left( \sigma \frac{\mathbf{A}^{(k)}}{\Delta t} \right) dV \quad (2 - 44)$$

As introduced before, three scalar equations are included in the equation (2 - 43), and three sets of vector shape functions along the  $x$ ,  $y$  and  $z$  axes are referred as the weighting functions to isolate these scalar equations in different directions. It is noted that the curl, divergence, and gradient of these parameters are involved in the integral equations. To facilitate the calculation, the following identities are given for the operators,

$$\left\{ \begin{array}{l}
\nabla \times \mathbf{A} = \left( \frac{\partial A_z}{\partial y} - \frac{\partial A_y}{\partial z} \right) \mathbf{i} + \left( \frac{\partial A_x}{\partial z} - \frac{\partial A_z}{\partial x} \right) \mathbf{j} + \left( \frac{\partial A_y}{\partial x} - \frac{\partial A_x}{\partial y} \right) \mathbf{k} \\
\nabla \cdot \mathbf{A} = \frac{\partial A_x}{\partial x} + \frac{\partial A_y}{\partial y} + \frac{\partial A_z}{\partial z} \\
\nabla \varphi = \frac{\partial \varphi}{\partial x} \mathbf{i} + \frac{\partial \varphi}{\partial y} \mathbf{j} + \frac{\partial \varphi}{\partial z} \mathbf{k} \\
\nabla W = \frac{\partial N_i}{\partial x} \mathbf{i} + \frac{\partial N_i}{\partial y} \mathbf{j} + \frac{\partial N_i}{\partial z} \mathbf{k} \\
\nabla \times \mathbf{W} = \frac{\partial N_i}{\partial z} \mathbf{j} - \frac{\partial N_i}{\partial y} \mathbf{k}, \quad \mathbf{W} = [N_i \ 0 \ 0] \\
\nabla \cdot \mathbf{W} = \frac{\partial N_i}{\partial x}, \quad \mathbf{W} = [N_i \ 0 \ 0] \\
\nabla \times \mathbf{W} = -\frac{\partial N_i}{\partial z} \mathbf{i} + \frac{\partial N_i}{\partial x} \mathbf{k}, \quad \mathbf{W} = [0 \ N_i \ 0] \\
\nabla \cdot \mathbf{W} = \frac{\partial N_i}{\partial y}, \quad \mathbf{W} = [0 \ N_i \ 0] \\
\nabla \times \mathbf{W} = \frac{\partial N_i}{\partial y} \mathbf{i} - \frac{\partial N_i}{\partial x} \mathbf{j}, \quad \mathbf{W} = [0 \ 0 \ N_i] \\
\nabla \cdot \mathbf{W} = \frac{\partial N_i}{\partial z}, \quad \mathbf{W} = [0 \ 0 \ N_i]
\end{array} \right. \quad (2-45)$$

Applying the first set of vector weighting functions  $\mathbf{W} = [N_i \ 0 \ 0]$  and expanding the potentials with the basis functions, the equation (2-43) is transformed to

$$\begin{aligned}
& \int_V v \frac{\partial N_i}{\partial z} \left( \sum_{j=1}^n A_{xj}^{(k+1)} \frac{\partial N_j}{\partial z} - \sum_{j=1}^n A_{zj}^{(k+1)} \frac{\partial N_j}{\partial x} \right) dV \\
& - \int_V v \frac{\partial N_i}{\partial y} \left( \sum_{j=1}^n A_{yj}^{(k+1)} \frac{\partial N_j}{\partial x} - \sum_{j=1}^n A_{xj}^{(k+1)} \frac{\partial N_j}{\partial y} \right) dV \\
& + \int_V v \frac{\partial N_i}{\partial x} \left( \sum_{j=1}^n A_{xj}^{(k+1)} \frac{\partial N_j}{\partial x} + \sum_{j=1}^n A_{yj}^{(k+1)} \frac{\partial N_j}{\partial y} + \sum_{j=1}^n A_{zj}^{(k+1)} \frac{\partial N_j}{\partial z} \right) dV \\
& + \int_V \frac{\sigma}{\Delta t} \sum_{j=1}^n A_{xj}^{(k+1)} N_i N_j dV + \int_V \sigma \sum_{j=1}^n \varphi_j^{(k+1)} N_i \frac{\partial N_j}{\partial x} dV \\
& = \int_V N_i J_x dV + \int_V \frac{\sigma}{\Delta t} \sum_{j=1}^n A_{xj}^{(k)} N_i N_j dV \quad (2-46)
\end{aligned}$$

Adjust the order of the terms in this equation and congregate the coefficients for

different variables,

$$\begin{aligned}
& \sum_{j=1}^n A_{xj}^{(k+1)} \int_V \left[ v \left( \frac{\partial N_i}{\partial y} \frac{\partial N_j}{\partial y} + \frac{\partial N_i}{\partial z} \frac{\partial N_j}{\partial z} + \frac{\partial N_i}{\partial x} \frac{\partial N_j}{\partial x} \right) + \frac{\sigma}{\Delta t} N_i N_j \right] dV \\
& + \sum_{j=1}^n A_{yj}^{(k+1)} \int_V \left[ v \left( -\frac{\partial N_i}{\partial y} \frac{\partial N_j}{\partial x} + \frac{\partial N_i}{\partial x} \frac{\partial N_j}{\partial y} \right) \right] dV \\
& + \sum_{j=1}^n A_{zj}^{(k+1)} \int_V \left[ v \left( -\frac{\partial N_i}{\partial z} \frac{\partial N_j}{\partial x} + \frac{\partial N_i}{\partial x} \frac{\partial N_j}{\partial z} \right) \right] dV \\
& + \sum_{j=1}^n \varphi_j^{(k+1)} \sigma \int_V N_i \frac{\partial N_j}{\partial x} dV \\
& = \int_V N_i J_x dV \\
& + \sum_{j=1}^n A_{xj}^{(k)} \frac{\sigma}{\Delta t} \int_V N_i N_j dV
\end{aligned} \tag{2-47}$$

Rewrite the equation in a simplified form,

$$\begin{aligned}
& \sum_{j=1}^n \left[ C_{xx} A_{xj}^{(k+1)} + C_{xy} A_{yj}^{(k+1)} + C_{xz} A_{zj}^{(k+1)} + C_{x\varphi} \varphi_j^{(k+1)} \right] \\
& = F_{xi} + \sum_{j=1}^n D_{xx} A_{xj}^{(k)}
\end{aligned} \tag{2-48}$$

where;

$$\left\{ \begin{aligned}
C_{xx} &= \int_V \left[ v \left( \frac{\partial N_i}{\partial y} \frac{\partial N_j}{\partial y} + \frac{\partial N_i}{\partial z} \frac{\partial N_j}{\partial z} + \frac{\partial N_i}{\partial x} \frac{\partial N_j}{\partial x} \right) + \frac{\sigma}{\Delta t} N_i N_j \right] dV \\
C_{xy} &= \int_V \left[ v \left( -\frac{\partial N_i}{\partial y} \frac{\partial N_j}{\partial x} + \frac{\partial N_i}{\partial x} \frac{\partial N_j}{\partial y} \right) \right] dV \\
C_{xz} &= \int_V \left[ v \left( -\frac{\partial N_i}{\partial z} \frac{\partial N_j}{\partial x} + \frac{\partial N_i}{\partial x} \frac{\partial N_j}{\partial z} \right) \right] dV \\
C_{x\varphi} &= \sigma \int_V N_i \frac{\partial N_j}{\partial x} dV
\end{aligned} \right. \tag{2-49}$$

$$F_{xi} = \int_V N_i J_x dV \tag{2-50}$$

$$D_{xx} = \frac{\sigma}{\Delta t} \int_V N_i N_j dV \quad (2-51)$$

Other two scalar equations are extracted from the equation (2-43) in a similar way. With the second set of vector weighting functions  $\mathbf{W} = [0 \ N_i \ 0]$ , other  $n$  equations are obtained,

$$\begin{aligned} \sum_{j=1}^n [C_{yx} A_{xj}^{(k+1)} + C_{yy} A_{yj}^{(k+1)} + C_{yz} A_{zj}^{(k+1)} + C_{y\varphi} \varphi_j^{(k+1)}] \\ = F_{yi} + \sum_{j=1}^n D_{yy} A_{yj}^{(k)} \end{aligned} \quad (2-52)$$

where;

$$\left\{ \begin{array}{l} C_{yx} = \int_V \left[ v \left( -\frac{\partial N_i}{\partial x} \frac{\partial N_j}{\partial y} + \frac{\partial N_i}{\partial y} \frac{\partial N_j}{\partial x} \right) \right] dV \\ C_{yy} = \int_V \left[ v \left( \frac{\partial N_i}{\partial y} \frac{\partial N_j}{\partial y} + \frac{\partial N_i}{\partial z} \frac{\partial N_j}{\partial z} + \frac{\partial N_i}{\partial x} \frac{\partial N_j}{\partial x} \right) + \frac{\sigma}{\Delta t} N_i N_j \right] dV \\ C_{yz} = \int_V \left[ v \left( -\frac{\partial N_i}{\partial z} \frac{\partial N_j}{\partial y} + \frac{\partial N_i}{\partial y} \frac{\partial N_j}{\partial z} \right) \right] dV \\ C_{y\varphi} = \sigma \int_V N_i \frac{\partial N_j}{\partial y} dV \end{array} \right. \quad (2-53)$$

$$F_{yi} = \int_V N_i J_y dV \quad (2-54)$$

$$D_{yy} = \frac{\sigma}{\Delta t} \int_V N_i N_j dV \quad (2-55)$$

With the last set of vector weighting functions  $\mathbf{W} = [0 \ 0 \ N_i]$ , the equation (2-43) is transformed to

$$\begin{aligned} \sum_{j=1}^n [C_{zx} A_{xj}^{(k+1)} + C_{zy} A_{yj}^{(k+1)} + C_{zz} A_{zj}^{(k+1)} + C_{z\varphi} \varphi_j^{(k+1)}] \\ = F_{zi} + \sum_{j=1}^n D_{zz} A_{zj}^{(k)} \end{aligned} \quad (2-56)$$

where;

$$\left\{ \begin{array}{l} C_{zx} = \int_V \left[ v \left( -\frac{\partial N_i}{\partial x} \frac{\partial N_j}{\partial z} + \frac{\partial N_i}{\partial z} \frac{\partial N_j}{\partial x} \right) \right] dV \\ C_{zy} = \int_V \left[ v \left( -\frac{\partial N_i}{\partial y} \frac{\partial N_j}{\partial z} + \frac{\partial N_i}{\partial z} \frac{\partial N_j}{\partial y} \right) \right] dV \\ C_{zz} = \int_V \left[ v \left( \frac{\partial N_i}{\partial y} \frac{\partial N_j}{\partial y} + \frac{\partial N_i}{\partial z} \frac{\partial N_j}{\partial z} + \frac{\partial N_i}{\partial x} \frac{\partial N_j}{\partial x} \right) + \frac{\sigma}{\Delta t} N_i N_j \right] dV \\ C_{z\varphi} = \sigma \int_V N_i \frac{\partial N_j}{\partial z} dV \end{array} \right. \quad (2-57)$$

$$F_{zi} = \int_V N_i J_z dV \quad (2-58)$$

$$D_{zz} = \frac{\sigma}{\Delta t} \int_V N_i N_j dV \quad (2-59)$$

Substitute the weighting function  $N_i$  and the operators of these parameters into the equation (2-44),

$$\begin{aligned} & \int_{V_1} \frac{\sigma}{\Delta t} \left( \frac{\partial N_i}{\partial x} \mathbf{i} + \frac{\partial N_i}{\partial y} \mathbf{j} + \frac{\partial N_i}{\partial z} \mathbf{k} \right) \cdot \sum_{j=1}^n \left( A_{xj}^{(k+1)} N_j \mathbf{i} + A_{yj}^{(k+1)} N_j \mathbf{j} + A_{zj}^{(k+1)} N_j \mathbf{k} \right) dV + \\ & \int_{V_1} \sigma \left( \frac{\partial N_i}{\partial x} \mathbf{i} + \frac{\partial N_i}{\partial y} \mathbf{j} + \frac{\partial N_i}{\partial z} \mathbf{k} \right) \cdot \sum_{j=1}^n \left( \frac{\partial N_j}{\partial x} \varphi_j^{(k+1)} \mathbf{i} + \frac{\partial N_j}{\partial y} \varphi_j^{(k+1)} \mathbf{j} + \frac{\partial N_j}{\partial z} \varphi_j^{(k+1)} \mathbf{k} \right) dV \\ & = \int_{V_1} \frac{\sigma}{\Delta t} \left( \frac{\partial N_i}{\partial x} \mathbf{i} + \frac{\partial N_i}{\partial y} \mathbf{j} + \frac{\partial N_i}{\partial z} \mathbf{k} \right) \cdot \sum_{j=1}^n \left( A_{xj}^{(k)} N_j \mathbf{i} + A_{yj}^{(k)} N_j \mathbf{j} + A_{zj}^{(k)} N_j \mathbf{k} \right) dV \end{aligned} \quad (2-60)$$

Rewrite the equation by congregating the coefficients for different variables,

$$\begin{aligned}
& \sum_{j=1}^n A_{xj}^{(k+1)} \int_{V_1} \left[ \frac{\sigma}{\Delta t} N_j \frac{\partial N_i}{\partial x} \right] dV \\
& + \sum_{j=1}^n A_{yj}^{(k+1)} \int_{V_1} \left[ \frac{\sigma}{\Delta t} N_j \frac{\partial N_i}{\partial y} \right] dV \\
& + \sum_{j=1}^n A_{zj}^{(k+1)} \int_{V_1} \left[ \frac{\sigma}{\Delta t} N_j \frac{\partial N_i}{\partial z} \right] dV \\
& + \sum_{j=1}^n \varphi_j^{(k+1)} \sigma \int_V \left[ \frac{\partial N_i}{\partial x} \frac{\partial N_j}{\partial x} + \frac{\partial N_i}{\partial y} \frac{\partial N_j}{\partial y} + \frac{\partial N_i}{\partial z} \frac{\partial N_j}{\partial z} \right] dV \\
& = \sum_{j=1}^n A_{xj}^{(k)} \int_{V_1} \left[ \frac{\sigma}{\Delta t} N_j \frac{\partial N_i}{\partial x} \right] dV \\
& + \sum_{j=1}^n A_{yj}^{(k)} \int_{V_1} \left[ \frac{\sigma}{\Delta t} N_j \frac{\partial N_i}{\partial y} \right] dV + \sum_{j=1}^n A_{zj}^{(k)} \int_{V_1} \left[ \frac{\sigma}{\Delta t} N_j \frac{\partial N_i}{\partial z} \right] dV
\end{aligned} \tag{2-61}$$

Then simplify the equation as

$$\begin{aligned}
& \sum_{j=1}^n \left[ C_{\varphi x} A_{xj}^{(k+1)} + C_{\varphi y} A_{yj}^{(k+1)} + C_{\varphi z} A_{zj}^{(k+1)} + C_{\varphi\varphi} \varphi_j^{(k+1)} \right] \\
& = \sum_{j=1}^n \left[ D_{\varphi x} A_{xj}^{(k)} + D_{\varphi y} A_{yj}^{(k)} + D_{\varphi z} A_{zj}^{(k)} \right]
\end{aligned} \tag{2-62}$$

Where;

$$\left\{ \begin{aligned}
C_{\varphi x} &= \int_{V_1} \left[ \frac{\sigma}{\Delta t} N_j \frac{\partial N_i}{\partial x} \right] dV \\
C_{\varphi y} &= \int_{V_1} \left[ \frac{\sigma}{\Delta t} N_j \frac{\partial N_i}{\partial y} \right] dV \\
C_{\varphi z} &= \int_{V_1} \left[ \frac{\sigma}{\Delta t} N_j \frac{\partial N_i}{\partial z} \right] dV \\
C_{\varphi\varphi} &= \sigma \int_V \left[ \frac{\partial N_i}{\partial x} \frac{\partial N_j}{\partial x} + \frac{\partial N_i}{\partial y} \frac{\partial N_j}{\partial y} + \frac{\partial N_i}{\partial z} \frac{\partial N_j}{\partial z} \right] dV
\end{aligned} \right. \tag{2-63}$$

$$\begin{cases} D_{\varphi x} = \int_{V_1} \left[ \frac{\sigma}{\Delta t} N_j \frac{\partial N_i}{\partial x} \right] dV \\ D_{\varphi y} = \int_{V_1} \left[ \frac{\sigma}{\Delta t} N_j \frac{\partial N_i}{\partial y} \right] dV \\ D_{\varphi z} = \int_{V_1} \left[ \frac{\sigma}{\Delta t} N_j \frac{\partial N_i}{\partial z} \right] dV \end{cases} \quad (2 - 64)$$

To conclude, for a mesh file with  $n$  nodes, there are total  $4n$  equations are generated from the equations (2 – 43) and (2 – 44). The number of equations is equal to the number of DoFs, which are included in the computational domain. To facilitate the following programming, these  $4n$  equations are rewritten in the matrix form

$$[S]\{u^{(k+1)}\} = [F] + [D]\{u^{(k)}\} \quad (2 - 65)$$

where;  $\{u\}$  is a column vector of the unknowns,  $\mathbf{A}$  and  $\varphi$ ;  $[S]$  is the stiffness matrix assembled according to the unknown vector;  $[F]$  is the load vector calculated with the source current density  $\mathbf{J}$ ;  $[D]$  is the matrix related to the former step solution;  $k + 1$  and  $k$  represent the current step and the former step, respectively. The unknown vector  $\{u\}$  is arranged as follows with the sub-vector  $u_i = [A_{xi} \ A_{yi} \ A_{zi} \ \varphi_i]$ ,

$$u = [u_1 \ u_2 \ \dots \ u_n]^T \quad (2 - 66)$$

Similarly, the sub-vector  $F_i$  and the load vector  $[F]$  is expressed as

$$\begin{cases} F_i = [F_{xi} \ F_{yi} \ F_{zi} \ 0] & (a) \\ F = [F_1 \ F_2 \ \dots \ F_n]^T & (b) \end{cases} \quad (2 - 67)$$

The size of these two vectors is  $4n \times 1$ , and the other two matrixes are  $4n \times 4n$  in size. The stiffness matrix  $[S]$  is formed by  $n \times n$  sub-matrixes,

$$[S] = \begin{bmatrix} S_{11} & S_{12} & \dots & S_{1n} \\ S_{21} & S_{22} & \dots & S_{2n} \\ \vdots & \vdots & \ddots & \vdots \\ S_{n1} & S_{n2} & \dots & S_{nn} \end{bmatrix} \quad (2 - 68)$$

where the entry  $S_{ij}$  is assembled as follows,

$$[S_{ij}] = \begin{bmatrix} C_{xx} & C_{xy} & C_{xz} & C_{x\varphi} \\ C_{yx} & C_{yy} & C_{yz} & C_{y\varphi} \\ C_{zx} & C_{zy} & C_{zz} & C_{z\varphi} \\ C_{\varphi x} & C_{\varphi y} & C_{\varphi z} & C_{\varphi\varphi} \end{bmatrix} \quad (i, j = 1, 2, \dots, n) \quad (2-69)$$

The matrix  $[D]$  is arranged in a similar way with the entries of sub-matrix assembled as

$$[D_{ij}] = \begin{bmatrix} D_{xx} & 0 & 0 & 0 \\ 0 & D_{yy} & 0 & 0 \\ 0 & 0 & D_{zz} & 0 \\ D_{\varphi x} & D_{\varphi y} & D_{\varphi z} & 0 \end{bmatrix} \quad (i, j = 1, 2, \dots, n) \quad (2-70)$$

## 2.1.4 Calculation of the Element Matrices

Tetrahedron, which can handle complicated geometries, is the most widely used element to discretize 3-D problems. In the linear tetrahedron element, only the four vertexes are defined as the nodes of finite element. Since the basis function can be directly formulated with the original coordinates, coordinate transformation is not indispensable for this type of element. According to the right-hand-screw rule, the four nodes are indexed as  $K$ ,  $M$ ,  $N$ , and  $L$ , successively, as shown in Fig. 2.2. For one tetrahedron element  $e$ , the element basis function is given by

$$N_i^e = \frac{1}{6V_e} (p_i + q_i x + r_i y + s_i z), \quad (i = K, M, N, L) \quad (2-71)$$

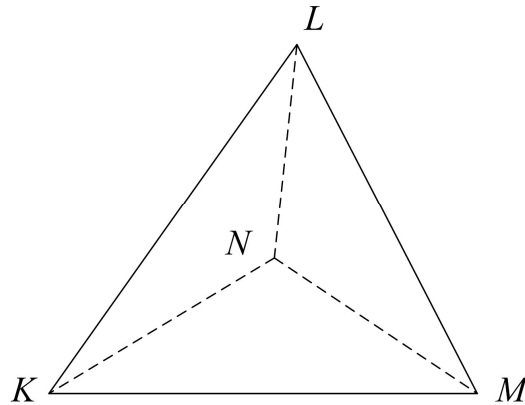


Fig. 2.2. The tetrahedron element.

where;  $V_e$  is the volume of the tetrahedral element  $e$ ;  $p_i$   $q_i$   $r_i$  and  $s_i$  are the coefficients for node  $i$ . All the parameters that are involved in the shape functions are calculated as follows:

$$\begin{aligned}
 V_e &= \frac{1}{6} \begin{bmatrix} 1 & x_K & y_K & z_K \\ 1 & x_M & y_M & z_M \\ 1 & x_N & y_N & z_N \\ 1 & x_L & y_L & z_L \end{bmatrix} \\
 p_K &= \begin{bmatrix} x_M & y_M & z_M \\ x_N & y_N & z_N \\ x_L & y_L & z_L \end{bmatrix} & p_M &= - \begin{bmatrix} x_K & y_K & z_K \\ x_N & y_N & z_N \\ x_L & y_L & z_L \end{bmatrix} \\
 p_N &= \begin{bmatrix} x_K & y_K & z_K \\ x_M & y_M & z_M \\ x_L & y_L & z_L \end{bmatrix} & p_L &= - \begin{bmatrix} x_K & y_K & z_K \\ x_M & y_M & z_M \\ x_N & y_N & z_N \end{bmatrix} \\
 q_K &= - \begin{bmatrix} 1 & y_M & z_M \\ 1 & y_N & z_N \\ 1 & y_L & z_L \end{bmatrix} & q_M &= \begin{bmatrix} 1 & y_K & z_K \\ 1 & y_N & z_N \\ 1 & y_L & z_L \end{bmatrix} \\
 q_N &= \begin{bmatrix} 1 & y_K & z_K \\ 1 & y_M & z_M \\ 1 & y_L & z_L \end{bmatrix} & q_L &= - \begin{bmatrix} 1 & y_K & z_K \\ 1 & y_M & z_M \\ 1 & y_N & z_N \end{bmatrix} & (2 - 72) \\
 r_K &= \begin{bmatrix} x_M & 1 & z_M \\ x_N & 1 & z_N \\ x_L & 1 & z_L \end{bmatrix} & r_M &= - \begin{bmatrix} x_K & 1 & z_K \\ x_N & 1 & z_N \\ x_L & 1 & z_L \end{bmatrix} \\
 r_N &= \begin{bmatrix} x_K & 1 & z_K \\ x_M & 1 & z_M \\ x_L & 1 & z_L \end{bmatrix} & r_L &= - \begin{bmatrix} x_K & 1 & z_K \\ x_M & 1 & z_M \\ x_N & 1 & z_N \end{bmatrix} \\
 s_K &= \begin{bmatrix} x_M & y_M & 1 \\ x_N & y_N & 1 \\ x_L & y_L & 1 \end{bmatrix} & s_M &= - \begin{bmatrix} x_K & y_K & 1 \\ x_N & y_N & 1 \\ x_L & y_L & 1 \end{bmatrix} \\
 s_N &= \begin{bmatrix} x_K & y_K & 1 \\ x_M & y_M & 1 \\ x_L & y_L & 1 \end{bmatrix} & s_L &= - \begin{bmatrix} x_K & y_K & 1 \\ x_M & y_M & 1 \\ x_N & y_N & 1 \end{bmatrix}
 \end{aligned}$$

From the fully expanded equations, it is found that the coefficients of these unknowns are formulated by the integral of shape function and its derivative. For the linear tetrahedron element, an identity for the volume integral of shape functions is obtained by applying the integration by substitution,

$$\int_{V_e} N_1^{m_1} N_2^{m_2} N_3^{m_3} N_4^{m_4} dV = \frac{m_1! m_2! m_3! m_4!}{(m_1 + m_2 + m_3 + m_4 + 3)!} 6V_e \quad (2-73)$$

According to this identity, the values of two common integrals are given,

$$\begin{cases} \int_{V_e} N_i dV = \frac{1}{4} V_e \\ \int_{V_e} N_i N_j dV = \frac{m}{20} V_e \quad m = \begin{cases} 2 & (i = j) \\ 1 & (i \neq j) \end{cases} \end{cases} \quad (2-74)$$

Hence, the contribution of this element  $e$  to the sub-matrix  $[S_{ij}]$ ,  $[D_{ij}]$ , and  $[F_i]$  can be calculated as follows,

$$[S_{ij}^e] = \begin{bmatrix} C_{xx}^e & C_{xy}^e & C_{xz}^e & C_{x\phi}^e \\ C_{yx}^e & C_{yy}^e & C_{yz}^e & C_{y\phi}^e \\ C_{zx}^e & C_{zy}^e & C_{zz}^e & C_{z\phi}^e \\ C_{\phi x}^e & C_{\phi y}^e & C_{\phi z}^e & C_{\phi\phi}^e \end{bmatrix} \quad (i, j = K, M, N, L) \quad (2-75)$$

$$[D_{ij}^e] = \begin{bmatrix} D_{xx}^e & 0 & 0 & 0 \\ 0 & D_{yy}^e & 0 & 0 \\ 0 & 0 & D_{zz}^e & 0 \\ D_{\phi x}^e & D_{\phi y}^e & D_{\phi z}^e & 0 \end{bmatrix} \quad (i, j = K, M, N, L) \quad (2-76)$$

$$[F_i^e] = [F_{xi}^e \quad F_{yi}^e \quad F_{zi}^e \quad 0] \quad (i = K, M, N, L) \quad (2-77)$$

where

$$\begin{cases} C_{xx}^e = \frac{v}{36V_e} (r_i r_j + s_i s_j + q_i q_j) + \frac{\sigma}{\Delta t} \frac{m}{20} V_e \\ C_{xy}^e = \frac{v}{36V_e} (-r_i q_j + q_i r_j) \\ C_{xz}^e = \frac{v}{36V_e} (-s_i q_j + q_i s_j) \\ C_{x\phi}^e = \frac{\sigma}{24} q_j \end{cases} \quad (2-78)$$

$$\left\{ \begin{array}{l} C_{yx}^e = \frac{v}{36V_e}(-q_i r_j + r_i q_j) \\ C_{yy}^e = \frac{v}{36V_e}(q_i q_j + s_i s_j + r_i r_j) + \frac{\sigma}{\Delta t} \frac{m}{20} V_e \\ C_{yz}^e = \frac{v}{36V_e}(-s_i r_j + r_i s_j) \\ C_{y\varphi}^e = \frac{\sigma}{24} r_j \end{array} \right. \quad (2-79)$$

$$\left\{ \begin{array}{l} C_{zx}^e = \frac{v}{36V_e}(-q_i s_j + s_i q_j) \\ C_{zy}^e = \frac{v}{36V_e}(-r_i s_j + s_i r_j) \\ C_{zz}^e = \frac{v}{36V_e}(q_i q_j + s_i s_j + r_i r_j) + \frac{\sigma}{\Delta t} \frac{m}{20} V_e \\ C_{z\varphi}^e = \frac{\sigma}{24} s_j \end{array} \right. \quad (2-80)$$

$$\left\{ \begin{array}{l} C_{\varphi x}^e = \frac{\sigma}{24\Delta t} q_i \\ C_{\varphi y}^e = \frac{\sigma}{24\Delta t} r_i \\ C_{\varphi z}^e = \frac{\sigma}{24\Delta t} s_i \\ C_{\varphi\varphi}^e = \frac{\sigma}{36V_e}(q_i q_j + s_i s_j + r_i r_j) \end{array} \right. \quad (2-81)$$

$$[F_i^e] = [F_{xi}^e \quad F_{yi}^e \quad F_{zi}^e \quad 0] \quad (i = K, M, N, L) \quad (2-82)$$

$$\left\{ \begin{array}{l} F_{xi}^e = \frac{1}{4} J_x V_e \\ F_{yi}^e = \frac{1}{4} J_y V_e \\ F_{zi}^e = \frac{1}{4} J_z V_e \end{array} \right. \quad (2-83)$$

$$D_{xx}^e = D_{yy}^e = D_{zz}^e = \frac{\sigma}{\Delta t} \frac{m}{20} V_e \quad (2-84)$$

$$\left\{ \begin{array}{l} D_{\varphi x}^e = \frac{\sigma}{24\Delta t} q_i \\ D_{\varphi y}^e = \frac{\sigma}{24\Delta t} r_i \\ D_{\varphi z}^e = \frac{\sigma}{24\Delta t} s_i \end{array} \right. \quad (2-85)$$

For the element  $e$ , a block stiffness matrix with the size of  $4 \times 4$  is formulated,

$$[S^e] = \begin{bmatrix} S_{11}^e & S_{12}^e & S_{13}^e & S_{14}^e \\ S_{21}^e & S_{22}^e & S_{23}^e & S_{24}^e \\ S_{31}^e & S_{32}^e & S_{33}^e & S_{34}^e \\ S_{41}^e & S_{42}^e & S_{43}^e & S_{44}^e \end{bmatrix} \quad (2 - 86)$$

which contains the contribution of this element to these four nodes. The load vector  $[F^e]$  and the matrix  $[D^e]$  are calculated in a similar way. These local matrixes and vectors are finally assembled to the global matrixes and vectors according to the global indexes of these nodes.

## 2.1.5 Handling Nonlinear Materials

In practical problems, nonlinear magnetic materials are generally included, such as the iron material. Because of the varying magnetic reluctivity, the stiffness matrix is no longer fixed and should be updated along with the solution of magnetic potential. The NR method, which has second order rate of convergence, is an efficient approach to solve nonlinear problems [B22]. In this method, the first order derivative of the nonlinear equations is used to linear the problem approximately.

From the equation (2 – 43), it is found that the curl-curl operator and the Gauge term contain nonlinear part, hence the magnetostatic problem is sufficient to illustrate the implementation of NR method. The weighting integral of the governing equation of magnetostatic problem is given as follows,

$$\int_V [(v \nabla \times \mathbf{A} \cdot \nabla \times \mathbf{W}) + (v \nabla \cdot \mathbf{A}) \nabla \cdot \mathbf{W}] dV = \int_V \mathbf{W} \cdot \mathbf{J} dV \quad (2 - 87)$$

The elemental Jacobian matrix is derived by calculating the first-order derivative to unknowns,

$$\begin{aligned} J_{gh}^e &= \int_V v (\nabla \times \mathbf{N}_g \cdot \nabla \times \mathbf{N}_h) dV + \int_V v (\nabla \cdot \mathbf{N}_g \nabla \cdot \mathbf{N}_h) dV \\ &+ \int_V v \frac{\partial v}{\partial A_h} (\nabla \times \mathbf{N}_g \cdot \nabla \times \mathbf{A}) dV + \int_V v \frac{\partial v}{\partial A_h} (\nabla \cdot \mathbf{N}_g \nabla \cdot \mathbf{A}) dV \end{aligned} \quad (2 - 88)$$

where,

$$\frac{\partial v}{\partial A_h} = \frac{\partial v}{\partial B} \frac{\sqrt{(\nabla \times \mathbf{A}, \nabla \times \mathbf{A})}}{\partial A_h} \quad (2-89)$$

The  $\partial v / \partial B$  is calculated with the  $B - H$  curve of the nonlinear material, which is interpolated from the discrete points by the spline function. The detailed entries of the Jacobian matrix are given as follows:

$$\frac{\partial f_{xi}}{\partial A_{xj}} = \frac{v}{36V_e} (r_i r_j + s_i s_j + q_i q_j) + \frac{1}{vB} \frac{\partial v}{\partial B} s f_{xi} \times st_{xj} \quad (2-90)$$

$$\frac{\partial f_{xi}}{\partial A_{yj}} = \frac{v}{36V_e} (-r_i q_j + q_i r_j) + \frac{1}{vB} \frac{\partial v}{\partial B} s f_{xi} \times st_{yj} \quad (2-91)$$

$$\frac{\partial f_{xi}}{\partial A_{zj}} = \frac{v}{36V_e} (-s_i q_j + q_i s_j) + \frac{1}{vB} \frac{\partial v}{\partial B} s f_{xi} \times st_{zj} \quad (2-92)$$

$$\frac{\partial f_{yi}}{\partial A_{xj}} = \frac{v}{36V_e} (-q_i r_j + r_i q_j) + \frac{1}{vB} \frac{\partial v}{\partial B} s f_{yi} \times st_{xj} \quad (2-93)$$

$$\frac{\partial f_{yi}}{\partial A_{yj}} = \frac{v}{36V_e} (r_i r_j + s_i s_j + q_i q_j) + \frac{1}{vB} \frac{\partial v}{\partial B} s f_{yi} \times st_{yj} \quad (2-94)$$

$$\frac{\partial f_{yi}}{\partial A_{zj}} = \frac{v}{36V_e} (-s_i r_j + r_i s_j) + \frac{1}{vB} \frac{\partial v}{\partial B} s f_{yi} \times st_{zj} \quad (2-95)$$

$$\frac{\partial f_{zi}}{\partial A_{xj}} = \frac{v}{36V_e} (-q_i s_j + s_i q_j) + \frac{1}{vB} \frac{\partial v}{\partial B} s f_{zi} \times st_{xj} \quad (2-96)$$

$$\frac{\partial f_{zi}}{\partial A_{yj}} = \frac{v}{36V_e} (-r_i s_j + s_i r_j) + \frac{1}{vB} \frac{\partial v}{\partial B} s f_{zi} \times st_{yj} \quad (2-97)$$

$$\frac{\partial f_{zi}}{\partial A_{zj}} = \frac{v}{36V_e} (r_i r_j + s_i s_j + q_i q_j) + \frac{1}{vB} \frac{\partial v}{\partial B} s f_{zi} \times st_{zj} \quad (2-98)$$

where;  $f_{xi}$ ,  $f_{yi}$ , and  $f_{zi}$  are the weighting integral equations of the weighting function  $N_i$ ; other parameters are defined as

$$st_{xj} = \frac{s_j}{6V_e} \left( \frac{\partial A_x}{\partial z} - \frac{\partial A_z}{\partial x} \right) - \frac{r_j}{6V_e} \left( \frac{\partial A_y}{\partial x} - \frac{\partial A_x}{\partial y} \right) \quad (2 - 99)$$

$$st_{yj} = -\frac{s_j}{6V_e} \left( \frac{\partial A_z}{\partial y} - \frac{\partial A_y}{\partial z} \right) + \frac{q_j}{6V_e} \left( \frac{\partial A_y}{\partial x} - \frac{\partial A_x}{\partial y} \right) \quad (2 - 100)$$

$$st_{zj} = \frac{r_j}{6V_e} \left( \frac{\partial A_z}{\partial y} - \frac{\partial A_y}{\partial z} \right) - \frac{q_j}{6V_e} \left( \frac{\partial A_x}{\partial z} - \frac{\partial A_z}{\partial x} \right) \quad (2 - 101)$$

$$sf_{xj} = vV_e \left[ st_{xj} + \frac{q_j}{6V_e} \left( \frac{\partial A_x}{\partial x} + \frac{\partial A_y}{\partial y} + \frac{\partial A_z}{\partial z} \right) \right] \quad (2 - 102)$$

$$sf_{yj} = vV_e \left[ st_{yj} + \frac{r_j}{6V_e} \left( \frac{\partial A_x}{\partial x} + \frac{\partial A_y}{\partial y} + \frac{\partial A_z}{\partial z} \right) \right] \quad (2 - 103)$$

$$sf_{zj} = vV_e \left[ st_{zj} + \frac{s_j}{6V_e} \left( \frac{\partial A_x}{\partial x} + \frac{\partial A_y}{\partial y} + \frac{\partial A_z}{\partial z} \right) \right] \quad (2 - 103)$$

The element Jacobian matrixes are calculated separately and are assembled to the global Jacobian matrix as the linear problem. The unknowns involved in the linearized equations are arranged in a residual vector, and the exact solution is approximated after several iterations. The iteration of NR method, which is formulated as

$$\begin{cases} \mathbf{J}\mathbf{a}^{(k+1)}\Delta\mathbf{A}^{(k+1)} = -\mathbf{f}^{(k+1)} \\ \mathbf{A}^{(k+1)} = \mathbf{A}^{(k)} + \Delta\mathbf{A}^{(k+1)} \end{cases} \quad (2 - 104)$$

will terminate when the convergence criterion

$$\left[ -\mathbf{f}^{(k+1)} \right]^2 \leq \varepsilon \quad (2 - 105)$$

is met.  $\mathbf{J}\mathbf{a}$  is the global Jacobian matrix;  $[-\mathbf{f}^{(k+1)}]$  is the residual vector;  $\varepsilon$  is the predefined control error.

## 2.1.6 Numerical examples

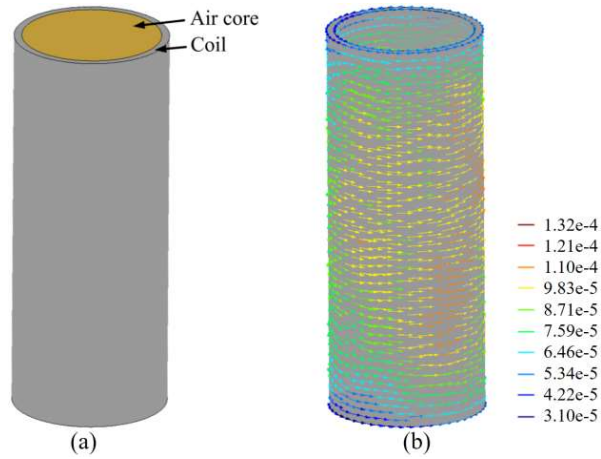


Fig. 2.3. (a) The geometry of the solenoid with an air core. (b) The magnetic vector potential derived by the FEM.

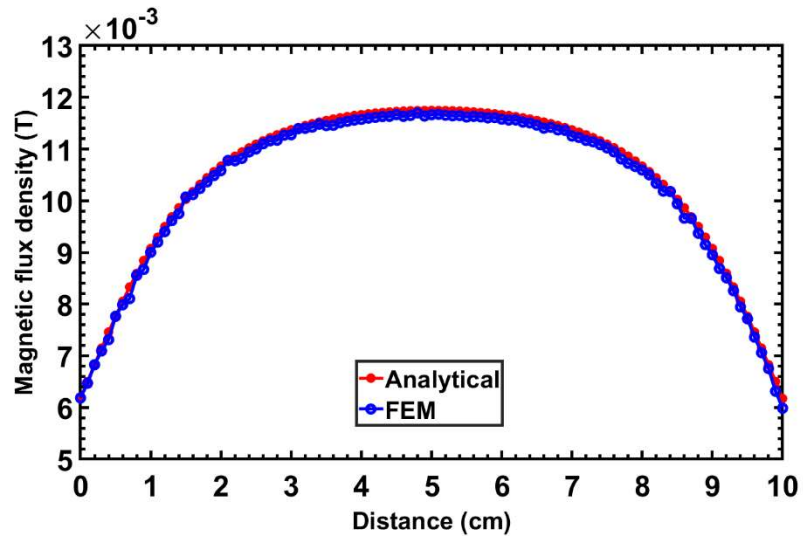


Fig. 2.4. The magnetic flux density along the axis of the air core.

The numerical example is to solve the magnetic field of a solenoid [B23], which has an air core, as shown in Fig. 2.3. The height ( $h$ ), out radius ( $r_2$ ) and inner radius ( $r_1$ ) of the coil, in which 1000 ampere-turns ( $In$ ) are applied, are  $0.1m$ ,  $0.002m$ , and  $0.0018m$ , respectively. In the numerical model, a sphere with the radius of  $0.5m$  is set as the computational domain for this problem, and homogeneous Dirichlet boundary conditions are specified on the surface. The calculated magnetic vector potential on the coil surface, which is shown in Fig. 2.3 (b), is in good agreement with the direction of the current in the coil. In addition, the numerical solution for the magnetic flux density on the solenoid axis is compared with the analytical solution,

which is given by [B24]

$$B = \frac{\mu_0 I n}{2(r_2 - r_1)} \left[ x_2 \ln \left( \frac{\sqrt{r_2^2 + x_2^2} + r_2}{\sqrt{r_1^2 + x_2^2} + r_1} \right) - x_1 \ln \left( \frac{\sqrt{r_2^2 + x_1^2} + r_2}{\sqrt{r_1^2 + x_1^2} + r_1} \right) \right] \quad (2 - 106)$$

where;  $x_2$  is the distance from the bottom of the solenoid to the measuring point;  $x_1$  is equal to  $x_2 - h$ . As shown in Fig. 2.4, the analytical solution and the numerical solution are plotted in red color and blue color, respectively. It can be seen that sufficiently accurate solutions are derived by the FEM solver.

## 2.2 The FEM for Thermal Field Analysis and Coupled Magneto-Thermal Field Analysis

### 2.2.1 Thermal Field Analysis

Heat is another form of energy, and it is transferred from high temperature region to low temperature region by conduction, convection and radiation. In the heat conduction process, the heat is transferred by movement of electrons and microscopic collisions of particles. In the fluids, such as liquid and gas, heat is transferred by the movement of fluids, and this convection process is accompanied by the heat conduction. In the heat radiation process, heat is emitted by electromagnetic radiation. In electromagnetic devices, the heat dissipated by radiation is relatively small, hence this process is generally neglected in the thermal analysis.

In addition to the thermal resistance based lumped-parameter thermal network [B25], numerical methods, such as FEM and finite volume method (FVM), are widely used in the thermal field analysis [B26]. Based on the conservation of heat and the Fourier's law, the governing equation for heat conduction in solids is formulated with the partial differential equation,

$$\nabla \cdot \lambda \nabla T = -Q + \rho c \frac{\partial T}{\partial t} \quad (2 - 107)$$

where;  $\lambda$  is the thermal conductivity ( $W/(m \cdot K)$ ) ;  $T$  is temperature ( $K$ ), i.e. the potential function of thermal field;  $Q$  is the heat source ( $W$ );  $\rho$  is density ( $kg/m^3$ ) ;  $c$  is the specific heat capacity ( $J/(kg \cdot K)$ ). The left-hand-side represents the transferred heat, while these two terms in the right-hand-side are the generated heat and the heat change owing to the temperature variations. With appropriate boundary and initial conditions, the thermal conduction problem can be solved with the Galerkin FEM. Compared with magnetic field, the governing equation of thermal field is simpler, as there is only one DoF on each node. Like the ESP, the temperature is expanded with the shape functions,

$$T \approx \sum_{j=1}^n T_j N_j \quad (2 - 108)$$

To illustrate the calculation process, a generic problem is constructed in region  $\Omega$ , which considers three common boundary conditions on  $\Gamma_1$ ,  $\Gamma_2$ , and  $\Gamma_3$

$$\nabla \cdot \lambda \nabla T + Q - \rho c \frac{\partial T}{\partial t} = 0 \quad (2 - 109)$$

$$\begin{cases} \Gamma_1: T = T_g & (a) \\ \Gamma_2: \lambda \frac{\partial T}{\partial n} + q_g = 0 & (b) \\ \Gamma_3: \lambda \frac{\partial T}{\partial n} + a_s T = a_s T_0 = q & (c) \end{cases} \quad (2 - 110)$$

With the weighting function  $W$ , the weighting integral of the residual of the governing equation reads,

$$\int_{\Omega} W \left( \nabla \cdot \lambda \nabla T + Q - \rho c \frac{\partial T}{\partial t} \right) d\Omega = 0 \quad (2 - 111)$$

Rewrite the equation with the Gauss theorem

$$\begin{aligned} & \int_{\Omega} \lambda \nabla W \cdot \nabla T d\Omega - \int_{\Omega} W \left( Q - \rho c \frac{\partial T}{\partial t} \right) d\Omega \\ & + \int_{\Gamma_2} W q_g dS + \int_{\Gamma_3} W a_s (T - T_0) dS = 0 \end{aligned} \quad (2 - 112)$$

Substituting boundary equations into equation (2-112) yields

$$\begin{aligned}
& \int_{\Omega} \lambda \nabla W \cdot \nabla T d\Omega + \int_{\Omega} W \rho c \frac{\partial T}{\partial t} d\Omega + \int_{\Gamma_3} W a_s T dS \\
& = \int_{\Omega} W Q d\Omega - \int_{\Gamma_2} W q_g dS + \int_{\Gamma_3} W a_s T_0 dS = 0 \quad (2 - 113)
\end{aligned}$$

Expanding the temperature with shape functions and discretizing the time derivative with backward difference method derive

$$\begin{aligned}
& \sum_{j=1}^n T_j^{(k+1)} \lambda \int_{\Omega} \nabla N_i \cdot \nabla N_j d\Omega + \sum_{j=1}^n T_j^{(k+1)} \frac{\rho c}{\Delta t} \int_{\Omega} N_i N_j d\Omega + \sum_{j=1}^n T_j^{(k+1)} a_s \int_{\Gamma_3} N_i N_j dS \\
& = \sum_{j=1}^n T_j^{(k)} \frac{\rho c}{\Delta t} \int_{\Omega} N_i N_j d\Omega + \int_{\Omega} N_i G d\Omega - \int_{\Gamma_2} N_i q_g dS + \int_{\Gamma_3} N_i a_s T_0 dS \quad (2 - 114)
\end{aligned}$$

Rewrite the equation in a compact form:

$$\sum_{j=1}^n S_{ij} T_j^{(k+1)} = F_i \quad (i, j = 1, 2, \dots, n) \quad (2 - 115)$$

where

$$S_{ij} = \lambda \int_{\Omega} \nabla N_i \cdot \nabla N_j d\Omega + \frac{\rho c}{\Delta t} \int_{\Omega} N_i N_j d\Omega + a_s \int_{\Gamma_3} N_i N_j dS \quad (2 - 116)$$

$$F_i = \sum_{j=1}^n T_j^{(k)} \frac{\rho c}{\Delta t} \int_{\Omega} N_i N_j d\Omega + \int_{\Omega} N_i G d\Omega - \int_{\Gamma_2} N_i q_g dS + \int_{\Gamma_3} N_i a_s T_0 dS \quad (2 - 117)$$

In this thesis, the same finite element, namely, the linear tetrahedron, is used to discretize the thermal field. Hence, the shape functions and the identity for the volume integral of shape functions, which are introduced in the former section, are also applied to the matrixes calculation of thermal field. In addition, an identity for the surface integral of shape functions is given,

$$\int_{\Gamma_3} N_i N_j dS = \frac{m_{\Gamma_3}}{12} S_{\Gamma_3} \quad \begin{cases} m = 2, i = j \\ m = 1, i \neq j \end{cases} \quad (2 - 118)$$

$$\int_{\Gamma_3} N_i dS = \frac{1}{3} S_{\Gamma_3} \quad (2 - 119)$$

Based on these identities, the entries  $S_{ij}$  and  $F_i$  are calculated as

$$S_{ij} = \frac{\lambda}{36V_e} (q_i q_j + s_i s_j + r_i r_j) + \frac{\rho c m_\Omega}{20\Delta t} V_e + \frac{a_s m_{\Gamma_3}}{12} S_{\Gamma_3} \quad (2 - 120)$$

$$F_i = \sum_{j=1}^n T_j^{(k)} \frac{\rho c m_\Omega}{20\Delta t} V_e + \frac{1}{4} G V_e - \frac{1}{3} q_g S_{\Gamma_2} + \frac{1}{3} a_s T_0 S_{\Gamma_3} \quad (2 - 121)$$

The second term of  $S_{ij}$  and the first term of  $F_i$ , which contain the time step  $\Delta t$ , represent the transient process. The contribution of boundary surfaces is specified to the related nodes, and there is no need for those internal elements to calculate the terms related to boundary surfaces. To showcase the details, the contribution of a face  $KMN$  on the boundary  $\Gamma_3$  is given,

$$S_{ij}^3 = \begin{bmatrix} \frac{2a_s}{12} S_{\Gamma_3} & \frac{a_s}{12} S_{\Gamma_3} & \frac{a_s}{12} S_{\Gamma_3} & 0 \\ \frac{a_s}{12} S_{\Gamma_3} & \frac{2a_s}{12} S_{\Gamma_3} & \frac{a_s}{12} S_{\Gamma_3} & 0 \\ \frac{a_s}{12} S_{\Gamma_3} & \frac{a_s}{12} S_{\Gamma_3} & \frac{2a_s}{12} S_{\Gamma_3} & 0 \\ 0 & 0 & 0 & 0 \end{bmatrix} \quad (2 - 122)$$

It is noted that all the boundary conditions, except the first one, are integrated into the weak formulation after the transformation. Before the assembly, the DoFs of nodes on the Dirichlet boundary are removed from the unknown list and the right-hand-side vector is modified to take these DoFs into consideration. The related columns and rows in the stiffness matrix are deleted to maintain the equivalence between the number of equations and the number of unknowns.

## 2.2.2 Coupled Field Analysis

Thermal analysis has attracted increasing attentions in the design of electromagnetic devices to acquire high efficiency, small size, large capacity, and strong stability [B27]. In addition, an accurate thermal analysis is crucial for the device operation and the decision making [B28]. During operation, the losses, which are

generated in the active parts, are dissipated to the ambient and the temperature of device rises in the meantime. The temperature rise is directly determined by the losses, and the losses are critically temperature-dependent. Hence, the thermal field and the electromagnetic field should be analyzed simultaneously. In addition, the heat transfer process is strongly coupled with the fluid flow in some devices, such as the transformers and the water cooled motors [B29]. To derive an accurate solution, the fluid field should be considered in the thermal field analysis. The governing equations for the convection heat transfer of fluid and the related calculation process are covered in the following section. Numerical methods, which can handle different fields, complex geometries, nonlinear materials, and transient problems, have been applied in the coupled field analysis [B30].

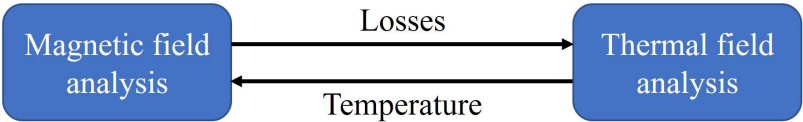


Fig. 2.5. The coupled magneto-thermal field analysis

Owing to the complicated coupling between fields, indirect coupling is generally adopted in the analysis. In other words, these two fields are solved separately and iteratively. As shown in Fig. 2.5, the magnetic field is solved with a predefined temperature, and the derived solution is used to calculate the loss distribution, which is transferred to the thermal field as the heat sources. The thermal field is solved based on the current losses, and the calculated temperature distribution is transferred to the magnetic field solver to update the temperature-dependent parameters, such as the electric conductivity and the magnetic permeability. The magnetic field is recalculated with these updated parameters. These two fields are solved iteratively until the predefined convergence criterion for temperature or loss is met.

To facilitate the design and analysis of electromagnetic devices, the FEM solver for thermal field has been added in several commercial electromagnetic field simulation software packages, such as the Infolytica Magnet/Thermnet [B31] and

JMAG [B32]. In addition, some universal simulation platform, such as the ANSYS Workbench [B33] and the COMSOL Multiphysics [B34], can handle more complicated problems, like the turbulent heat transfer.

Two categories of approaches are generally adopted in the numerical methods to solve the coupled magneto-thermal field. The first approach to deal with the coupling is to build the FE spaces for these two fields with one set of mesh. With this strategy, the memory space and meshing time for a second mesh are not required, and the data transfer between fields is readily accomplished. The major drawbacks are the unnecessary waste of computational work and the potential convergence problems, which are resulted by the different requirements for discretization. Solving each field with different meshes is the other common approach. This approach requires more storage resources and an additional mapping algorithm for different meshes, which may introduce extra errors to the solution [B35]. Compared with the former coupling approach, this approach is relatively robust by sacrificing precision and storage resources. In the ANSYS Workbench, the barycenter of elements, which are read from the fluid field solver Fluent, is mapped to the mesh used in the Maxwell solver to read the corresponding loss. This mapping algorithm is so coarse that large transfer errors are introduced to the solution. Radial basis function method, and non-matching mesh mapping method, which is based on the Gauss integral and coordinate transformation, are proposed to improve the mapping precision [B36].

The core losses and the cooper losses are considered in the losses calculation. For the core loss, the separation model proposed by Bertotti, which divides the core loss into three components, is given as follows

$$P_{fe} = k_h f B_m^2 + k_c (f B_m)^2 + k_e (f B_m)^{1.5} \quad (2 - 123)$$

where;  $k_h$  is the hysteresis coefficient;  $f$  is the frequency (Hz);  $k_c$  is the classical eddy coefficient; and  $k_e$  is the excess coefficient. In the finite element analysis, the element copper loss is calculated by the following formula

$$P_{cu} = V J^2 / \sigma_t \quad (2 - 124)$$

where;  $V$  is the volume of the element;  $\sigma_t$  is the electric conductivity;  $J$  is the current density.

In the coupled analysis, two material properties related to the electromagnetic field, i.e. the magnetic permeability and the electric conductivity, are modelled with the temperature dependent characteristic. The temperature-dependent electric conductivity is expressed by the following formula

$$\sigma_t = \sigma_0 / (1.0 + k_\sigma \times (T - T_0)) \quad (2 - 125)$$

where;  $\sigma_0$  is the referenced electric conductivity at temperature  $T_0$ ;  $k_\sigma$  is the temperature coefficient of electric conductivity. The temperature-dependent permeability of steel is represented by the following formula

$$\mu_t = \mu_0 (1.0 + k_\mu \times (T - T_0)) \quad (2 - 126)$$

where;  $\mu_0$  is the referenced magnetic permeability at temperature  $T_0$ ;  $k_\mu$  is the temperature coefficient of magnetic permeability.

## **2.3 The Analysis and Design of Power Transformers**

### **2.3.1 The Analysis of Power Transformers**

Power transformers have served as the main electrical equipment in alternating current power systems since last century and still play a vital role in modern High Voltage Direct Current system as the connector between systems. According to the insulating medium, the transformers are classified into oil-immersed transformers, dry type transformers, and resin type transformers [B37]. For high- power and high-voltage applications, oil-immersed transformer is the most commonly used type, and the mineral oil is a good coolant as well. Based on the cooling method, oil-immersed transformers are classified into three categories, natural oil cooling (ON) transformer,

oil forced cooling (OF) transformer, and oil directed cooling (OD) transformer. Combined with the external cooling medium and its circulation mechanism, a four-letter code, like ONAF for oil natural air forced transformer, is generally used to express the identification of oil-immersed transformers. Without any auxiliary equipment for oil circulation, the structure of ON transformer is simple, making for a highly stable operation. The natural convection is drifted by the lift force generated by the density discrepancy of oil. In OF transformers, the velocity of flow in cooling equipment is increased by the oil pumps, while there is still a thermosiphon flow in the windings. The OD technique, in which the oil is pumped and directed to flow through the cooling ducts in the winding, is used to reduce the hot-spot temperature. The accurate analysis of the power transformers is crucial for the design optimization, safe operation and decision making [B28]. Several areas are involved in the analysis, such as the electromagnetic analysis, the thermal analysis, and the insulation analysis. In some cases, the coupling analysis is used to cope with the naturally coupled field in transformers [B38, B39].

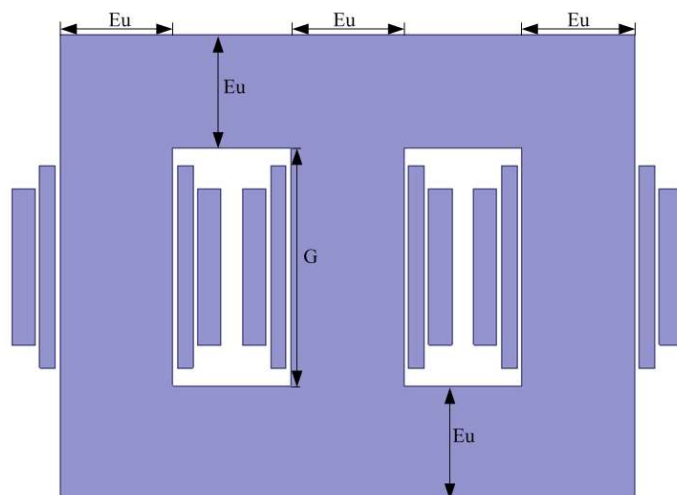


Fig. 2.6. Front view of the transformer.

Magnetic circuit method is a common approach for the magnetic field analysis. A three-phase, dry type power transformer, which is rated at  $30MW$ ,  $115kV/13.8kV$ ,  $60Hz$ , is used to illustrate the analysis process of power transformers. The high-

voltage winding and the low-voltage winding are connected in delta and star, respectively. The front view of this transformer is given in Fig. 2.6, in which  $E_u$  and  $G$  represent the thickness of the core leg and the height of the window. In addition, the deepness of the transformer is notated by  $D$ .

With the given dimensions, the cross-section area of core can be computed as

$$S_c = D \times E_u \quad (2 - 127)$$

The volts per turn is computed as follows:

$$VPT = \frac{13800}{\sqrt{3}N_2} \quad (2 - 128)$$

where  $N_2$  is the number of low-voltage winding turns. Then the magnetic flux density is given by

$$B_m = \frac{VPT}{4.44fS_c} \quad (2 - 129)$$

This formula is based on an assumption that the magnetic field is evenly distributed in the core. This procedure can be replaced by the finite element analysis to derive a more accurate field [B40-B42]. Moreover, FEM is also used in combination with optimization methods for the design optimization of transformers [B43].

If the number of high-voltage winding turns is not given, it can be computed according to the transformation ratio,

$$N_1 = \frac{115000}{VPT} \quad (2 - 130)$$

It is worth noting that the windings are connected in different modes. The following analysis on losses are based on the solution of magnetic field and the detailed dimensions. The volume of core is calculated from the following equation,

$$V_c = E_u \times (6E_u + 4W + 3G) \times D \quad (2 - 131)$$

According to the magnetic flux density and the interpolated  $B$ -loss curve for the frequency, the total core losses of this transformer are derived by

$$P_c = P_v \times V_c \quad (2 - 132)$$

where  $P_v$  is the core loss per volume at the specific magnetic flux density.

The copper losses are calculated in a similar way, and the first step is to compute the dimensions of these two windings. The height of winding is derived with the distance to core and the height of window,

$$TD_{LV} = G - 2D_{LV-C} \quad (2 - 132)$$

$$TD_{HV} = G - 2D_{HV-C} \quad (2 - 133)$$

where;  $D_{LV-C}$  is the distance between core and secondary winding;  $D_{HV-C}$  is the distance between core and primary winding. Then the width of winding is to be determined, in which the wire type is considered. The primary and secondary windings are wound by copper wire with the diameter of  $d_{HV}$  and copper sheet with the thickness of  $t_{LV}$ , respectively. The number of wire layers in the primary winding is calculate based on its height and the number of turns,

$$Layers_{HV} = \frac{N_1}{TD_{HV}/d_{HV}} \quad (2 - 134)$$

The width of winding is derived from the following equation,

$$W_{LV} = t_{LV-C} \times N_2 \quad (2 - 135)$$

$$W_{HV} = d_{HV} \times Layers_{HV} \quad (2 - 136)$$

The length of winding is approximately calculated by

$$L_{LV} = \pi(W_{LV} + 2W_{LV-C} + E_u) \quad (2 - 137)$$

$$L_{HV} = \pi(2W_{LV} + 2W_{LV-C} + 2W_{LV-HV} + E_u + W_{HV}) \quad (2 - 138)$$

where;  $W_{LV-C}$  is the width between core and secondary winding;  $W_{LV-H}$  is the width between secondary winding and primary winding. With all the dimensions of windings determined, the volume of winding is obtained,

$$V_{LV} = TD_{LV} \times 2W_{LV} \times W_{LV} \times 3 \quad (2 - 139)$$

$$V_{HV} = \frac{\pi \times d_{HV} \times d_{HV} \times L_{HV} \times N_1}{4} \times 3 \quad (2 - 140)$$

Then the copper losses for these two windings are calculated by

$$P_{LV} = V_{LV}J_{LV}^2/\sigma_t \quad (2 - 141)$$

$$P_{HV} = V_{HV}J_{HV}^2/\sigma_t \quad (2 - 142)$$

where  $J$  is the current density of winding. The main components of transformer losses are obtained with these analytical formulas, while other losses, such as stray losses on the tank and structures, are neglected in the analysis. In some cases, the stray losses have a significant effect on the hot-spot temperature, and should be treated carefully. Other parameters, like the impedance voltage, can be derived with the related analytical approaches.

Based on the solution of electromagnetic field, the thermal analysis of transformer can be conducted by analytical methods in combination with empirical coefficients. In oil-immersed transformers, the average winding temperature-rise is calculated with the gradient and the average oil temperature-rise [B37]. The empirical equation for the gradient is formulated with the thermal load per surface, which equals to the quotient of copper loss to the effective heat dissipation area. Generally, the empirical equation is only suitable for a certain type of transformer, and the coefficients require modification to fit different dimensions. For ON transformers, the average oil temperature-rise is determined by a similar approach as the winding, while the oil flow should be considered for the OF transformers. The average oil temperature-rise of OF transformers is formulated with the volume flow rate and the cooling capacity of chiller, when the head of the oil pump is equal to the total resistance [B44]. According to the flow path, the entire cooling system is split into several parts, which are calculated separately with specific formulas. Because of the complex fluid field, these analytical formulas are not very accurate. In addition, detailed temperature distribution, like the hot-spot temperature, cannot be obtained with this type of method.

It is well known that high temperature accelerates the aging of dielectric, which reduces the service life of power transformer and may cause severe faults [B28]. As the dominating heating component, the overheating problem of windings has attracted increasing attentions [B45]. Thermal network method [B46, B47] and numerical

methods [B48-B53] are applied to model the isolated windings to give an accurate estimation of the temperature-rise at hot-spot. To reduce the size of computational domain and the complexity of problem, heat-run test is used to derive the inlet flow rate of the windings. The bottom oil temperature is specified as the other parameter of the inlet boundary condition, and the inlet oil flow rate is iterated until the calculated average winding temperature-rise is matched with the measured value. Hence, the winding is isolated from the rest of the cooling system.

The thermal network model consists of two sub-models, the hydraulic sub-model and the heat conduction sub-model. The mass flow rate distribution in the cooling ducts is obtained with the first sub model, and the heat conduction sub-model is to calculate the temperature distribution in the winding. Since the oil flow and the heat transfer is strongly coupled, these two sub-models are coupled through the boundary conditions on the liquid-solid interfaces and are solved iteratively until meeting the convergence criterion. On account of the complexity of numerical analysis for flow field, the hydraulic sub-model is analytically built based on the mass and pressure loss conservation, while the heat conduction in winding is analyzed either numerically or analytically. For winding with several passes, either successive analysis of passes or building a whole model for all the passes is accepted.

As reported in the former paragraph, the computing costs for numerical heat transfer analysis of windings, in which the fluid domain is taken into consideration, is much higher than the analytical method. Tens of millions grids are required to discretize the 2D winding model [B48], and the number will increase to hundreds of millions for 3D model [B49]. Limited by the computing equipment, the numerical analysis was not widely applied in the thermal analysis of transformers. However, with the advancement of computer technology and parallel algorithms, numerical software is widely used in the thermal field analysis, in which the heat transfer in solids and liquids is coupled in a numerical model and solved by the fluid field solver.

Since the oil velocity in ON transformers is small, the flow is laminar. These three conservation equations for the laminar flow are given by

Continuity,

$$\nabla \cdot (\rho \mathbf{V}) = 0 \quad (2 - 143)$$

Momentum and,

$$\nabla \cdot (\rho \mathbf{V} \mathbf{V}) = -\nabla P + \nabla \cdot (\mu \nabla \mathbf{V}) + \rho \mathbf{g} \quad (2 - 144)$$

Energy,

$$\nabla \cdot (\rho \mathbf{V} C T) = \nabla \cdot (k \nabla T) + S_e \quad (2 - 145)$$

where;  $P$  is the pressure;  $\mathbf{g}$  is the gravity vector;  $\mathbf{V}$  is the velocity vector;  $S_e$  is the heat source. For turbulent flow, extra models for the turbulence are required and are solved along with these three equations for the conservation of continuity, momentum and energy.

In addition, the radiator is isolated from the rest of power transformer, and the numerical model [B54] and semi-analytical reduced model [B55] are used to analyze the radiator performance. To cope with the coupled problem existing in transformers, a coupling analysis that involving thermal, fluid and electromagnetic field was conducted for a three-phase medium-power dry-type power transformer, and the numerical solution is validated by the experimental temperature-rise test [B30].

### 2.3.2 Power Transformer Design Optimization

Transformer design optimization has received considerable attentions with the development of power industry [B1]. The most commonly used objective functions of TDO are to minimize the manufacturing cost and to minimize the total owing cost. According to the objective functions, the cost of each part should be measured with the market price. Under some circumstances, there are always more than one objectives to be optimized through transformer design process, such as manufacturing cost, total owing cost, loss, efficiency, and temperature rise, which is a typical multi-objective optimization problem [B56-B59]. Multi-objective optimization aims to find

a set of optimal solutions among all the conflicting objectives under certain constraints, which are supplied to the transformer manufacturer. These optimal solutions are called Pareto solutions, which are different from the single solution obtained in the single-objective optimization problem. In addition, there are several constraints to be met for all the candidates. International technical specifications on transformers, like IEC 60076-1, IEC 60076-2, IEC 60076-3 and IEC 60076-5, are the main constraints to satisfy. Another possible set of constraints stems from the needs of customer, such as the dimension limits.

Design based on the analytical model, which is introduced in the former section, is the most commonly used approach in industry [B37, B60]. For optimization problems of integer variables, all candidates should be evaluated to ensure the validity of optimal solution, while it is impossible to enumerate all the combinations for continuous variables. Another weakness of this method is the low accuracy of analytical transformer model, which may lead to wrong solutions. Many optimization algorithms, such as mixed integer programming, branch and bound technique, genetic algorithms, steepest descent method and evolution approaches, are applied in the TDO [B37]. To obtain an accurate evaluation of the transformer characteristics, FEM is used in the entire design process or the final validation process.

The thermal design of power transformers is also investigated in many studies. Based on the analytical model of ONAN transformer windings, the effects that geometrical parameters, flow arrangement, and mass flow rate have on the heat transfer performance were investigated, which gives a guidance for the subsequent design of windings [B47]. In addition, the optimization of radiator is performed with the numerical simulation tool, ANSYS Fluent, and an optimized radiator with optimum length of sections and optimum spacing between sections are derived. The cooling capacity is improved by 14% when compared with the existing design [B61]. To attain the goal of cooling optimization of power transformers, six different geometric configurations of a power transformer are numerically studied with six different flow rates imposed on the inlet. In this study, the temperature dependent characteristics of fluid properties and boundary conditions are taken into consideration

[B51]. In [B38], the genetic algorithm is combined with the CFD to obtain an optimal configuration of the cooling ducts and windings. The losses are calculated by the coupled CFD-electromagnetic 3D model, in which anisotropic and temperature-dependent quantities are specified for the thermal properties. An optimal positioning of the air ducts and winding is obtained, and the hot-spot temperature is reduced along with an overall heat transfer performance improvement when compared with the current transformer.

## 2.4 Literature Review of Nanofluid

Mineral oil is the most commonly used coolant and dielectric in oil-immersed power transformers, especially for high-power and high-voltage transformers. Owing to the inherently low thermal conductivity, oil pumps are introduced into the OF and OD transformers to improve the cooling performance by increasing the oil velocity. However, the electrification of oil is exacerbated by the increased flow velocity. The accumulated charges may accelerate the aging of insulation board and shorten the service life of transformer [B62].

An innovative approach to improve the heat transfer performance of liquid coolant is to enhance the thermal conductivity by adding solid particles with order-of-magnitude higher thermal conductivity. In 1873, this idea was proposed by Maxwell for the first time, after which many investigations were conducted until Choi et al. produced the colloidal fluid with metallic nanoparticles in 1995 [B63]. The term “nanofluid” was created to represent the colloidal fluid suspended with nanoparticles. The measured thermal property validated the original concept proposed by Maxwell. This innovative approach has been applied in the common coolants, such as water [B64, B65], transformer oil [B66, B67], vegetable oil [B68] and so on. The nanofluids prepared with different nanoparticles and concentrations are tested. In addition, the effect that preparation methods have on the thermal properties of nanofluids is considered in some

studies [B69]. The most commonly concerned nanofluid properties are thermal conductivity, breakdown voltage, viscosity, and dielectric dissipation factor.

The transformer oil based nanofluids have been investigated by many researchers with different types of nanoparticles. C. Choi prepared three kinds of transformer oil based nanofluids with the  $\text{Al}_2\text{O}_3$  and  $\text{AlN}$  nanoparticles [B70]. It is found that the thermal conductivity of nanofluids is in positive correlation with the thermal conductivity of nanoparticles and the volume fraction. In [B71], the multi-walled carbon nanotubes are dispersed in the transformer oil in two mass concentrations of 0.001 and 0.01%. An experimental set-up was designed to resemble the oil-immersed transformer, and the performance of nanofluids under natural and forced convection is experimentally studied. In this study, eight properties or parameters, namely, thermal conductivity, viscosity, breakdown voltage, electrical conductivity, density, shear stress, flash point, and pour point, are determined. The thermal conductivity increases with the rising concentration, while the effect that temperature has on the thermal conductivity is not monotonous. Once the temperature is higher than a specific value, about 60 degrees centigrade, a dramatic decrease in the thermal conductivity is observed with the increasing temperature. As expected, there is a dramatic decrease in the breakdown voltage after adding multi-walled carbon nanotubes, and this phenomenon is aggravated by the increasing concentration. To tackle the potential deterioration in insulating property, ceramic nanoparticles with higher relative permittivity are used to prepare the nanofluids. In [B72], the transformer oil based nanofluids are prepared using Zirconia( $\text{ZrO}_2$ ) and Titania( $\text{TiO}_2$ ), and their dielectric and thermal properties are measured. The AC breakdown voltages and impulse breakdown voltages of all the nanofluids, except the AC breakdown voltage of the  $\text{TiO}_2$  nanofluid at 0.05%wt, witnessed a significant growth when compared with the base oil.

The preparation methods for nanofluids are classified to two categories, the single-step method and the two-step method [B69]. In the single-step method, the development and the dispersion of nanoparticles are conducted at the same time. Using this method, a stable suspension can be derived with a relatively higher cost. In the two-step method, the nanoparticles are prepared separately and then dispersed into the base fluid by

ultrasonic dissolution, ball milling, magnetic stirring, or high-shear mixing. Compared with the first method, the application of the two-step method is more broad [B73].

To facilitate the preparation of nanofluids and the subsequent simulation, many models, based on theoretical analysis or experimental data, are proposed to express the equivalent properties of nanofluids [B74]. Except for the concentration and the properties of nanoparticles, some other parameters, such as the dimension of nanoparticles, may be used to present the microscopic phenomenon in nanofluids. The models for the density, the specific heat, and the thermal expansion coefficient of nanofluid are generally formulated according to the solid-liquid equations, as given by

$$\rho_{nf} = (1 - \phi)\rho_f + \phi\rho_p \quad (2 - 146)$$

$$C_{nf}\rho_{nf} = (1 - \phi)C_f\rho_f + \phi C_p\rho_p \quad (2 - 147)$$

$$\beta_{nf}\rho_{nf} = (1 - \phi)\beta_f\rho_f + \phi\beta_p\rho_p \quad (2 - 148)$$

where;  $\phi$  is the volume fraction of nanoparticles;  $\beta$  is the thermal expansion coefficient; the nanoparticle and nanofluid are noted by the subscript  $nf$  and  $p$ , respectively. Due to the lack of experimental data, the effect that temperature has on these properties is neglected.

To conduct the thermal analysis of nanofluids, there are other two important thermal properties to be determined, i.e. the thermal conductivity and the viscosity. Although various models based on theoretical or experimental analysis have been proposed to estimate these two properties for nanofluid, a uniform model that applies to all the nanofluids does not exist. Lacking consensus on the mechanism of nanofluids, the proposed models should cope with varying parameters, such as the Brownian motion, size, thermal diffusivity, temperature and so on, and this aspect limits the application scenarios of these models. A review on the latest models for thermal conductivity and viscosity is given in [B75].

In this thesis, the Einstein viscosity formula based model [B76], in which the radius of the nanoparticle is considered, is adopted to estimate the viscosity and the thermal conductivity model [B77], which is based on experimental investigations, is

used

$$\mu_{nf} = \mu_f \left[ 1 + 2.5\phi \left( 1 + \frac{8.868}{r} \right) \right] \quad (2 - 149)$$

$$k_{nf} = k_f \left[ 1 + 4.4Re_p^{0.4} Pr_f^{0.66} \left( \frac{T}{T_{fr}} \right)^{10} \left( \frac{k_p}{k_f} \right)^{0.03} \phi^{0.66} \right] \quad (2 - 150)$$

where;  $Pr$  is the Prandtl number;  $T_{fr}$  is the freezing point of the carrier liquid;  $r$  is the average radius of the nanoparticle; the Reynolds number of nanoparticle is given by

$$Re_p = \frac{2\rho_f k_b T}{\pi\mu_f^2 d_p} \quad (2 - 151)$$

where;  $d_p$  is the diameter of the nanoparticle;  $k_b$  is the Boltzmann constant ( $1.38066 \times 10^{-23} \text{ J K}^{-1}$ ). From these two models, it can be found that the thermal conductivity and the viscosity increase after adding nanoparticles, which has been validated in numerous experimental studies. In addition, only the temperature dependence of thermal conductivity is concerned in the model, while other properties are regarded as temperature independent.

In the experimental investigations and numerical studies of nanofluids, the mostly commonly used devices are simple containers, such as tube [B67], cavity [B78], and microchannel heat sink [B79]. Both laminar flow [B80] and turbulent flow [B81] are concerned in the former studies, which give a comprehensive insight for the heat transfer of nanofluids. In the numerical studies, two types of methods are widely employed to analyze the nanofluid flow, and they are the multi-phase method and the single-phase method [B75]. As there are two phases, i.e. the liquid phase and the solid phase (nanoparticle), involved in the nanofluids, the utilization of multi-phase method is straightforward [B79, B82, B83]. Even so, the simple single-phase method is broadly adopted by scholars [B75, B84, B85], and the solution derived with this approach is reasonable as well. In the single-phase method, the nanofluid is regarded as a homogenous mixture with equivalent properties, and these two phases are in thermal equilibrium and flow in the same velocity. In the single-phase method, the governing

equations are formulated for the mixture, and turbulence models are added into the governing equations for the turbulent flow. In the multi-phase method, the differences in velocities and temperatures between phases are considered. The multi-phase method is further classified into two categories, the Lagrangian-Eulerian method and the Eulerian-Eulerian method, which consists of three popular models, the volume of fluid (VOF) model, the mixture model, and the Eulerian model. The Eulerian-Eulerian method is suitable for mixture with large amount of particles. The Eulerian model is a complete multi-phase approach, in which the governing equations are formulated for each phase separately. In the mixture model, the governing equations are formulated for the mixture rather than for each phase. In addition, there is one more conservation equation of the volume fraction in the governing equations. The interaction between phases and the velocity difference are considered in the mixture model by modifying the momentum and energy equations. The VOF model gives shared temperatures and velocities for both phases, while the volume fraction is derived by solving a continuity equation of the second phase. Compared with the single-phase method, more equations are involved in the calculation of multi-phase method, and the requirement for computational resources increases accordingly. In the open literature with experimental validation, the multi-phase method is reported to be more accurate when compared with the single-phase method [B82, B83].

The heat transfer of an oil-immersed distribution transformer after adding carbon nanotubes (CNT) and graphite of different concentrations is studied with the single-phase method [B86]. A 3D slice model is built for the distributor transformer, and transformer oil cooling is included for comparison. Significant improvement on the heat transfer performance was observed from the numerical results. In [B87], the heat transfer characteristics of transformer oil based nanofluid in a transformer is numerically analyzed with the COMSOL. The Eulerian model is used, and the distribution of nanoparticles are derived along with the temperature and velocity. In addition, the hysteresis loop of nanofluid materials should be taken into consideration when conducting the electromagnetic analysis [B88]. A special type of nanofluid, namely, ferrofluid, is prepared with magnetic nanoparticles, and has more applications other than

improving the cooling performance [B89-B91], such as enlarging the torques or forces of electrical machines by filling the gaps [B92, B93].

## 2.5 Summary

The potential formulations for Maxwell equations and heat conduction equations are reviewed along with the detailed discretization process of FEM. The commonly used NR method for nonlinear problems is also included. In addition, these two common coupling strategies for magneto-thermal analysis are presented.

The analytical method used in the transformer analysis and design is reviewed along with the optimization methods. Numerical methods, such as finite element analysis and CFD analysis, have been gradually introduced into the design process to partially or completely replace the analytical models. To reduce the computational burden, isolated parts of transformers, such as windings and radiators, are investigated separately.

This chapter also reviews the studies on transformer oil based nanofluid, such as preparation, measurement, experimental investigations, and numerical analysis. The prediction models for nanofluid properties and the numerical models for nanofluid flows are covered.

## 2.6 Reference-Part B

[B1] E. I. Amoiralis, M. A. Tsili, and A. G. Kladas, "Transformer Design and Optimization: A Literature Survey," *IEEE Trans. Power Del.*, vol. 24, no. 4, pp. 1999-2024, Oct 2009.

[B2] J. E. Flaherty, *Finite Element Analysis Lecture Notes*, Spring, 2000.

[B3] O. Biro, K. Preis, and K. R. Richter, "On the use of the magnetic vector potential in the nodal and edge finite element analysis of 3D magnetostatic problems," *IEEE*

*Trans. Magn.*, vol. 32, no. 3, pp. 651-654, May 1996.

[B4] K. Simonyi, *Theoretische Elektrotechnik*. Berlin: VEB Deutscher Verlag Wissenschaften, 1977.

[B5] H. Igarashi, and T. Honma, "On convergence of ICCG applied to finite-element equation for quasi-static fields," *IEEE Trans. Magn.*, vol. 38, no. 2, pp. 565-568, Mar. 2002.

[B6] B. Weiß, and O. Bíró, "On the convergence of transient eddy-current problems," *IEEE Trans. Magn.*, vol. 40, no. 2, pp. 957-960, Mar. 2004.

[B7] B. Weiß, and O. Bíró, "Multigrid for time-harmonic 3-D eddy-current analysis with edge elements," *IEEE Trans. Magn.*, vol. 41, no. 5, pp. 1712-1715, May 2005.

[B8] J. Gyselinck, P. Dular, C. Geuzaine, and R. V. Sabariego, "Surface-impedance boundary conditions in time-domain finite-element calculations using the magnetic vector-potential formulation," *IEEE Trans. Magn.*, vol. 45, no. 3, pp. 1280-1283, Mar. 2009.

[B9] P. Dular, N. Sadowski, J. P. A. Bastos, and W. Legros, "Dual complete procedures to take stranded inductors into account in magnetic vector potential formulations," *IEEE Trans. Magn.*, vol. 36, no. 4, pp. 1600-1605, Jul. 2000.

[B10] J. P. Webb, and B. Forghani, "A single scalar potential method for 3D magnetostatics using edge elements," *IEEE Trans. Magn.*, vol. 25, no. 5, pp. 4126-4128, Sep. 1989.

[B11] J. P. Webb, and B. Forghani, "T-method using hierarchical edge elements," *IEE Proc. Sci. Meas. Technol.*, vol. 142, no. 2, pp. 133-141, Mar. 1995.

[B12] A. G. Kladas, and J. A. Tegopoulos, "A new scalar potential formulation for 3-D magnetostatics necessitating no source field calculation," *IEEE Trans. Magn.*, vol. 28, no. 2, pp. 1103-1106, Mar. 1992.

[B13] H. T. Luong, Y. Marechal, and G. Meunier, "Computation of 3-D current driven eddy current problems using cutting surfaces," *IEEE Trans. Magn.*, vol. 33, no. 2, pp. 1314-1317, Mar. 1997.

- [B14] A. T. Phung, O. Chadebec, P. Labie, Y. L. Floch, and G. Meunier, "Automatic cuts for magnetic scalar potential formulations," *IEEE Trans. Magn.*, vol. 41, no. 5, pp. 1668-1671, May 2005.
- [B15] Z. Ren, "T-formulation for eddy-current problems in multiply connected regions," *IEEE Trans. Magn.*, vol. 38, no. 2, pp. 557-560, Mar. 2002.
- [B16] P. Zhou, Z. Badics, D. Lin, and Z. J. Cendes, "Nonlinear T-formulation including motion for multiply connected 3-D problems," *IEEE Trans. Magn.*, vol. 44, no. 6, pp. 718-721, Jun. 2008.
- [B17] B.E. MacNeal, J.R. Brauer, R.N. Coppelino, "A general finite element vector potential formulation of electromagnetics using a time-integrated electric scalar potential," *IEEE Trans. Magn.*, vol. 26, pp. 1768 – 1770, 1990.
- [B18] T. Morisue, "A new formulation of the magnetic vector potential method in 3-D multiply connected regions," *IEEE Trans. Magn.*, vol. 24, pp. 110-113, Jan. 1988.
- [B19] Oszkar Biro, and Kurt Preis, "On the use of the magnetic vector potential in the finite element analysis of three-dimensional eddy currents," *IEEE Trans. Magn.*, vol. 25, no. 4, pp. 3145-3159, July 1989.
- [B20] R. Bossavit, "How weak is the "weak solution" in finite element methods?" *IEEE Trans. Magn.*, vol. 34, no. 5, pp. 2429-2432, Sep 1998.
- [B21] J. M. Jin, *The finite element method in electromagnetics*, 2 nd ed. Hoboken, NJ: Wiley, 2002.
- [B22] Y. P. Zhao and W. N. Fu, "A Novel Formulation with Coulomb Gauge for 3-D Magnetostatic Problems Using Edge Elements," *IEEE Trans. Magn.*, vol. 53, no. 6, Jun 2017.
- [B23] Y. P. Zhao and W. N. Fu, "A Novel Formulation with Coulomb Gauge for 3-D Magnetostatic Problems Using Edge Elements," *IEEE Trans. Magn.*, vol. 53, no. 6, Jun 2017.
- [B24] 'Axial Field of a Finite Solenoid', <https://tiggerntatie.github.io/emagnet/solenoids/solenoidonaxis.htm>.
- [B25] P. H. Mellor, D. Roberts, and D. R. Turner, "Lumped Parameter Thermal-Model for Electrical Machines of Tefc Design," *IEE Proc. Elec. Power Appl.*, vol. 138, no. 5,

pp. 205-218, Sep 1991.

[B26] W. Minkowycz, E. M. Sparrow, G. Schneider, and R. Pletcher, "*Handbook of numerical heat transfer*," New York, Wiley-Interscience, 1988.

[B27] A. Boglietti, et al., "Evolution and modern approaches for thermal analysis of electrical machines," *IEEE Trans. Ind. Electron.*, vol. 56, no. 3, pp. 871-882, Mar. 2009.

[B28] F. T. P. Picher, M. Chaaban, S. Gravel, C. Rajotte, B. Girard, "Optimisation of transformer overload using advanced thermal modeling," in *The CIGRE Conference*, Paris, France, 2010.

[B29] L. W. Pierce and W. J. McNutt, "An Investigation of the Thermal Performance of an Oil Filled Transformer Winding," *IEEE Trans. Power Del.*, vol. 7, no. 3, pp. 1347-1358, Jul. 1992.

[B30] J. Smolka, O. Biro, and A. J. Nowak, "Numerical Simulation and Experimental Validation of Coupled Flow, Heat Transfer and Electromagnetic Problems in Electrical Transformers," *Arch. Comput. Method E.*, vol. 16, no. 3, pp. 319-355, Sep 2009.

[B31] Magnet & Thermnet, version 7.5, Montreal: Infolytica, May 6, 2014.

[B32] JMAG, version 18.0, Japan: JMAG, Feb. 2019.

[B33] ANSYS, version 18.2, Pittsburgh: ANSYS, Aug. 2017.

[B34] COMSOL Multiphysics, version 5.4, Stockholm: COMSOL, Oct. 2018.

[B35] Y. J. Zhang, W. N. Qin, and J. J. Ruan, "Variable mapping method with nonmatching meshes in 3-d finite-element analysis of coupled electromagnetic-structural fields," *IEEE Trans. Plasma Sci.*, vol. 43, no. 5, pp. 1288-1292, May 2015.

[B36] 刘刚, 张瀚方, 池骋, 李琳, and 李慧奇, "二维电磁场-流体-温度场耦合仿真节点数据映射算法研究," *电工技术学报*, vol. 33, no. 1, pp. 148-157, 2018.

[B37] P. S. Georgilakis, *Spotlight on modern transformer design*. Springer Science & Business Media, 2009.

- [B38] J. Smolka, "CFD-based 3-D optimization of the mutual coil configuration for the effective cooling of an electrical transformer," *Appl. Therm. Eng.*, vol. 50, no. 1, pp. 124-133, Jan 10 2013.
- [B39] J. Smolka and A. J. Nowak, "Shape Optimization of Coils and Cooling Ducts in Dry-Type Transformers Using Computational Fluid Dynamics and Genetic Algorithm," *IEEE Trans. Magn.*, vol. 47, no. 6, pp. 1726-1731, Jun 2011.
- [B40] L. Susnjic, Z. Haznadar, and Z. Valkovic, "3D finite-element determination of stray losses in power transformer," *Electric Power Systems Research*, vol. 78, no. 10, pp. 1814-1818, 2008.
- [B41] D. Constantin, P.-M. Nicolae, and C.-M. Nitu, "3D Finite element analysis of a three phase power transformer," in **Eurocon 2013**, 2013, pp. 1548-1552: IEEE.
- [B42] M. Tsili, A. KLADAS, P. GEORGILAKIS, A. SOUFLARIS, and D. PAPARIGAS, "3D Finite Element and Mixed Finite-Boundary Element Method for the Magnetic Field Analysis of Power Transformers," *Wseas Transactions ON Circuits and Systems*, no. 5.
- [B43] E. I. Amoiralis, M. A. Tsili, P. S. Georgilakis, A. G. Kladas, and A. T. Souflaris, "A parallel mixed integer programming-finite element method technique for global design optimization of power transformers," *IEEE Transactions on Magnetics*, vol. 44, no. 6, pp. 1022-1025, 2008.
- [B44] Shenyang Transformer LLC. *Design handbook of oil-immersed power transformer*. Shenyang: Shenyang Transformer LLC, pp. 162-203, 1999.
- [B45] C. W. Group, "*Transformer Thermal Modelling*," CIGRE report, 2016.
- [B46] J. H. Zhang and X. G. Li, "Oil cooling for disk-type transformer windings - Part 1: Theory and model development," *IEEE Trans. Power Del.*, vol. 21, no. 3, pp. 1318-1325, Jul. 2006.
- [B47] J. H. Zhang and X. G. Li, "Oil cooling for disk-type transformer windings - Part II: Parametric studies of design parameters," *IEEE Trans. Power Del.*, vol. 21, no. 3, pp. 1326-1332, Jul. 2006.

- [B48] F. Torriano, M. Chaaban, and P. Picher, "Numerical study of parameters affecting the temperature distribution in a disc-type transformer winding," *Appl. Therm. Eng.*, vol. 30, no. 14-15, pp. 2034-2044, Oct. 2010.
- [B49] F. Torriano, P. Picher, and M. Chaaban, "Numerical investigation of 3D flow and thermal effects in a disc-type transformer winding," *Appl. Therm. Eng.*, vol. 40, pp. 121-131, Jul. 2012.
- [B50] A. Skillen, A. Revell, H. Iacovides, and W. Wu, "Numerical prediction of local hot-spot phenomena in transformer windings," *Appl. Therm. Eng.*, vol. 36, pp. 96-105, Apr. 2012.
- [B51] N. El Wakil, N. C. Chereches, and J. Padet, "Numerical study of heat transfer and fluid flow in a power transformer," *Int. J. Therm. Sci.*, vol. 45, no. 6, pp. 615-626, Jun. 2006.
- [B52] X. Zhang, Z. D. Wang, and Q. Liu, "Prediction of Pressure Drop and Flow Distribution in Disc-Type Transformer Windings in an OD Cooling Mode," *IEEE Trans. Power Del.*, vol. 32, no. 4, pp. 1655-1664, Aug. 2017.
- [B53] S. Tenbohlen, N. Schmidt, C. Breuer, S. Khandan, and R. Lebreton, "Investigation of Thermal Behavior of an Oil-Directed Cooled Transformer Winding," *IEEE Trans. Power Del.*, vol. 33, no. 3, pp. 1091-1098, Jun. 2018.
- [B54] G. R. Rodriguez, L. Garelli, M. Storti, D. Granata, M. Amadei, and M. Rossetti, "Numerical and experimental thermo-fluid dynamic analysis of a power transformer working in ONAN mode," *Appl. Therm. Eng.*, vol. 112, pp. 1271-1280, Feb 5 2017.
- [B55] L. Garelli, G. R. Rodriguez, M. Storti, D. Granata, M. Amadei, and M. Rossetti, "Reduced model for the thermo-fluid dynamic analysis of a power transformer radiator working in ONAF mode," *Appl. Therm. Eng.*, vol. 124, pp. 855-864, Sep 2017.
- [B56] L. D. Coelho, V. C. Mariani, M. V. F. da Luz, and J. V. Leite, "Novel Gamma Differential Evolution Approach for Multiobjective Transformer Design Optimization," *IEEE Trans. Magn.*, vol. 49, no. 5, pp. 2121-2124, May 2013.
- [B57] H. V. H. Ayala, L. D. Coelho, V. C. Mariani, M. V. F. da Luz, and J. V. Leite, "Harmony Search Approach Based on Ricker Map for Multi-Objective Transformer Design Optimization," *IEEE Trans. Magn.*, vol. 51, no. 3, Mar 2015.

- [B58] L. D. Coelho, V. C. Mariani, F. A. Guerra, M. V. F. da Luz, and J. V. Leite, "Multiobjective Optimization of Transformer Design Using a Chaotic Evolutionary Approach," *IEEE Trans. Magn.*, vol. 50, no. 2, Feb 2014.
- [B59] H. V. H. Ayala, E. H. D. Segundo, L. Lebensztajn, V. C. Mariani, and L. D. Coelho, "Multiobjective Wind Driven Optimization Approach Applied to Transformer Design," *2016 IEEE Congress on Evolutionary Computation*, pp. 4642-4647, 2016.
- [B60] P. S. Georgilakis, M. A. Tsili, and A. T. Souflaris, "A heuristic solution to the transformer manufacturing cost optimization problem," *J. Mater. Process. Tech.*, vol. 181, no. 1-3, pp. 260-266, Jan. 2007.
- [B61] S. Anishek, R. Sony, K. J. Jayadeep, and P. M. Kamath, "Performance Analysis and Optimisation of an Oil Natural Air Natural Power Transformer Radiator," *International Conference on Emerging Trends in Engineering, Science and Technology*, vol. 24, pp. 428-435, 2016.
- [B62] R. M. Radwan, R. M. Eldewieny, and I. A. Metwally, "Investigation of Static Electrification Phenomenon Due to Transformer Oil Flow in Electric-Power Apparatus," *IEEE Trans. Electr. Insul.*, vol. 27, no. 2, pp. 278-286, Apr. 1992.
- [B63] S. Choi and J. Eastman, "Enhancing thermal conductivity of fluids with nanoparticles," *ASME-Publications-Fed*, vol. 231, pp. 99-106, 1995.
- [B64] A. A. A. Arani and J. Amani, "Experimental study on the effect of TiO<sub>2</sub>-water nanofluid on heat transfer and pressure drop," *Exp. Therm. Fluid Sci.*, vol. 42, pp. 107-115, Oct 2012.
- [B65] C. T. Nguyen, G. Roy, C. Gauthier, and N. Galanis, "Heat transfer enhancement using Al<sub>2</sub>O<sub>3</sub>-water nanofluid for an electronic liquid cooling system," *Appl. Therm. Eng.*, vol. 27, no. 8-9, pp. 1501-1506, 2007.
- [B66] M. Maharana, M. M. Bordeori, S. K. Nayak, and N. Sahoo, "Nanofluid-based transformer oil: effect of ageing on thermal, electrical and physicochemical properties," *IET Sci. Meas. Technol.*, vol. 12, no. 7, pp. 878-885, 2018.
- [B67] D. Ashtiani, M. A. Akhavan-Behabadi, and M. F. Pakdaman, "An experimental investigation on heat transfer characteristics of multi-walled CNT-heat transfer oil nanofluid flow inside flattened tubes under uniform wall temperature condition," *Int.*

*Commun. Heat Mass*, vol. 39, no. 9, pp. 1404-1409, 2012.

[B68] J. Li, Z. T. Zhang, P. Zou, S. Grzybowski, and M. Zahn, "Preparation of a Vegetable Oil-Based Nanofluid and Investigation of Its Breakdown and Dielectric Properties," *IEEE Electr. Insul. M.*, vol. 28, no. 5, pp. 43-50, Sep-Oct 2012.

[B69] Z. Haddad, C. Abid, H. F. Oztop, and A. Mataoui, "A review on how the researchers prepare their nanofluids," *Int. J. Therm. Sci.*, vol. 76, pp. 168-189, Feb 2014.

[B70] C. Choi, H. S. Yoo, and J. M. Oh, "Preparation and heat transfer properties of nanoparticle-in-transformer oil dispersions as advanced energy-efficient coolants," *Curr. Appl. Phys.*, vol. 8, no. 6, pp. 710-712, Oct. 2008.

[B71] A. Beheshti, M. Shanbedi, and S. Z. Heris, "Heat transfer and rheological properties of transformer oil-oxidized MWCNT nanofluid," *J. Therm. Anal. Calorim.*, vol. 118, no. 3, pp. 1451-1460, Dec 2014.

[B72] S. C. Pugazhendhi, "Experimental evaluation on dielectric and thermal characteristics of nano filler added transformer oil," in *Proc. ICHVE*, Shanghai, China, 2012, pp. 207-210.

[B73] M. Rafiq, Y. Z. Lv, and C. R. Li, "A Review on Properties, Opportunities, and Challenges of Transformer Oil-Based Nanofluids," *J. Nanomater.*, 2016.

[B74] Z. Haddad, H. F. Oztop, E. Abu-Nada, and A. Mataoui, "A review on natural convective heat transfer of nanofluids," *Renew. Sust. Energ. Rev.*, vol. 16, no. 7, pp. 5363-5378, Sep 2012.

[B75] S. M. Vanaki, R. Ganesan, and H. A. Mohammed, "Numerical study of convective heat transfer of nanofluids: A review," *Renew. Sust. Energ. Rev.*, vol. 54, pp. 1212-1239, Feb 2016.

[B76] P. Xiaofei, "Study of Nanofluids Heat Transfer Performance in High Temperature Condition based on Vehicular Cooler," Ph.D. thesis, Dept. Elect. Eng., Zhejiang University, Zhejiang, China, 2007.

[B77] M. Corcione, "Empirical correlating equations for predicting the effective thermal conductivity and dynamic viscosity of nanofluids," *Energy Convers. Manage.*, vol. 52, no. 1, pp. 789-793, Jan. 2011.

- [B78] F. Talebi, A. H. Mahmoudi, and M. Shahi, "Numerical study of mixed convection flows in a square lid-driven cavity utilizing nanofluid," *Int. Commun. Heat Mass*, vol. 37, no. 1, pp. 79-90, Jan 2010.
- [B79] M. Kalteh, A. Abbassi, M. Saffar-Avval, A. Frijns, A. Darhuber, and J. Harting, "Experimental and numerical investigation of nanofluid forced convection inside a wide microchannel heat sink," *Appl. Therm. Eng.*, vol. 36, pp. 260-268, Apr 2012.
- [B80] M. Kalteh, A. Abbassi, M. Saffar-Avval, and J. Harting, "Eulerian-Eulerian two-phase numerical simulation of nanofluid laminar forced convection in a microchannel," *Int. J. Heat Fluid Fl.*, vol. 32, no. 1, pp. 107-116, Feb 2011.
- [B81] V. Bianco, O. Manca, and S. Nardini, "Numerical investigation on nanofluids turbulent convection heat transfer inside a circular tube," *Int. J. Therm. Sci.*, vol. 50, no. 3, pp. 341-349, Mar 2011.
- [B82] M. H. Fard, M. N. Esfahany, and M. R. Talaie, "Numerical study of convective heat transfer of nanofluids in a circular tube two-phase model versus single-phase model," *Int. J. Heat Mass Transf.*, vol. 37, no. 1, pp. 91-97, Jan. 2010.
- [B83] R. Lotfi, Y. Saboohi, and A. M. Rashidi, "Numerical study of forced convective heat transfer of Nanofluids: Comparison of different approaches," *Int. J. Heat Mass Transf.*, vol. 37, no. 1, pp. 74-78, Jan. 2010.
- [B84] W. Rashmi, A. F. Ismail, M. Khalid, and Y. Faridah, "CFD studies on natural convection heat transfer of Al<sub>2</sub>O<sub>3</sub>-water nanofluids," *Heat Mass Transfer.*, vol. 47, no. 10, pp. 1301-1310, Oct. 2011.
- [B85] H. F. Oztop and E. Abu-Nada, "Numerical study of natural convection in partially heated rectangular enclosures filled with nanofluids," *Int. J. Heat Fluid Flow*, vol. 29, no. 5, pp. 1326-1336, Oct. 2008.
- [B86] R. Pendyala, S. U. Ilyas, L. R. Lim, and N. Marneni, "CFD Analysis of Heat Transfer Performance of Nanofluids in Distributor Transformer," *Proceeding of 4th International Conference on Process Engineering and Advanced Materials*, vol. 148, pp. 1162-1169, 2016.
- [B87] W. M. Guan et al., "Finite Element Modeling of Heat Transfer in a Nanofluid Filled Transformer," *IEEE Trans. Magn.*, vol. 50, no. 2, Feb 2014.

- [B88] G. Mishra et al., "Magnetic properties of nanocrystalline  $\beta$ -SiC," *Journal of nanoscience and nanotechnology*, vol. 11, no. 6, pp. 5049-5053, 2011.
- [B89] A. M. Morega, M. Morega, L. Pislaru-Danescu, V. Stoica, F. Nouras, and F. D. Stoian, "A Novel, Ferrofluid-Cooled Transformer. Electromagnetic Field and Heat Transfer by Numerical Simulation," *Proceedings of the 12th International Conference on Optimization of Electrical and Electronic Equipment*, Pts I-IV, pp. 140, 2010.
- [B90] L. Pislaru-Danescu et al., "Prototyping a Ferrofluid-Cooled Transformer," (in English), *IEEE Transactions on Industry Applications*, vol. 49, no. 3, pp. 1289-1298, May-Jun 2013.
- [B91] R. Zanella et al., "Study of Magnetoconvection Impact on a Coil Cooling by Ferrofluid with a Spectral/Finite-Element Method," *IEEE Trans. Magn.*, vol. 54, no. 3, pp. 1-4, 2018.
- [B92] S. Engelmann, A. Nethe, T. Scholz, and H. D. Stahlmann, "Experiments with a ferrofluid - supported linear electric motor," *Applied organometallic chemistry*, vol. 18, no. 10, pp. 529-531, 2004.
- [B93] A. Methe, T. Scholz, H. D. Stahlmann, and M. Filtz, "Ferrofluids in electric motors - A numerical process model," *IEEE Trans. Magn.*, vol. 38, no. 2, pp. 1177-1180, Mar 2002.

# Chapter 3 The Adaptive Degrees-of-Freedom Finite Element Method

Adaptive FEMs were proposed to solve real-life electromagnetic problems by automatically modify the discretization of specific problems [C1], and the major aim of adaptive FEMs is to derive accurate solutions while avoiding the unnecessary waste of computational resources. In this chapter, an adaptive DoFs FEM is presented for the 3D nonlinear magnetic field, thermal field, and coupled magneto-thermal field analysis.

## 3.1 Introduction to Adaptive Finite Element Method

With the given criterion on precision, an optimal discretization file is generated for the problem during the adaptive calculation, and this discretization file should be as coarse as possible while satisfying the criterion [C2]. For transient problems, the optimal discretization file may vary for different time steps, and automatic control of time step sizes should be included in the solver as well. Generally, there are two key techniques, namely, error estimators and discretization adjustment, involved in the adaptive FEMs [C1]. Based on the estimated errors of current solution, the discretization file is automatically refined or coarsened, and the modified discretization file is used in the following step or time step.

According to the discretization adjustment method, the adaptive FEMs are divided into three categories, namely, the  $r$ -method [C3, C4],  $p$ -method [C5] and  $h$ -method [C1, C6, C7]. In the  $r$ -method, the mesh topology is maintained during the modification, and nodes are concentrated to these areas with large errors to enhance the resolution. This method is not flexible in some situations, especially for these problems with coarse meshes. In the  $p$ -method, the order of the polynomial basis

functions is changed adaptively, while the mesh is maintained to be unchanged. Since several different local stiffness matrixes are involved, the implementation of this method is relatively complicated. Hence, the  $r$ -method and the  $p$ -method are also used in combination with the  $h$ -method. As the most commonly used adaptive FEM, the  $h$ -method changes the mesh successively by adding and removing nodes.

With the ability to handle complicated geometries, triangle and tetrahedron are two common elements that are used to discretise the magnetic field. Recursive refinement algorithms were proposed to refine the mesh of triangle and tetrahedron element, such as the longest edge bisection algorithm [C8] for triangle and the recursive algorithm proposed by Kossaczky [C9] for 3-D problems. No hanging point and other type of element are generated in the refinement process. In addition, the unicity of element can be maintained during the coarsening process. The mesh information, such as the finite element information, geometric data, and DoFs information, needs to be reorganized after the refinement and coarsening [C2].

The adaptive control of procedures in space and time step sizes is generally included in the adaptive FEMs for transient problems. Several strategies are presented to realize the adaptive procedures in space [C10], namely, explicit strategy, semi-implicit strategy, implicit strategy A and implicit strategy B. Meanwhile, the algorithms for controlling time step sizes vary in the usage of grid adaption. Hence, these two controls can be combined in several ways [C2].

The discretization modification and the control of adaptive procedures are guided by the estimated errors of the current solution. Since the exact results of most of the DoFs are unknown, many researchers aim to propose an accurate, effective, and broadly suitable error estimator, such as the recovery-type [C11-C13], the residual type [C14], the energy based method [C15], the norm of the gradient of the solution [C1], the magnetic flux line method [C16] and so on.

The broadly used recovery type error estimator, the ZZ error estimator [C11] is simple and easy to implement. The exact value of flux density is assumed to be the interpolation of numerical solution [C17],

$$\mathbf{B}_{true}^e = \sum_{i=1}^{nv} N^{ie} \left( \frac{1}{M^i} \sum_1^{M^i} \mathbf{B}^j \right) \quad (3-1)$$

where;  $\mathbf{B}^j$  is the current flux density in element  $j$ ;  $\mathbf{B}_{true}^e$  is the exact value of  $\mathbf{B}^e$ ;  $nv$  is the number of vertexes; and  $N^i$  is the complement function for element  $e$ ;  $M^i$  is the number of elements consisting node  $i$ . Here, the flux density at a node is interpolated by the average flux density of its surrounding elements. For the node on the interface between materials, these  $M^i$  elements are divided according to material and then are used to estimate the nodal average flux density for each material. The errors of the current numerical solution are then calculated based on the magnetic energy as

$$(\varepsilon^e)^2 = \frac{\frac{1}{2} \int_{V_e} (\mathbf{B}^e - \mathbf{B}_{true}^e) \cdot \vartheta (\mathbf{B}^e - \mathbf{B}_{true}^e) dV}{\frac{1}{2NE} \sum_{i=1}^{NE} \int_{V_i} \mathbf{B}^i \cdot \vartheta \mathbf{B}^i dV} \times 100\% \quad (3-2)$$

where  $NE$  is the number of elements.

## 3.2 The Adaptive DoFs FEM for 3D Nonlinear Magnetic Field Analysis

During the calculation of nonlinear problems, the iteration process may generate some local refinement, which is not required for the following steps [C2]. To control the computational scale, local mesh coarsening may be needed. Hence, both mesh coarsening and mesh refinement may be involved in one single step, which increases the complexity in reorganizing the mesh information. Recently, a novel  $h$ -method, namely, the adaptive DoFs FEM, was proposed to solve 2D magnetic field [C18, C19]. The explicit nodes elimination, which is used in conventional  $h$ -method, is replaced by implicitly removing these redundant DoFs (slave DoFs) from the unknown list, which distinguishes this method from other  $h$ -methods. The slave-master technique is

introduced into this process to impose extra constraints on these slave DoFs, and these constraint formulations are formulated with master DoFs [C20]. After the transformation, the problem scale is reduced without actually coarsening the mesh. In addition, the subsequent information administration after mesh coarsening are obviated. A common refinement algorithm for triangle element, namely the longest edge bisection algorithm, is used in the refinement process. The proposed method is developed in combination with a simple constraint formulation, and its effectiveness has been validated by solving several 2D nonlinear problems.

To extend this method to solve 3D problems, a novel category of constraint, which has higher precision, is presented. The coefficients of the constraint formulation are derived with a uniform interpolation function for polyhedrons [C21]. More master DoFs are used in the proposed constraint to deal with the complex field. The improvement in accuracy is showcased by individual and overall assessment. Tetrahedral element is used in the spatial discretization, and the coarse mesh is refined with a bisection based algorithm. In addition, the nonlinearity introduced by materials are handled with the NR method, and the ZZ error estimator is used to calculate the errors of the numerical results.

### **3.2.1 The Proposed Constraint**

Nodes of minimal errors are removed in conventional  $h$ -methods, and the adapted mesh according to the current solution is used in the subsequent step. Although the DoFs at these nodes do not exist any longer, the potentials at these positions can be computed with the adjacent DoFs and the shape function of these related elements. Moreover, the accuracy of the solution, which is derived with the adapted mesh, is still acceptable. In the adaptive DoFs FEM, these redundant DoFs are interpolated with the adjacent DoFs reasonably and then removed from the unknown list implicitly. The DoFs are divided into three categories, slave DoFs, master DoFs, and normal DoFs. To differentiate these three types of DoFs, an identifier *dofId* is introduced into the

data structure, and the slave, master, and normal DoF are identified by 1, 2, and 0, respectively.

The extra interpolation functions of slave DoFs are formulated with master DoFs. A uniform linear interpolation function is given by

$$u^s = \sum_{i=1}^k \alpha_i u_i^m \quad (3-3)$$

where; the superscript ( $s$  and  $m$ ) is the attribute of DoF; the subscript is the index of master DoF;  $\alpha_i$  is the coefficient of the  $i^{th}$  master DoF;  $k$  is the number of master DoFs. These interpolation equations are then substituted into the algebraic system to remove the slave DoFs from the unknown list, which is the so-called slave-master technique. The extra interpolation formulations are also called constraints, which are imposed on the slave DoFs.

There are two key factors involved in the constraint, the choice of master DoFs and the determination of coefficients. The simple constraint, which is validated to be effective in 2D problems, adopts two adjacent master DoFs and average coefficients,

$$u^s = \frac{u_1^m + u_2^m}{2} \quad (3-4)$$

However, this constraint is unable to deal with the complicated 3D magnetic field. To extend the adaptive DoFs FEM to solve 3D problems, a novel constraint adopting more master DoFs with rational coefficients is presented.

For a slave node, the neighboring nodes, which are connected to the slave node by edges, are the first choice for master nodes. The number of neighboring nodes of slave nodes is different from each other, and the number of master nodes used for each slave node also varies. Then a general strategy is required to deal with the variation in the number of master nodes. In order to derive an accurate interpolation function for the slave DoF, a general shape function of polyhedrons [C21] is adopted, and the shape function is calculated by normalizing the weighting functions of nodes,

$$\alpha_i(\mathbf{x}) = \frac{w_i(\mathbf{x})}{\sum_{m=1}^{Nv} w_m(\mathbf{x})} \quad (3-5)$$

where;  $Nv$  is the number of master nodes;  $\mathbf{x}$  is the coordinate vector of the slave node;  $w_i(\mathbf{x})$  is the weighting function of the  $i^{th}$  master node, which is defined as,

$$w_i(\mathbf{x}) = \sum_{j=1}^l \left[ \frac{\gamma_{j,j+1}}{V_{i,j,j+1}} + \frac{\gamma_{i,j} V_{j-1,j+1,j}}{V_{i,j-1,j} V_{i,j,j+1}} \right] \quad (3-6)$$

where;  $j$  and  $l$  are the respective index of and the number of the neighboring master node for the  $i^{th}$  master node;  $V$  is the volume of the tetrahedron consisting of the slave node and other three nodes indexed by its subscripts; and the coefficient  $\gamma$  is given by

$$\gamma_{a,b} = \frac{\|(\mathbf{x}_a - \mathbf{x}) \times (\mathbf{x}_b - \mathbf{x})\|}{6} \arccos \left[ \frac{(\mathbf{x}_a - \mathbf{x})^T (\mathbf{x}_b - \mathbf{x})}{\|\mathbf{x}_a - \mathbf{x}\| \|\mathbf{x}_b - \mathbf{x}\|} \right] \quad (3-7)$$

Table 3.1. Neighboring information for the master nodes.

Master node $Id$	Sequenced neighboring master nodes
6252	11618 4590 5275 10687 11219 9438
4590	11618 6252 5275 8533
5275	10687 6252 4590 8533 4143 10078
8533	4143 5275 4590 11618 10617 11997
4143	10078 5275 8533 11997
5315	10617 6013 9438 11618
6013	10617 5315 9438 11219 5314 10078 11997
9438	11618 5315 6013 11219 6252
10687	10078 5275 6252 11219 5314
10078	11997 4143 5275 10687 5314 6013
5314	6013 10078 10687 11219
11219	6252 10687 5314 6013 9438
10617	8533 11618 5315 6013 11997
11618	8533 10617 5315 9438 6252 4590
11997	8533 4143 10078 6013 10617

The index of neighboring master node is numbered independently for each master node, and the weighting function is computed according to the neighboring information. This strategy applies to any polyhedron with no less than four faces.

Table 3.2. The MVP at master nodes and the constraint coefficients.

$Id$	$A_x$	$A_y$	$A_z$	$\alpha$
6252	-6.81E-05	-5.44E-05	2.47E-06	0.05780
4590	-8.52E-05	-4.99E-05	2.67E-06	0.05469
5275	-7.44E-05	-6.52E-05	1.94E-06	0.05504
8533	-8.35E-05	-5.26E-05	2.04E-06	0.07081
4143	-7.73E-05	-6.50E-05	1.30E-06	0.06132
5315	-7.04E-05	-3.56E-05	1.39E-06	0.05946
6013	-6.33E-05	-4.54E-05	1.12E-06	0.08440
9438	-6.78E-05	-4.13E-05	2.34E-06	0.05863
10687	-6.01E-05	-6.36E-05	1.59E-06	0.05512
10078	-6.82E-05	-6.13E-05	1.14E-06	0.09634
5314	-5.60E-05	-5.71E-05	9.65E-07	0.05777
11219	-5.98E-05	-5.29E-05	1.73E-06	0.07132
10617	-7.73E-05	-4.12E-05	1.35E-06	0.06856
11618	-7.80E-05	-4.41E-05	2.27E-06	0.08910
11997	-7.45E-05	-5.05E-05	8.90E-07	0.05965

A slave node with  $Id$  1311 is chosen from the second numerical example in section 3.2.3 to illustrate the constraint details. 15 adjacent nodes are adopted as the master nodes for this slave node, and the neighboring information among these master nodes are administrated and sorted, as listed in Table 3.1. The dummy polyhedron formed by these master nodes have 26 triangular faces. Based on the neighboring information, the constraint coefficients are obtained by normalizing the calculated weighting functions. The derived coefficients are listed in Table 3.2 with the solution

of the DoFs at these nodes. The approximation results of the proposed constraint and the simple constraint are compared, as listed in Table 3.3. Two subscripts,  $c1$  and  $c2$ , are used to identify the proposed constraint and the simple constraint, respectively. An error analysis is conducted with the FE solution of the slave DoFs as the references. It is found that the performance of the simple constraint is unpredictable, and there are huge discrepancies among the errors of three directions. In contrast, a robust performance is observed when using the proposed constraint, although there is not any pre-knowledge of the field. The analysis of more slave DoFs reflects the same conclusion, and the overall performance in numerical problems is analyzed in the section 3.2.3.

Table 3.3. Error analysis of these two constraints.

$A$	$V_{ref}$	$V_{c1}$	$V_{c2}$	$E_{c1}$	$E_{c2}$
$A_x$	-7.13E-05	-7.09E-05	-7.66E-05	0.5%	7.5%
$A_y$	-5.27E-05	-5.18E-05	-5.22E-05	1.8%	1.1%
$A_z$	1.71E-06	1.66E-06	2.57E-06	2.7%	50.6%

### 3.2.2 Adaptive DoFs Adjustment

The number of DoFs is increased along with the mesh refinement process, in which new nodes are added in regions with steep gradients. During the generation of new nodes, edges, faces and elements, the indexes, relations, and neighboring information are changed, which needs to be reorganized. The recursive refinement algorithm proposed for tetrahedron element is adopted in this study to increase the DoFs [C9]. The six edges in a tetrahedron element is separated into three “edges”, two “face diagonals”, and one “diagonal”. As shown in Fig. 3.1, the recursive refinement is a process to bisect the diagonal-face diagonal-edge in turn. Accordingly, the elements are divided into three categories to facilitate the refinement. Preconditioning may be required to ensure the edge to be bisected is compatibly divisible, which means all the elements consisting of this edge are in one type.

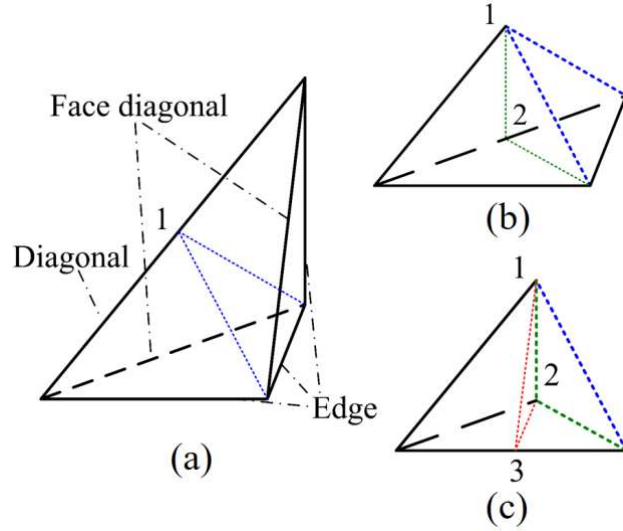


Fig. 3.1. The edge classification and the recursive refinement by bisecting (a) the diagonal, (b) one of the face diagonals and (c) one of the edges

The slave DoFs is removed by the slave-master technique in the element level, accompanied by an identical assembly process as the conventional FEM [C22]. During the elimination, the element algebraic equation is transformed with the constraints of slave DoFs. To illustrate this technique, the transformation process of the FE equation of a tetrahedron, in which the DoFs at the third node are assumed to be slaves, is given in detail. The element algebraic equation derived by discretizing the MVP is given by

$$\mathbf{K}\mathbf{u} = \mathbf{f} \quad (3-8)$$

where;  $\mathbf{K}$  is the element stiffness matrix (size  $12 \times 12$ );  $\mathbf{u}$  is the element unknown vector (size  $12 \times 1$ );  $\mathbf{f}$  is the element load vector (size  $12 \times 1$ ). Replace the slave DoFs in the unknown vector with the constraints,

$$\mathbf{u} = \begin{Bmatrix} \mathbf{A}_1 \\ \mathbf{A}_2 \\ \mathbf{A}_3 \\ \mathbf{A}_4 \end{Bmatrix} = \begin{Bmatrix} \mathbf{I}_3 & & & \\ & \mathbf{I}_3 & & \\ & & \boldsymbol{\alpha} & \\ & & & \mathbf{I}_3 \end{Bmatrix} \begin{Bmatrix} \mathbf{A}_1 \\ \mathbf{A}_2 \\ \mathbf{A}'_3 \\ \mathbf{A}_4 \end{Bmatrix} = \mathbf{T}\hat{\mathbf{u}} \quad (3-9)$$

where;  $\mathbf{I}_3$  a unit matrix (size 3);  $\boldsymbol{\alpha}$  is the constraint matrix (size  $3 \times 3k$ );  $\mathbf{A}'_3$  is the master unknown vector (size  $3k \times 1$ );  $\mathbf{T}$  is a compact notation for the transformation matrix (size  $12 \times (9 + 3k)$ );  $\hat{\mathbf{u}}$  is the transformed unknown vector (size  $(9 + 3k) \times 1$ ). After the substitution, the slave DoFs are eliminated from the

transformed unknown vector. The constraint matrix  $\alpha$  is given as follows,

$$\alpha = \begin{bmatrix} \alpha_1 & \dots & \alpha_k & & & & & & \\ & & & \alpha_1 & \dots & \alpha_k & & & \\ & & & & & & \alpha_1 & \dots & \alpha_k \end{bmatrix} \quad (3-10)$$

and the master unknown vector is given by

$$\mathbf{A}'_3 = [A_{1x}^m \quad \dots \quad A_{kx}^m \quad A_{1y}^m \quad \dots \quad A_{ky}^m \quad A_{1z}^m \quad \dots \quad A_{kz}^m]^T \quad (3-11)$$

Substituting equation (3-9) into the element algebraic equation (3-8) and pre-multiplying the newly generated equation with the transpose of  $\mathbf{T}$  gives

$$\mathbf{KT}\hat{\mathbf{u}} = \mathbf{f} \rightarrow \mathbf{T}^T \mathbf{KT}\hat{\mathbf{u}} = \mathbf{T}^T \mathbf{f} \rightarrow \hat{\mathbf{K}}\hat{\mathbf{u}} = \hat{\mathbf{f}} \quad (3-12)$$

where;  $\hat{\mathbf{K}}$  is the transformed element stiffness matrix (size  $(9 + 3k) \times (9 + 3k)$ );  $\hat{\mathbf{f}}$  is the transformed element load vector (size  $(9 + 3k) \times 1$ ). The transformation does not change the symmetry characteristic of the stiffness matrix. After the global assembly, the reduction of the algebraic system dimension is realized. These slave DoFs are recovered from their constraints after solving the algebraic equations.

Two types of adaptive procedures are adopted to solve the nonlinear problems in combination with the simple constraint and the proposed constraint. In the first strategy, the error estimator is only invoked after the first iteration. The adapted DoFs are then solved in the following steps until convergence. The other strategy uses the solve-estimate-adapt process until the given criterion is met.

### 3.2.3 Numerical Examples

In order to check the mesh refinement algorithm, an artificial static problem with analytical solutions are used,

$$\begin{cases} \nabla \times \left( \frac{1}{\mu} \nabla \times \mathbf{A} \right) - \nabla \vartheta \nabla \cdot \mathbf{A} = \mathbf{J}_s \\ \mu = 2.0 \\ \mathbf{J}_s = (-2, -2, -2) \\ \mathbf{A} = (y^2 + z^2, z^2 + x^2, x^2 + y^2) \end{cases} \quad (3 - 13)$$

The problem is defined within a unit cube, the surface of which are specified with Dirichlet boundary conditions. A coarse mesh is generated firstly and then refined successively, and the  $L^2$  error is used to estimate the solutions,

$$\|\varepsilon\|_{L_2} = \left( \int_V (u - u^h)^2 dV \right)^{\frac{1}{2}} \quad (3 - 14)$$

where;  $u$  and  $u^h$  are the numerical result and the exact value, respectively. This formula is incorporate to the FEM solver by the Gauss integral of second order precision. As listed in Table 3.4, the computed  $L^2$  errors for the magnetic potentials continuously decrease along the refinement process, which verifies the effectiveness of this refinement algorithm.

Table 3.4 The convergence test for mesh refinement algorithm.

No. of elements	$L^2$ error of $A_x$	$L^2$ error of $A_y$	$L^2$ error of $A_z$
642	1.47E-2	1.42E-3	1.48E-3
5004	4.02E-3	3.99E-3	4.13E-3
37632	2.13E-3	2.05E-3	1.99E-3

A nonlinear artificial problem [C23], which is defined within a unit cube, is used to showcase the correctness of the proposed constraint,

$$\begin{cases} \nabla \times (\vartheta \nabla \times \mathbf{A}) - \nabla \vartheta \nabla \cdot \mathbf{A} = \mathbf{J}_s \\ \vartheta = e^{x+y}/\sqrt{2} \\ \mathbf{J}_s = (0, 0, -2e^{2x+2y}) \end{cases} \quad (3 - 15)$$

The analytical solution of this problem is given by  $\mathbf{A} = (0, 0, e^{x+y}/\sqrt{2})$ , with which the Dirichlet boundary conditions are derived for the artificial numerical problem. The

nonlinear reluctivity is linearized by the NR method, and the criterion for convergence is a residual below  $1.0 \times 10^{-6}$ . In the generated mesh, there are 33074 nodes and 81567 DoFs.

These two adaptive procedures are tested in combination with the simple constraint and the proposed constraint, and the estimated  $L^2$  errors of the magnetic potentials are listed in Table 3.5. It is observed that the errors of the simple constraint are at least an order of magnitude larger than the proposed constraint. In addition, compared with the first adaptive strategy, the second adaptive procedure derives more accurate solution by a smaller number of DoFs.

Table 3.5 Error analysis of these two constraints in the second example

No. of DoFs	$L^2$ error of $A_x$	$L^2$ error of $A_y$	$L^2$ error of $A_z$
74394	1.55E-2	2.50E-2	3.61E-2
About 72522	8.20E-3	1.22E-2	2.77E-2
74394	1.03E-3	1.03E-3	2.11E-3
About 69354	1.59E-4	1.65E-4	3.75E-4

The second row and the third row list the results of the simple constraint, and the results of the proposed constraint are given in the last two rows.

The numerical problem in the section 2.1.6 is recalculated with the adaptive DoFs method. An algebraic system with 164574 unknowns are generated from the mesh with 55325 nodes. After 18480 DoFs are specified as slaves, the system is re-solved with the proposed constraint (constraint 2). The numerical solution of the magnetic flux density along the solenoid axis shows good consistency with the analytical solution [C24] (see Fig. 3.2), which validates the correctness of the proposed constraint. The simple constraint (constraint 1) is also considered for comparison, and the derived solution, which is drawn in black color, reveals that large errors are introduced into the solution by this constraint.

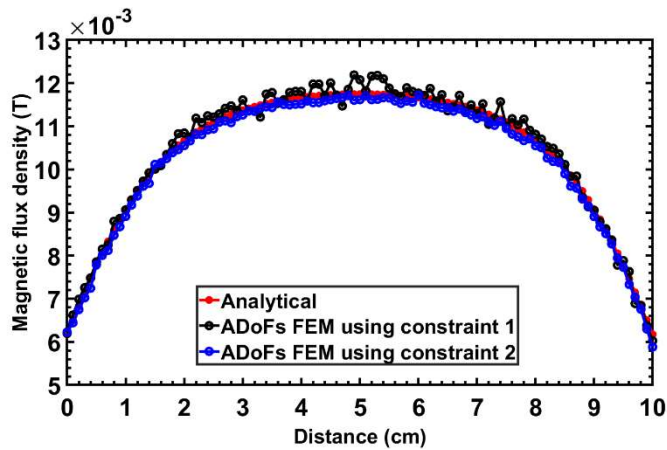


Fig. 3.2. The magnetic flux density along the axis of the air core.

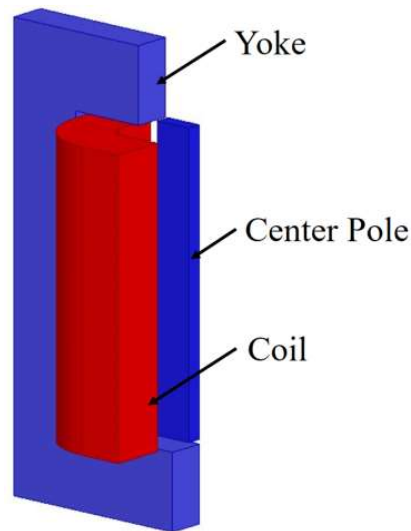


Fig. 3.3. The geometry of TEAM problem 20.

To check the performance in nonlinear engineering problems, the TEAM workshop problem 20 [C25] is solved using this adaptive DoFs FEM. Owing to the symmetry structure, one quarter of the geometry is modelled (see Fig. 3.3) and solved. The yoke and the center pole are made of a material with nonlinear magnetic reluctivity. An exciting current of 5000 ampere-turns is flowing in the coil. For the nonlinear iteration, the convergence criterion predefined on the residual is below  $1.0 \times 10^{-6}$ . The second adaptive procedure is adopted, and about 12253 DoFs are chosen from the total 129287 DoFs and then specified as solve DoFs in each adaption. Hence, during the iteration, the scale of the problem is roughly reduced by 15%. The virtual work method [C26] is used to calculate the magnetic force, and the force acting on the center

pole in the  $z$  direction is 19.55N. For a full scale geometry, the calculate force would be 78.2N, which is close to the measured value [C27]. In addition, the calculated magnetic flux density and magnetic vector potential are given in Fig. 3.4 for illustration. This method is easily implemented and also applicable to solving other fields and transient problems.

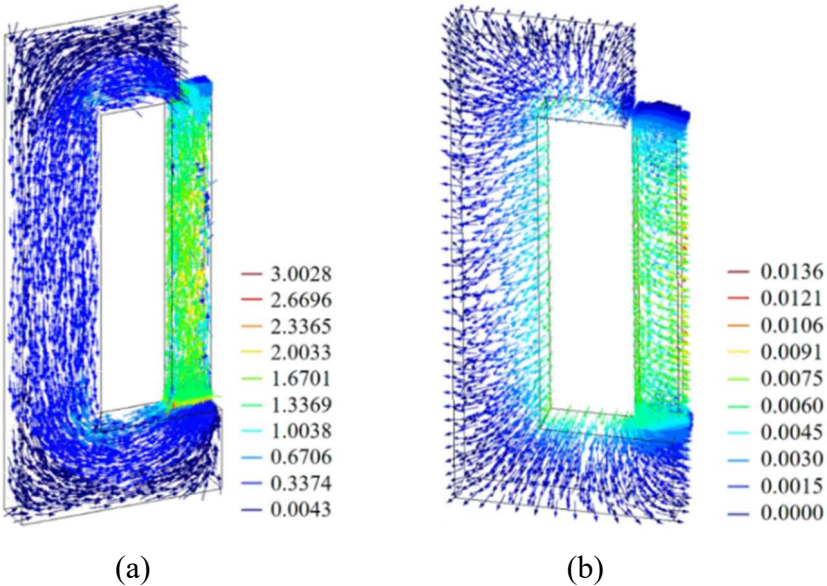


Fig. 3.4. (a) The magnetic flux density and (b) the vector potential derived with the adaptive DoFs FEM.

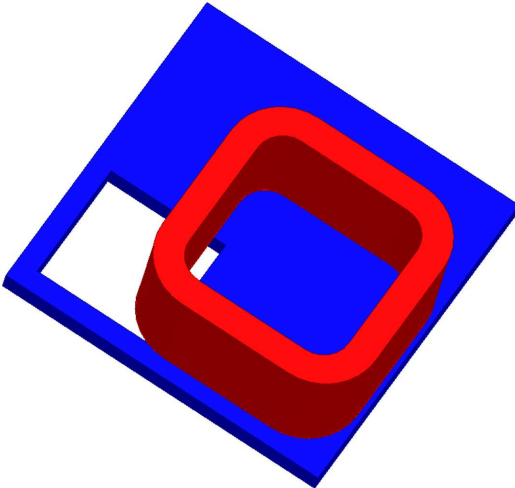


Fig. 3.5. The geometry of TEAM workshop problem 7.

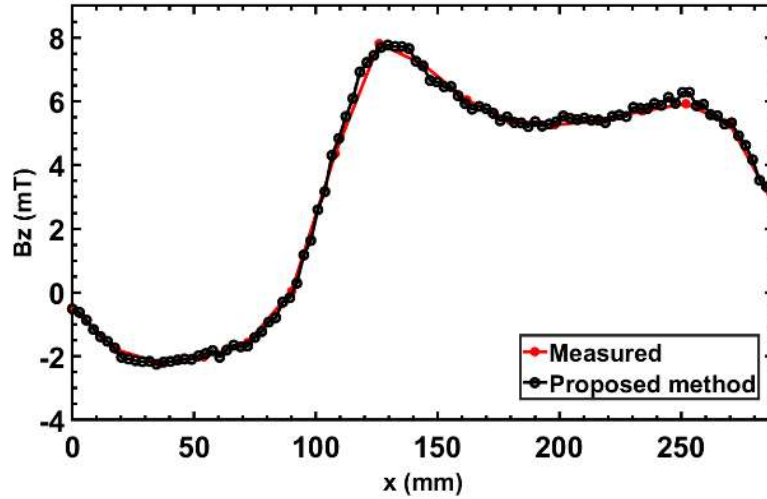


Fig. 3.6. Z-components  $B_z$  of magnetic flux densities along the line A1-B1.

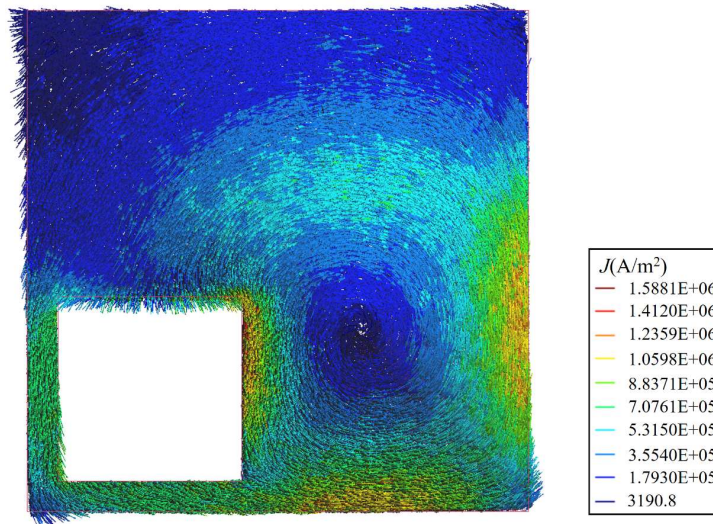


Fig. 3.7. The eddy current density in the aluminum plate at time instant  $t$ .

As another engineering application, the TEAM workshop problem 7 is solved with this adaptive DoFs FEM [18]. As shown in Fig. 3.5, the stranded racetrack-shaped coil over the asymmetrical conductor is excited by a 2742AT current, which varies sinusoidally at a frequency of 50 Hz. The conductivity of the aluminum plate is  $3.526 \times 10^7$  S/m. The drive current is excited from zero value at the starting point, and zero initial value is set for the unknown in this time dependent problem. The adaptive DoFs FEM time-stepping process is calculated to 25ms with a uniform time step of 0.5ms. The calculated Z-components  $B_z$  of magnetic flux densities along line A1-B1 (from (0, 72, 34) to (288, 72, 34)) are given in Fig. 3.6 along with the measured results.

During the time-stepping calculation, roughly about 37000 DoFs in the mesh containing 259869 DoFs are constrained in each step according to the guidance from the error estimator. The good agreement between calculated results and measured results, which is observed from Fig. 3.6, shows that the accuracy of the solution is not affected by the constrained DoFs. Moreover, about 20% of the computing time is saved for this problem when compared to conventional FEM, which showcases the effectiveness of the proposed method in solving 3-D transient magnetic problems. In addition, the calculated eddy current in the aluminum plate is shown in Fig. 3.7.

### **3.3 The Adaptive DoFs FEM for Thermal and Magneto-Thermal Field Analysis**

Based on the investigation of adaptive DoFs FEM, it is found that this method is applicable to magneto-thermal field analysis. The FE space of each field is built with one set of FEM mesh, and the requirement on discretization of each field is met by adapting the DoFs separately. The scale of the problem is reduced without intruding an extra mapping algorithm, and the errors resulted by the mapping algorithm are avoided.

#### **3.3.1 The Extension of Adaptive DoFs FEM**

Before applying the adaptive DoFs to solve coupled magneto-thermal problems, it is firstly extended to solve the thermal field. As introduced in the section 2.2, the numerical calculation process of the heat conduction equation is similar to that of the Maxwell equations. Also,  $h$ -type adaptive FEMs was proposed to solve the heat conduction problems [C28]. Error estimators, adaptive procedures in space, and control of time step sizes are involved in the method. When extending the adaptive

DoFs FEM to solve thermal field, the error estimator, which was used and validated in [C29], is adopted.

The exact values of temperature are derived in the same way as the magnetic field. The heat flux corresponds to the flux density in the magnetic field, and the corresponding parameter of magnetic potential is the temperature. With the assumed exact values, the energy error for the numerical solution is formulated as [C29]

$$(\varepsilon_m^e)^2 = \frac{\int_{V_e} \frac{1}{k} (\mathbf{q}^e - \mathbf{q}_{true}^e) \cdot (\mathbf{q}^e - \mathbf{q}_{true}^e) dV}{\int_{V_e} \frac{1}{k} \mathbf{q}^e \cdot \mathbf{q}^e dV} \times 100\% \quad (3 - 16)$$

where the heat flux  $\mathbf{q}^e$  is defined as

$$\mathbf{q}^e = \left[ k \frac{\partial T}{\partial x} \quad k \frac{\partial T}{\partial y} \quad k \frac{\partial T}{\partial z} \right] \quad (3 - 17)$$

Other techniques that are involved in the adaptive DoFs FEM are identical for these two field. In addition, owing to the scalar potential, the implementation process in thermal field is simpler when compared to the magnetic field. With the solvers developed for the magnetic and thermal field, the coupling procedures, and the temperature dependent characteristics, the extension of adaptive DoFs FEM to coupled magneto-thermal field is straightforward. These two fields are solved iteratively until the convergence criterion is met. Another coupling strategy, in which the same mesh is used for both fields without any adaption, is considered for comparison and mutual authentication. Two types of numerical examples, one for thermal field analysis and the other for coupled magneto-thermal field analysis, are calculated to showcase the effectiveness of this method.

### 3.3.2 Numerical Examples

The numerical example for thermal field analysis is a validation case from ANSYS [C30]. The numerical problem is to compute the temperature distribution in a

long thick-walled cylinder, the outer and inner surfaces of which are maintained at the temperature of  $-17.78^{\circ}\text{C}$  and  $-18.33^{\circ}\text{C}$ , respectively. As shown in Fig. 3.8, a numerical model is built with one-quarter of the cylinder and the axial length specified as  $2.54\text{mm}$ . Owing to the special structure, these four cutting surfaces are adiabatic. With 400 nodes in the mesh with 3505 nodes specified as slaves, the calculated temperature, which is shown in Fig. 3.8, is consistent with the reference. In addition, the temperatures of three points, P1 (4.76, 0.0, 0.0), P2 (7.08, 0.0, 0.0), and P3 (15.88, 0.0, 0.0), are compared with the referenced values given in [C30], which validates the correctness of the adaptive DoFs FEM solver developed for thermal field.

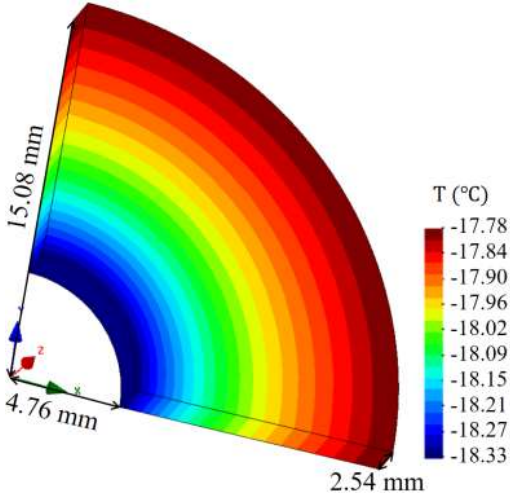


Fig. 3.8. The geometry and temperature of the cylinder.

Table 3.6. Comparison of the temperature for three fixed points.

	Target ( $^{\circ}\text{C}$ )	Numerical( $^{\circ}\text{C}$ )	Error ( $^{\circ}\text{C}$ )
Temperature (P1)	-18.33	-18.33	0.00
Temperature (P2)	-18.15	-18.12	0.03
Temperature (P3)	-17.78	-17.78	0.00

Based on the TEAM workshop problem 20, which is solved in the section 3.2.3, a magneto-thermal coupling problem is formed by considering the temperature dependence of the materials. The effect of eddy currents is neglected and the sinusoidal field ( $f = 60\text{Hz}$ ) is approximated by the static analysis results. All the surfaces, except

the symmetry faces, are specified with convective boundaries. The formulas for the losses computation and properties update are introduced in section 2.2.2, and the related coefficients of these formulas are listed in Table 3.7. A mesh with 19193 thermal DoFs and 129287 magnetic DoFs are generated for the coupling problem.

Table 3.7. The parameters in the fourth example.

Parameter	$k_h$	$k_c$	$k_e$	$k_\sigma$	$k_\mu$
Value	0.005697	0.000078	0.0	0.006800	0.001088

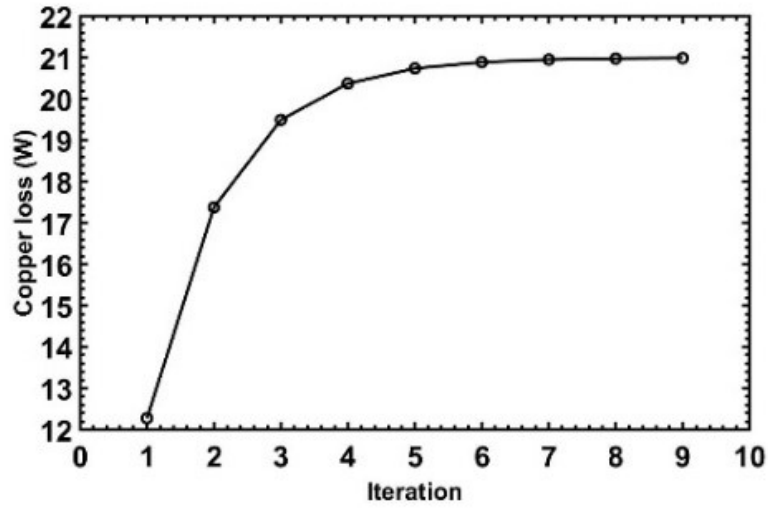


Fig. 3.9. The convergence curve of the calculated copper loss.

It takes nine steps for the iteration between these two fields to converge, and the convergence curve of the copper losses is shown in Fig. 3.9. There are roughly fifteen hundred thermal DoFs and ten thousand magnetic DoFs are specified as slave DoFs in each iteration. For magnetic field involving nonlinearity, the NR iteration terminates after thirteen steps. As shown in Fig.3.10, the magnetic flux density derived by the coupled simulation is slight smaller than the solution obtained in the magnetic field analysis. In other words, the magnetic field analysis gives overestimated results when neglecting the effect of temperature. In addition, the core losses witness a decrease trend in the iteration process. The same phenomenon is observed for the magnetic force acting on the center pole. As shown in Fig. 3.11, the temperature distribution derived

by the adaptive DoFs coupling analysis is in good accordance with the solution obtained by the referenced strategy, in which the same mesh is used for both fields without any adaption, while the proposed method only takes 30% of the time consumed by the referenced strategy.

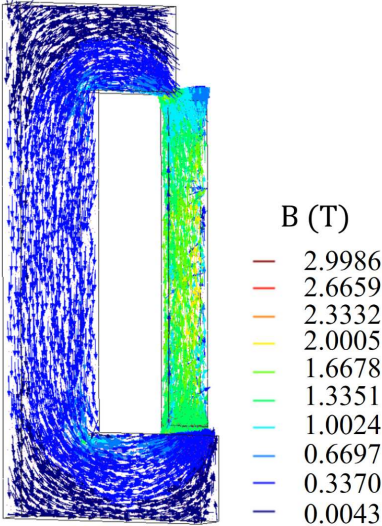


Fig. 3.10. The magnetic flux density obtained by the coupling analysis.

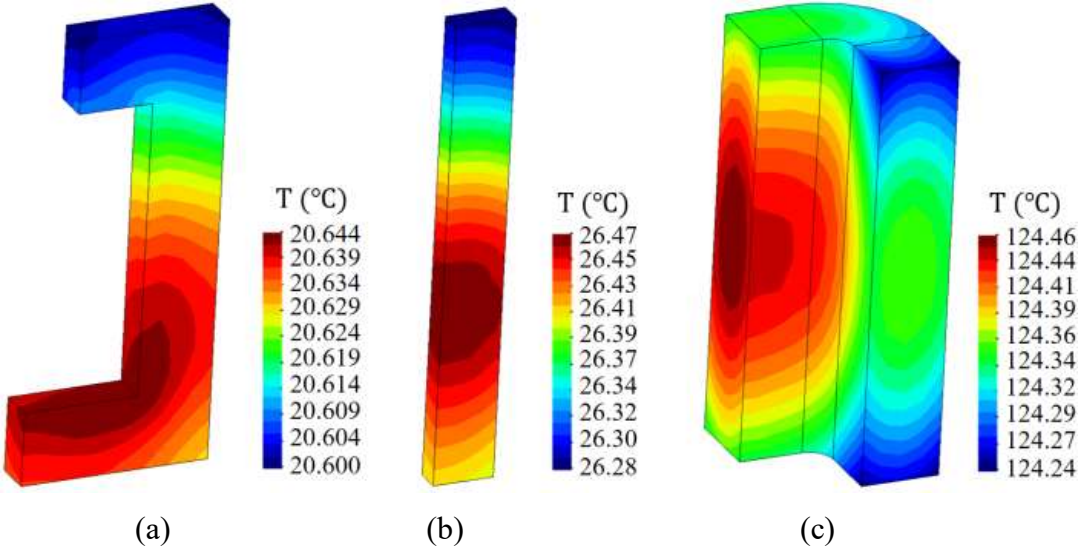


Fig. 3.11. The temperature of (a) the yoke, (b) the center pole and (c) the coil.

The modified TEAM workshop problem 7 [11], in which the temperature dependence of conductivity is considered, is solved using the proposed method. In order to obtain the steady state performance, the magnetic transient solver is coupled

with the thermal static solver. The temperature coefficients for the conductivity of aluminum plate and copper winding are 0.0039 and 0.00404, respectively. The adaptive DoFs FEM time-stepping process is calculated to  $t = 25 \text{ ms}$  with a uniform time step of  $0.5 \text{ ms}$ , and the thermal solver is invoked after every ten steps of magnetic field computation. During the adaptive computation, a mesh with 467202 elements are produced, and roughly 17% of the magnetic DoFs and 29% of the thermal DoFs are constrained in each step. As shown in Fig. 3.12, the calculated  $Z$ -components  $B_z$  of magnetic flux densities along line A1-B1 (from  $(0, 72, 34)$  to  $(288, 72, 34)$ ) are plotted along with the measured results, and the good agreement between these two solutions validates the correctness of the propose method. The derived temperature, which is shown in Fig. 3.13, is close to the results obtained without any constrained DoFs. Overall, the computational load is reduced by about 18% using the proposed method, while the accuracy of the results is not affected. For illustration, the derived eddy current density in the aluminum plate is given in Fig. 3.14. It is observed that the magnitude is slightly smaller than that obtained in the magnetic field analysis, and this is consistent with the variation in resistance after considering the temperature characteristics.

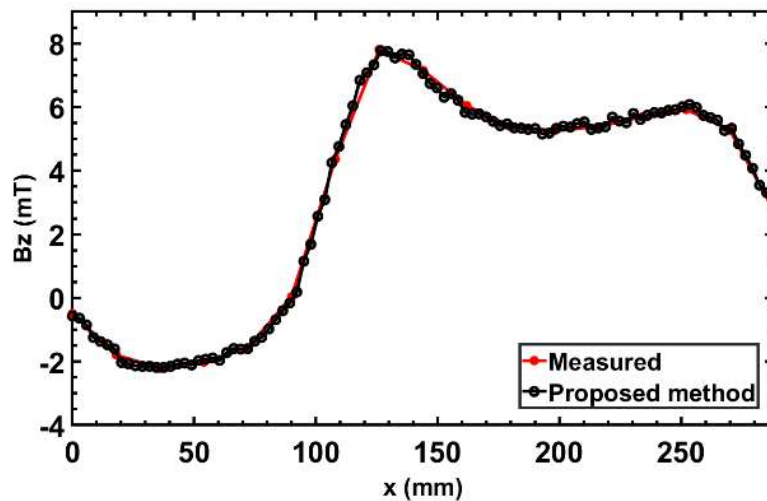


Fig. 3.12.  $Z$ -components  $B_z$  of magnetic flux densities along the line A1-B1 (coupled).

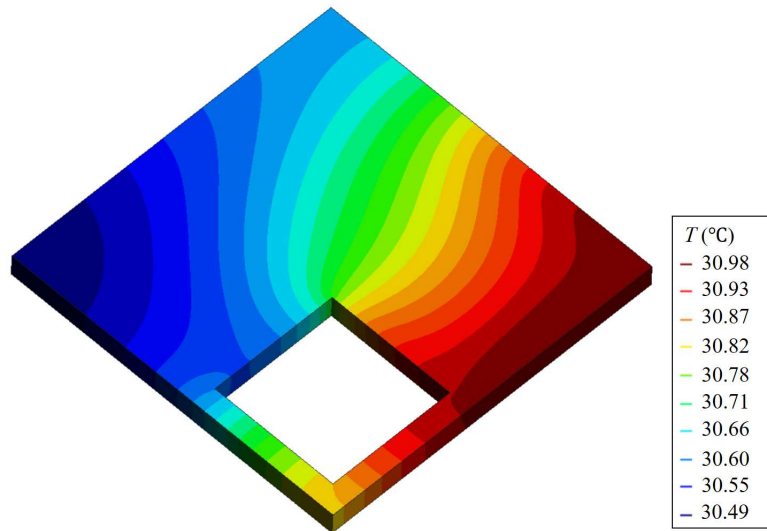


Fig. 3.13. The temperature contours of the aluminum plate at time instant  $t$ .

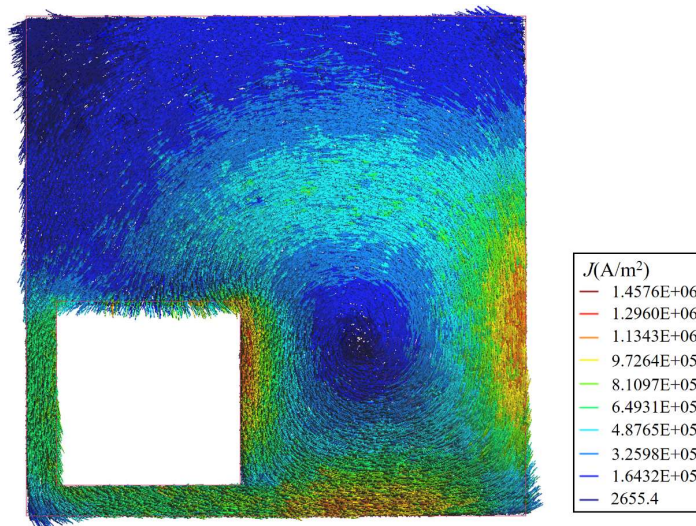


Fig. 3.14. The eddy current density in the aluminum plate at time instant  $t$  (coupled).

### 3.4 Summary

An adaptive DoFs FEM is presented for 3D nonlinear magnetic field, thermal field, and coupled magneto-thermal field analysis in this chapter, and several numerical examples for this three types of fields are calculated. In this method, the explicit nodes removing is replaced by eliminating the corresponding DoFs implicitly, and a type of constraint is proposed to tackle the 3D field. The dimensions of system are reduced mathematically, while the rearrangement of mesh data for coarsening operation is no longer needed. Owing to the simple and flexible constraint, this

algorithm is easily implemented and extended.

In the coupled analysis, the FE spaces of these two fields are built with one set of mesh, and the DoFs of these two fields are adjusted separately according to their respective requirements. These slave DoFs are eliminated and recovered by using the constraint and the slave-master technique. Hence, mapping algorithms are not required for the data transfer between fields, and the different discretization requirements are met. The effectiveness of this method in terms of efficiency and accuracy is showcased by numerical examples.

### 3.5 Reference-Part C

- [C1] Z. J. Cendes and D. N. Shenton, “Adaptive mesh refinement in the finite-element computation of magnetic-fields”, *IEEE Trans. Magn.*, vol. 21, no. 5, pp. 1811-1816, 1985.
- [C2] A. Schmidt, K.G.Siebert, “*Design of Adaptive Finite Element Software: The Finite Element Toolbox ALBERTA,*” 1st edn, Springer-Verlag Berlin Heidelberg, New York, 2004.
- [C3] W.Z. Huang, “Practical aspects of formulation and solution of moving mesh partial differential equations,” *J. Comput. Phys.*, vol. 171, pp. 753–775, 2001.
- [C4] W.Z. Huang, J.T. Ma, R.D. Russell, “A study of moving mesh PDE methods for numerical simulation of blowup in reaction diffusion equations,” *J. Comput. Phys.*, vol. 227, pp. 6532–6552, 2008.
- [C5] M.M. Ilic, A.Z. Ilic, B.M. Notaros, “Efficient large-domain 2-D FEM solution of arbitrary waveguides using p-refinement on generalized quadrilaterals,” *IEEE Trans. Microwave Theory Tech.*, vol. 53, no. 4, pp. 1377–1383, 2005.
- [C6] D. Ladas, V. Mazauric, G. Meunier, et al., “An energy based approach of electromagnetism applied to adaptive meshing and error criteria,” *IEEE Trans. Magn.*, vol. 44, no. 6, pp. 1246–1249, 2008.

- [C7] S. Matsutomo, S. Noguchi, H. Yamashita, "Adaptive mesh generation method utilizing magnetic flux lines in two-dimensional finite element analysis," *IEEE Trans. Magn.*, vol. 48, no. 2, pp. 527–530, 2012.
- [C8] D. Azocar, M. Elgueta, M.C. Rivara, "Automatic LEFM crack propagation method based on local Lepp-Delaunay mesh refinement," *Adv. Eng. Software*, vol. 41, pp. 111–119, 2010.
- [C9] I. Kossaczky, "A Recursive Approach to Local Mesh Refinement in 2 and 3 Dimensions," *J. Comput. Appl. Math.*, vol. 55, no. 3, pp. 275-288, 1994.
- [C10] E. Bansch, "Adaptive finite element techniques for the Navier–Stokes equations and other transient problems," *Adaptive Finite and Boundary Element Methods* Southampton: Computational Mechanics Publications, pp. 47–76, 1993.
- [C11] O. C. Zienkiewicz, and J. Z. Zhu, "A simple error estimator and adaptive procedure for practical engineering analysis," *Int. J. Numer. Meth. Eng.*, vol. 24, pp. 337-357, 1987.
- [C12] E. Q. Hu, X. Z. Chen, and K. D. Zhou, "A new posteriori error estimate and adaptivity approach for electromagnetic field finite element computations," *Proc. CSSE*, vol. 17, no. 2, pp. 78-83, Mar. 1997.
- [C13] J. B. Li, D. X. Xie, and X. M. Liu, "A posteriori error estimation and adaptive mesh refinement controlling in finite element analysis of 3-D steady state eddy current field," *IEEE Trans. Magn.*, vol. 46, no. 8, pp. 3500-3503, Aug. 2010.
- [C14] T. L. Horvath, and F. Izsak, "Implicit a posteriori error estimation using patch recovery techniques," *Central Eur. J. Math.*, vol. 10, no. 1, pp. 55-72, 2012.
- [C15] D. Ladas, V. Mazauric, G. Meunier, O. Chadebec, M. Ebene-Ebene, Y. Marechal, and P. Wendling, "An energy based approach of electromagnetism applied to adaptive meshing and error criteria," *IEEE Trans. Magn.*, vol. 44, no. 6, pp. 1246-1249, Jun. 2008.
- [C16] S. Matsutomo, S. Noguchi, and H. Yamashita, "Adaptive mesh generation method utilizing magnetic flux lines in two-dimensional finite element analysis," *IEEE Trans. Magn.*, vol. 48, no. 2, pp. 527-530, Feb. 2012.

- [C17] K. Yamazaki, S. Watari, T. Saeki, Y. Sugiura, "Adaptive finite element meshing at each iterative calculation for electromagnetic field analysis of rotating machines," *Electr. Eng. Japan*, vol. 164, no. 3, pp. 78–91, 2008.
- [C18] Y. P. Zhao, S. L. Ho, and W. N. Fu, "A novel adaptive mesh finite element method for nonlinear magnetic field analysis," *IEEE Trans. Magn.*, vol. 49, no. 5, pp. 1777-1780, May 2013.
- [C19] Y. P. Zhao, S. L. Ho, and W. N. Fu, "An Adaptive Degrees-of-Freedom Finite-Element Method for Transient Magnetic Field Analysis," *IEEE Trans. Magn.*, vol. 49, no. 12, pp. 5724-5729, 2013.
- [C20] 'Lecture notes, Chapter 8, MultiFreedom Constraints I', <http://www.colorado.edu/engineering/cas/courses.d/FEM.d/IFEM.Ch08.d/IFEM.Ch08.pdf>
- [C21] M. Wicke, M. Botsch, and M. Gross, "A finite element method on convex polyhedra," *Comput. Graph. Forum*, vol. 26, no. 3, pp. 355-364, 2007.
- [C22] W. N. Fu and, "Elimination of nonphysical solutions and implementation of adaptive step size algorithm in time-stepping finite-element method for magnetic field-circuit-motion coupled problems," *IEEE Trans. Magn.*, vol. 46, no. 1, pp. 29–38, Jan. 2010.
- [C23] Y. P. Zhao and W. N. Fu, "A Novel Formulation with Coulomb Gauge for 3-D Magnetostatic Problems Using Edge Elements," *IEEE Trans. Magn.*, vol. 53, no. 6, Jun 2017.
- [C24] 'Axial Field of a Finite Solenoid', <https://tiggerntatie.github.io/emagnet/solenoids/solenoidonaxis.htm>.
- [C25] Bíró, O.: 'Solution of TEAM benchmark problem #20 (3-D static force problem)', in *Proc. 4th Int. TEAM Workshop*, Miami, 1993, pp. 23–25
- [C26] J. L. Coulomb, "A Methodology for the Determination of Global Electromechanical Quantities from a Finite-Element Analysis and Its Application to the Evaluation of Magnetic Forces, Torques and Stiffness," *IEEE Trans. Magn.*, vol. 19, No. 6, pp. 2514-2519, 1983.
- [C27] N. Takahashi, T. Nakata, and H. Morishige, "Summary of results for problem 20 (3-D static force problem)," *COMPEL-Int. J. Comput. Math. Elect. Electron. Eng.*, vol. 14, nos. 2–3, pp. 57–75, 1995.

- [C28] A. S. Franca and K. Haghghi, “Adaptive finite-element analysis of transient thermal problems,” *Numer. Heat Tr. B-Fund.*, vol. 26, no. 3, pp. 273-292, Apr. 1994.
- [C29] H. C. Huang and R. W. Lewis, “Adaptive Analysis for Heat Flow Problems Using Error Estimation Techniques,” *Proc. Sirth Int. Conf: for Numerical Methods in ntermal Problems*, vol. 6, pp. 1029-1044, Pineridge Press, Swansea, U.K., 1989.
- [C30] ANSYS, version 18.2, Pittsburgh: ANSYS, Aug. 2017.

# **Chapter 4 Convective Heat Transfer of Nanofluids in Transformers**

As introduced in the section 2.3.1, the hot-spot temperature-rise of oil-immersed transformers has attracted increasing attentions [D1]. Many investigations have been conducted for the heat transfer of disc-type windings. Based on the existing studies, a comprehensive investigation on the natural convective nanofluids in disc-type windings is presented in this chapter. It is the first time to employ the multi-phase mixture model to study such a nanofluid flow, and the single-phase model is also considered for mutual authentication and comparison.

## **4.1 Introduction to the Heat Transfer in Transformer**

The power losses of transformer active parts, such as iron structures, core, and windings, are converted into heat during the operation, and the generated heat is then diffused to the ambient, which results in a synchronous temperature rise through the heat transfer path. Five stages are included in the heat transfer path of ON transformer: 1) heat conduction from the interior hot-spot to surfaces in the active parts; 2) convective heat transfer between the active parts and oil; 3) convective heat transfer between oil and the internal tank surface; 4) heat conduction in the tank; 5) convective heat transfer over the tank surface and heat radiation. In the OF transformer, there is one more heat transfer path, which is the warmed up and pumped out transformer oil. It takes several hours for the transformers to reach the thermal equilibrium.

With the ability to handle complex flow field, irregular geometry, and nonlinear materials, numerical methods, such as FVM and FEM, have been widely used in the heat transfer analysis of transformers. Some studies focus on the integral analysis of transformers, which can derive a comprehensive solution on the thermal and flow field.

In [D2], the heat transfer in an ONAN three-phase three-limb transformer is analyzed by the FVM. The measured losses are used as heat sources in the thermal field solver, and the simulation results of temperature are validated by the measured temperatures. In addition, coupled analysis, such as magneto-fluidic-thermal analysis, is also used to consider the temperature dependent parameters. In [D3], a 3D magneto-fluidic-thermal analysis of a 10kV oil-immersed triangular wound core transformer is presented. Heat generated by the core and windings are derived in the electromagnetic analysis using the FEM, and the thermal and fluidic field are solved by the FVM. The effect that temperature has on the losses is taken into consideration, and the numerical results are validated by the analytical method presented in the IEC standards. DC bias is considered with the field-circuit coupled FEM in [D4]. The implementation process of magneto-fluidic-thermal analysis is presented in detail by a three-phase dry-type power transformer.

Since the hot-spot temperature rise in transformers is critical for the safe operation, many investigations have been conducted on the related topics. The hot-spot temperature-rise in the structural parts of an ODFS-334 MVA/500 kV single-phase auto-transformer is computed by a coupling approach. The stray losses in the structural parts are obtained by the magnetic field analysis, and are then transferred to the fluid-thermal solver to compute the convective heat transfer coefficient, with which the thermal field is finally solved by the magnetic-thermal coupling algorithm [D5]. To investigate the hot-spot temperature rise in windings, the convective heat transfer in the windings is widely studied. A comprehensive literature review on the thermal modeling, which including the analytical model, CFD model, and measurement, are published by the CIGRE working group A2.38 [D1]. F. Torriano et al. investigated the effect that the inlet boundary conditions and the numerical model have on the temperature and flow distributions numerically [D6, D7]. A 2D model is constructed for one pass of the disc-type transformer winding, and the effect of inlet position is studied [D6]. Since the effect of sticks and duct spacers is neglected in the 2D model, a 3D model is built to derive a more accurate solution [D7]. The 3D computations are however very time consuming, and for this reason a modification strategy for the 2D model is proposed based on the

3D field computations. To investigate the coupling between passes, Alex Skillen et al. built a complete numerical model for a transformer winding with four passes, and the temperature rise at hot-spot is predicted by an open source CFD code [D8].

## **4.2 Numerical Study for One Pass of the Winding**

In order to apply the nanofluid to the transformer cooling, the heat transfer of nanofluid in windings needs to be investigated. To the best knowledge of the author, there is no experimental or numerical studies on the heat transfer in nanofluid cooled transformer windings. Limited studies [D9, D10] were conducted on the convective heat transfer of nanofluid in simple containers. In this section, the numerical study of natural convective heat-transfer of nanofluid (oil/SiC) in disc-type winding is presented. The study is based on the numerical model of one pass of the winding [D6], and both the single-phase model and multi-phase mixture model are used for mutual authentication and comparison. The numerical model and solver are validated by the existing results of the referenced model, which has the same dimensions as [D6] and is cooled by transformer oil. The mass flow distribution and the pressure drop are evaluated along with the temperature distribution.

### **4.2.1 The Numerical Model**

In order to estimate the performance of nanofluid, an ON transformer [D6], which is rated at 66MVA, is modified by replacing the regular transformer oil with nanofluid (oil/SiC), and then studied numerically. As shown in Fig. 4.1, an axisymmetric 2D model rather than 3D model is constructed for one pass of the low-voltage windings, and the effect of sticks and duct spacers is neglected in the 2D model. Nineteen discs, twenty horizontal ducts, and two vertical ducts are included in the pass. The horizontal

ducts and discs are sequentially numbered from bottom to top. In this numerical model, the insulation board surrounding the conductors are considered, and no heat sources are imposed on this component. The dimensions of the notations shown in Fig. 4.1 are given as below:

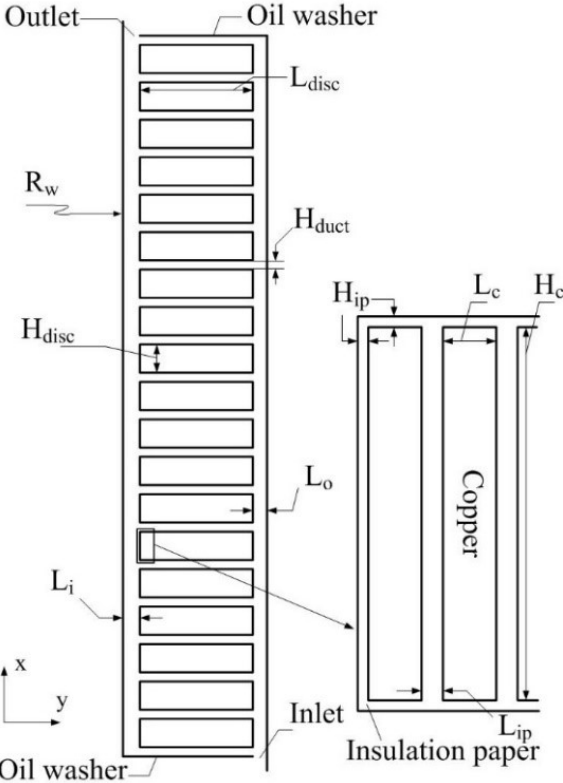


Fig. 4.1 The model of one pass of the low-voltage windings.

- $L_{disc} = 0.0522 \text{ (m)}$
- $R_w = 0.3162 \text{ (m)}$
- $H_{duct} = 0.0051 \text{ (m)}$
- $H_{disc} = 0.015 \text{ (m)}$
- $L_o = 0.0064 \text{ (m)}$
- $L_i = 0.0089 \text{ (m)}$

$$H_{ip} = 0.0004 \text{ (m)}$$

$$L_{ip} = 0.0008 \text{ (m)}$$

$$L_c = 0.0021 \text{ (m)}$$

$$H_c = 0.0143 \text{ (m)}$$

Oil is directed into the pass through the outer vertical duct, flows through the horizontal ducts, joins together and flows out at the inner vertical duct. For windings with several passes, the direction of the horizontal oil flows changes inversely along the passes. The zig-zag windings form an efficient cooling system by these two types of passes, which have opposite inlet positions. Hence, both types of passes are included in the study.

A homogeneous heat source ( $676.9W/disc$ ) is imposed on the conductors, and the error produced by non-uniform eddy losses is ignored. The surrounding cylinders and these two oil washers, which have low thermal conductivity, are as assumed to be adiabatic. A pressure boundary condition ( $0 Pa$ ) is specified for the outlet. The inlet boundary condition, which is obtained by heat run test for transformer oil cooling [D11], is used for nanofluid cooling, and the velocity and temperature of the inlet flow are  $0.0592 m/s$  and  $319.85K$ , respectively. The effect that the usage of nanofluid has on the inlet boundary condition is ignored to isolated the influence of nanofluid on heat transfer in windings.

All the properties of the materials, except for the transformer oil properties, are treated as temperature independent and are given in table 1. The temperature dependent properties of transformer oil are formulated as follows [D12]:

$$\rho_f = 1098.72 - 0.712T \quad (4 - 1)$$

$$C_f = 807.163 + 3.58T \quad (4 - 2)$$

$$\mu_f = 0.08467 - 4.0 \times 10^{-4}T + 5.0 \times 10^{-7}T^2 \quad (4 - 3)$$

$$k_f = 0.1509 - 7.101 \times 10^{-5}T \quad (4 - 4)$$

where; the subscript  $f$  is the index of transformer oil;  $\rho$  is the density;  $C$  is the specific heat;  $\mu$  is the viscosity;  $k$  is the thermal conductivity.

Table 4.1. Material Properties.

Material	Density ( $kg\ m^{-3}$ )	Specific heat ( $W\ kg^{-1}\ K^{-1}$ )	Thermal conductivity ( $W\ m^{-1}\ K^{-1}$ )
Copper	8933	385	401
Insulation	930	1340	0.19
SiC	3160	750	490

## 4.2.2 The Nanofluid Model

The governing equations, which are used to represent the fluid field, depend on the nanofluid model and the pattern of fluid motion. The nanofluid is regarded as conventional single-phase fluid in the single-phase model, and is integrally modelled by the measured or calculated equivalent properties [D13-D18]. No more equations and additional terms are required to model the dispersed nanoparticles and the interaction between phases. In the multi-phase mixture model [D15, D16], the volume fraction conservation equation and modified terms regarding to the velocity discrepancy between phases are considered in the governing equations. The pattern of fluid motion is evaluated by the Reynolds number, and the critical value for laminar flow is below than 2100. To calculate the Reynolds number for the studied flow, the nanofluid flow is regarded as a pure single-phase model, and the properties of the studied nanofluid are predicted by the models introduced in section 2.4. The average flow velocity is replaced by a larger inlet velocity. The calculated Reynolds number is about 1000, which is far below the critical value. Hence, the nanofluid flow is laminar and no turbulence model is required.

With the governing equations determined, the problem is then discretized and solved using the numerical methods. The momentum and energy are discretized in space with the second order upwind scheme. This convective heat transfer problem is finally solved by the FVM based software ANSYS-Fluent.

In the single-phase model, the governing equations for the nanofluid flow represented are identical to the conventional single-phase flow, while the equations are formulated for the mixture, as given by

Continuity,

$$\nabla \cdot (\rho_{nf} \mathbf{V}) = 0 \quad (4 - 5)$$

Momentum and,

$$\nabla \cdot (\rho_{nf} \mathbf{V} \mathbf{V}) = -\nabla P + \nabla \cdot (\mu_{nf} \nabla \mathbf{V}) + \rho_{nf} \mathbf{g} \quad (4 - 6)$$

Energy,

$$\nabla \cdot (\rho_{nf} \mathbf{V} C_{nf} T) = \nabla \cdot (k_{nf} \nabla T) + S_e \quad (4 - 7)$$

where the subscript  $nf$  is the index of nanofluid.

Since the mixture model is an incomplete multi-phase model, its governing equations are also formulated for the mixture. Unlike the single-phase model, the interaction and velocity difference between phases are concerned in the conservation equations of energy and momentum. In addition, one more equation for the conservation of volume fraction is added to the governing equations, which are given by

Continuity,

$$\nabla \cdot (\rho_{nf} \mathbf{V}_m) = 0 \quad (4 - 8)$$

Momentum and,

$$\nabla \cdot (\rho_{nf} \mathbf{V}_m \mathbf{V}_m) = -\nabla P + \nabla \cdot \tau + \rho_{nf} \mathbf{g} + \nabla \cdot \left( \sum_{k=1}^2 \phi_k \rho_k \mathbf{V}_{dr,k} \mathbf{V}_{dr,k} \right) \quad (4 - 9)$$

Energy,

$$\nabla \cdot \left( \sum_{k=1}^2 \phi_k \mathbf{V}_k (\rho_k E_k + P) \right) = \nabla \cdot (k_{nf} \nabla T) + S_e \quad (4-10)$$

Volume fraction,

$$\nabla \cdot (\phi \rho_p \mathbf{V}_m) = \nabla \cdot (\phi \rho_p \mathbf{V}_{dr,p}) \quad (4-11)$$

The mass-averaged velocity of the nanofluid is defined by

$$\mathbf{V}_m = \frac{\sum_{k=1}^2 \phi_k \rho_k \mathbf{V}_k}{\rho_{nf}} \quad (4-12)$$

The stress tensor  $\tau$  is

$$\tau = \mu_{nf} \nabla \mathbf{V}_m \quad (4-13)$$

The drift velocity  $\mathbf{V}_{dr,p}$  is formulated with the relative velocity  $\mathbf{V}_{pf}$

$$\mathbf{V}_{dr,p} = \mathbf{V}_{pf} - \sum_{k=1}^2 \frac{\phi_k \rho_k}{\rho_{nf}} \mathbf{V}_{fk} \quad (4-14)$$

where the relative velocity is derived with the assumption of a local equilibrium [D19]

$$\mathbf{V}_{pf} = \frac{\rho_p d_p^2}{18 \mu_f f_{drag}} \frac{(\rho_p - \rho_{eff})}{\rho_p} \mathbf{a} \quad (4-15)$$

The acceleration  $\mathbf{a}$  is defined as

$$\mathbf{a} = \mathbf{g} - (\mathbf{V}_m \cdot \nabla) \mathbf{V}_m \quad (4-16)$$

and the  $f_{drag}$  is the drag force function [D20]

$$f_{drag} = \begin{cases} 1 + 0.15 Re_p^{0.687} & Re_p \leq 1000 \\ 0.0183 Re_p & Re_p > 1000 \end{cases} \quad (4-17)$$

It can be found that the governing equations of the mixture model include the continuity, momentum, and energy equations of nanofluid, the volume fraction equation of nanoparticles, and the algebraic expressions of the relative velocities. Hence, more variables are involved in the multi-phase mixture model when compared with the single-phase model, while the volume fraction distribution can be obtained

using the mixture model.

### 4.2.3 The Validation of Numerical Model and the Grid Independence Study

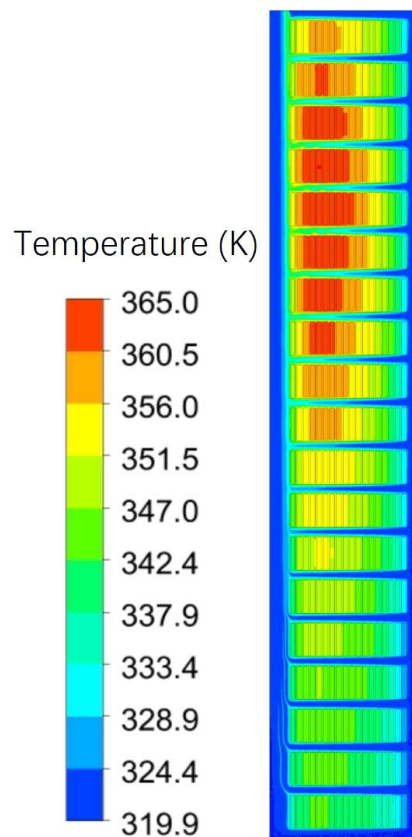


Fig. 4.2. The temperature contours of the referenced winding.

The nanofluid flow is solved by the same solver as transformer oil flow. In order to verify the effectiveness of the solver and numerical model, the referenced winding cooled by transformer oil is modelled and recalculated, and the derived solutions are compared with the existing results in [D6]. As shown in Fig. 4.2, the numerical analysis gives the same hot-spot location (disc 16), and the maximum temperature is 365.04K, about 0.9% (3.5K) lower than the reference. Moreover, the derived mass flow rate fractions, which are shown in Fig. 4.3, are in good accordance with the

referenced results. Among the horizontal ducts, most of the oil (18% to 19%) flows into the first duct, and the last duct have a relatively small mass flow rate fraction (about 3%). These are consistent with the reference, hence the effectiveness of the solver and the correctness of the model are validated.

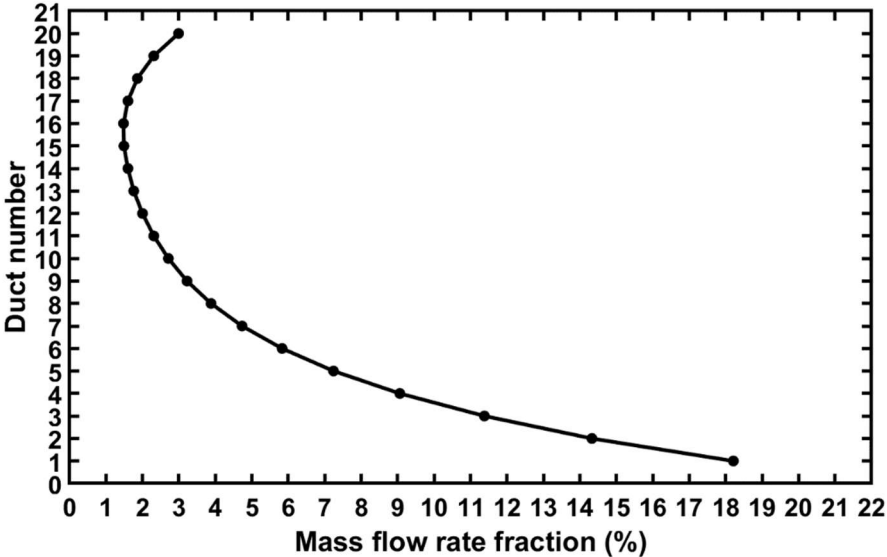


Fig. 4.3. The mass flow rate distribution of the referenced winding.

The validated solver is used to compute these two modified passes cooled by transformer oil, and the derived results are used as the references to estimate the heat transfer performance improvement after usingnanofluid. Since the inlet of the former pass is narrower than the latter one, it temperature is much higher than the latter pass, as shown in Fig. 4.4. The generated FVM mesh contains about 1.2 million quadrilateral elements, and part of the mesh is given in Fig. 4.4(a). Form the obtained mass flow rate distribution among the horizontal ducts (see Fig. 4.5), it is found that the mass flow rate distribution of the pass with inlet on the inner vertical duct is relatively uniform when compared with the other pass, which leads to a smaller temperature difference among the discs. The mass flow rate distribution (*MFRD*) is used to estimate the flow distribution, and it is defined as

$$MFRD_i = \frac{M_i}{(\sum_{k=1}^{20} M_k)/20} = \frac{M_i}{M_{mean}} \quad (4 - 18)$$

As shown in Fig. 4.5, discs, which are surrounded by horizontal ducts with the smallest  $MFRD$ , have the highest temperature-rise. The hot-spot locations of these two passes are disc fourteen and disc fifteen, respectively.

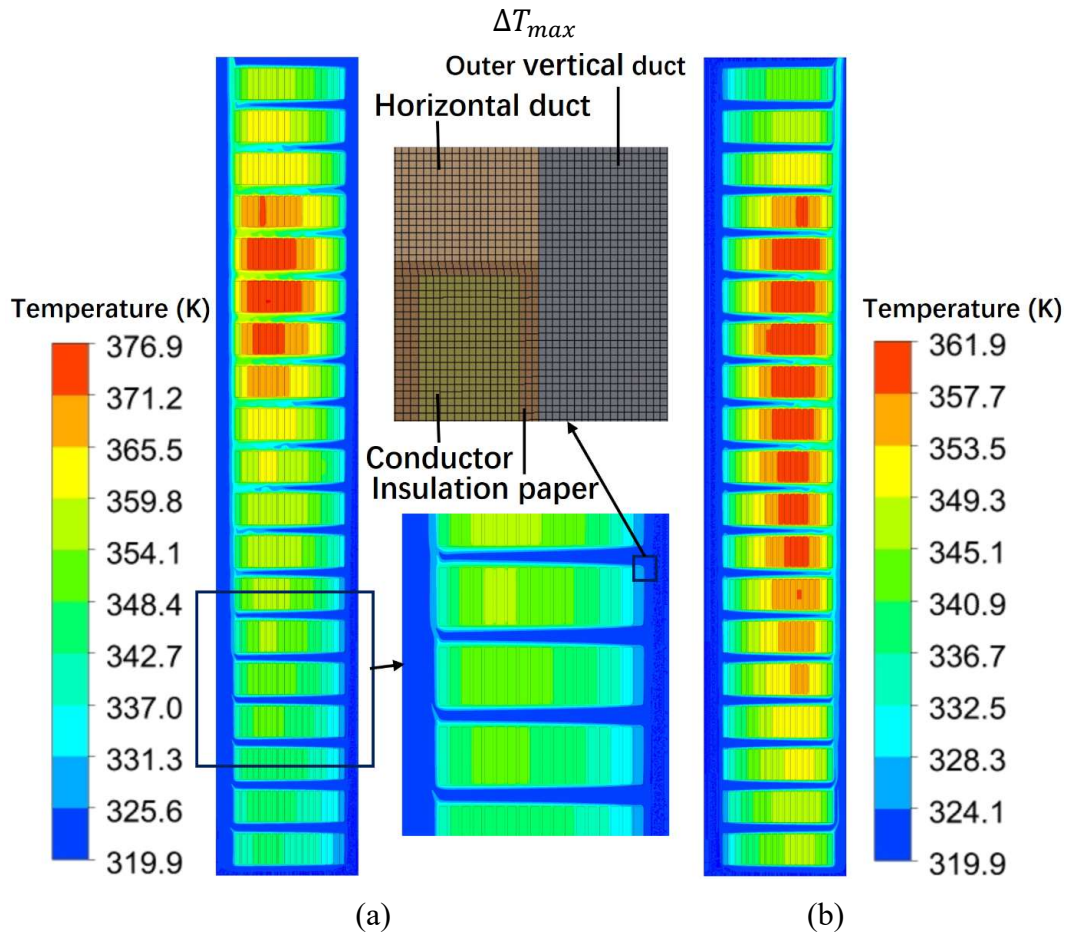


Fig. 4.4. (a) The temperature contours of the pass with inlet on the outer vertical duct and part of the mesh. (b) The temperature contours of the pass with inlet on the inner vertical duct.

The mesh generated for the simulation of transformer oil cooled winding is adopted to investigate the oil/SiC nanofluid flow, which has 1% concentration of nanoparticles. The grid-independence of the simulation is ensured by two refined meshes. For simple flows, the grid-independence of results is estimated with the variation of the average Nusselt number [D21]. However, this parameter is difficult to

determine in complicated geometries. For this reason, another alternative is to estimate the variation of maximum and mean temperature. With the element sizing constrained globally, the mesh is refined for two times, producing two meshes with roughly 8% and 16% more elements. By comparing the results of these two meshes, it is found that the changes of maximum and average temperature are 0.4% (1.39K) and 0.3% (0.85K) when using the mixture model, and the corresponding variations for the single-phase model are 0.2% (0.59K) and 0.3% (0.97K), respectively. Hence, for this studied problem, the initial mesh is feasible.

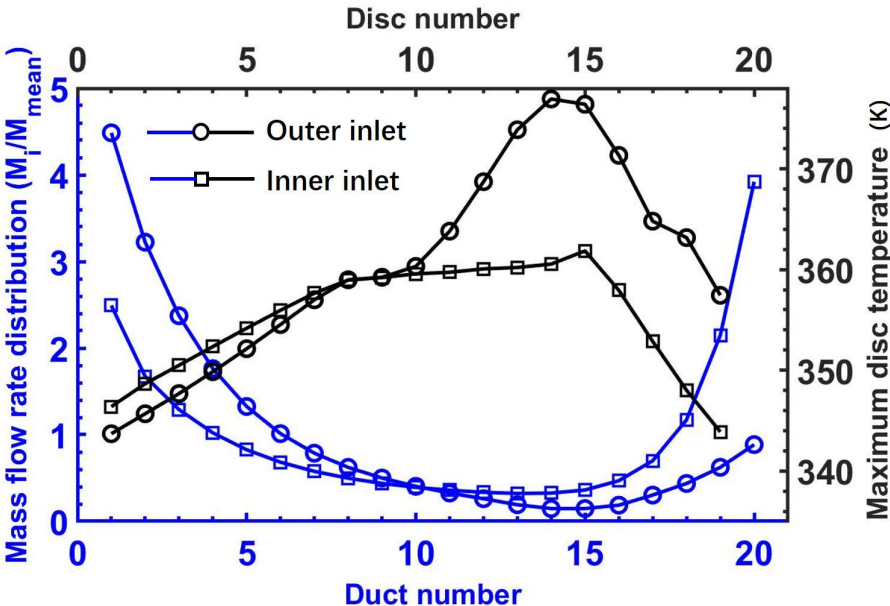
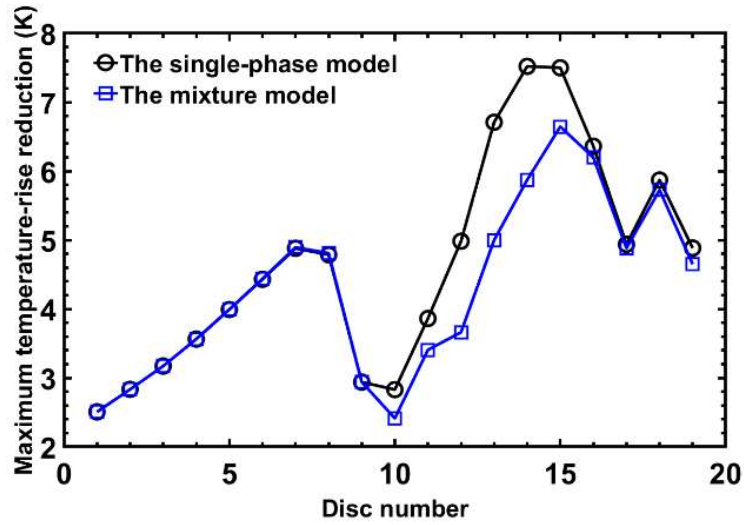


Fig. 4.5. The flow and temperature distribution for these two passes.

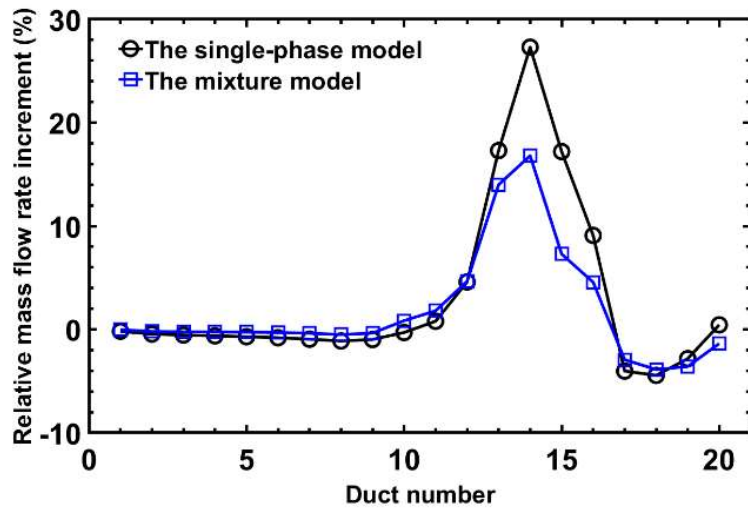
### 4.2.4 Results and Discussion

The convective heat transfer coefficient increases if the thermal conductivity is improved. Hence, it is possible to dissipate the same amount of heat with a smaller temperature difference. After adding the SiC nanoparticles, the viscosity and thermal conductivity of the transformer oil is increased. Hence, the cooling performance is expected to be improved. In the following studies, both the multi-phase mixture model

and the single-phase model are used for mutual authentication and comparison.



(a)



(b)

Fig. 4.6. (a) The maximum temperature-rise reduction and (b) relative mass flow rate increment for the pass with inlet on the outer vertical duct and nanofluid cooling.

From the numerical results of the nanofluid flow in the pass with inlet on the outer vertical duct, which are given in Fig. 4.6 and Fig. 4.7(b), it is found that there is an overall temperature reduction when compared with the references. The vertical axis title of Fig. 4.6(a), namely, the maximum temperature-rise reduction, which is computed for each disc, is defined as:

$$p_1 = T_f^{max} - T_{nf}^{max} \quad (4 - 19)$$

The peak locations of the curves in Fig. 4.6(a) are almost consistent with the hot-spot location of the corresponding transformer oil cooled winding, which is given in Fig. 4.5. The vertical axis title of Fig. 4.6(b), namely, the relative mass flow rate increment, is computed for each duct as:

$$p_2 = \frac{MFRD_{nf} - MFRD_f}{MFRD_f} \quad (4 - 20)$$

The changes in the maximum temperature-rise reduction of discs is explained and confirmed by the results of relative mass flow rate increment. In addition, based on the numerical results of the heat transfer coefficients, a similar curve as those shown in Fig. 4.6(a) can be plotted for the increments in heat transfer coefficients. It is found that quite close results are obtained by these two models for the thermal and fluidic field, hence the effectiveness of the numerical study is strengthened by mutual authentication.

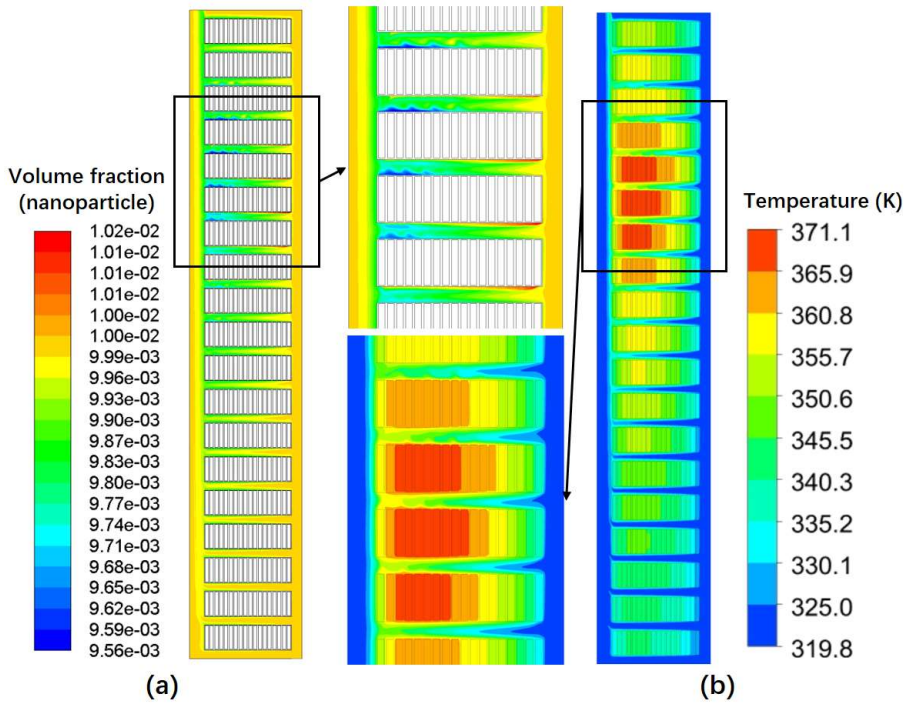


Fig. 4.7. (a) The distribution of nanoparticles volume fraction and (b) temperature contours derived by the mixture model for the pass with inlet on the outer vertical duct and nanofluid cooling.

Table 4.2. Mass Flow Rate Distribution.

Duct	$MFRD^P$	$MFRD^S$	$MFRD^M$	$p_2^S$	$p_2^M$
1	4.486	4.478	4.485	-0.18%	-0.03%
2	3.223	3.208	3.216	-0.45%	-0.20%
3	2.373	2.360	2.367	-0.55%	-0.23%
4	1.763	1.752	1.758	-0.62%	-0.25%
5	1.326	1.316	1.322	-0.71%	-0.26%
6	1.012	1.004	1.009	-0.81%	-0.30%
7	0.787	0.779	0.784	-0.95%	-0.37%
8	0.622	0.616	0.619	-1.12%	-0.50%
9	0.499	0.495	0.498	-0.98%	-0.36%
10	0.403	0.402	0.407	-0.30%	0.84%
11	0.327	0.329	0.332	0.79%	1.80%
12	0.261	0.273	0.273	4.59%	4.65%
13	0.191	0.224	0.218	17.28%	13.96%
14	0.147	0.187	0.172	27.34%	16.84%
15	0.147	0.172	0.158	17.19%	7.29%
16	0.186	0.203	0.195	9.09%	4.56%
17	0.303	0.290	0.294	-4.03%	-2.93%
18	0.437	0.417	0.420	-4.45%	-3.88%
19	0.623	0.606	0.601	-2.83%	-3.59%
20	0.885	0.889	0.873	0.44%	-1.37%
Sum	20.000	20.000	20.000		

For a clear illustration, the detailed mass flow rate distribution is listed in Table 4.2. The multi-phase mixture model, the single-phase model and the transformer oil are represented by these three superscripts  $M$ ,  $S$ , and  $P$ , respectively. Compared with the results of the multi-phase mixture model, the single-phase model gives larger  $MFRD$  increments in the ducts 13, 14, 15, and 16, through which the smallest  $MFRD$  flows. Hence, a better heat transfer performance in the vicinity of hot-spot locations is estimated by the single-phase model. However, the maximum difference in the heat transfer coefficient of disc is 1.7% for these two nanofluid models. The average flow velocity in the pass decreases slightly after adding nanoparticles, while the density of nanofluid, which is another variable included in the drag equation, increases. With the combined effect of these two parameters, the pressure drop through this pass decreases slightly after using the nanofluid (see Fig. 4.8).

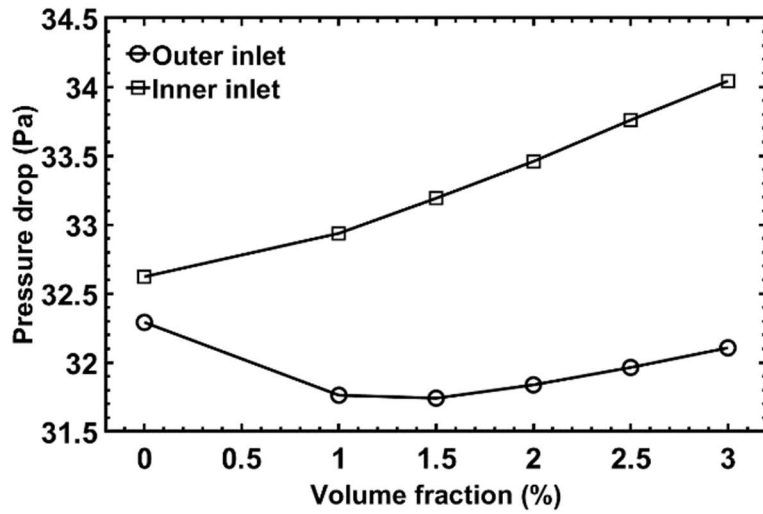


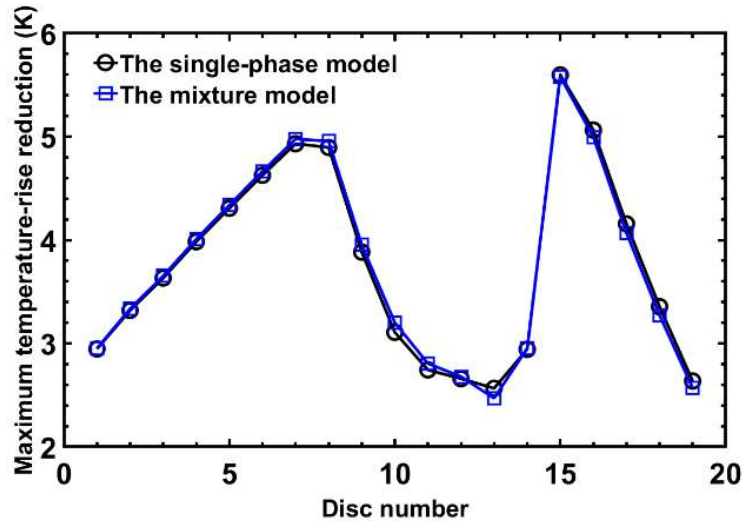
Fig. 4.8. Pressure drop of nanofluids in different volume fraction.

The volume fraction distribution of nanoparticles is obtained as well, since the conservation equation of volume fraction is included in the governing equations of mixture model. As shown in Fig. 4.7(a), there is a negative correlation between the nanofluid temperature and the concentration of nanoparticle. In the horizontal ducts, the outside temperature is much lower than the inside temperature, while the volume fraction has a downward trend from the outside of ducts to the inside of ducts.

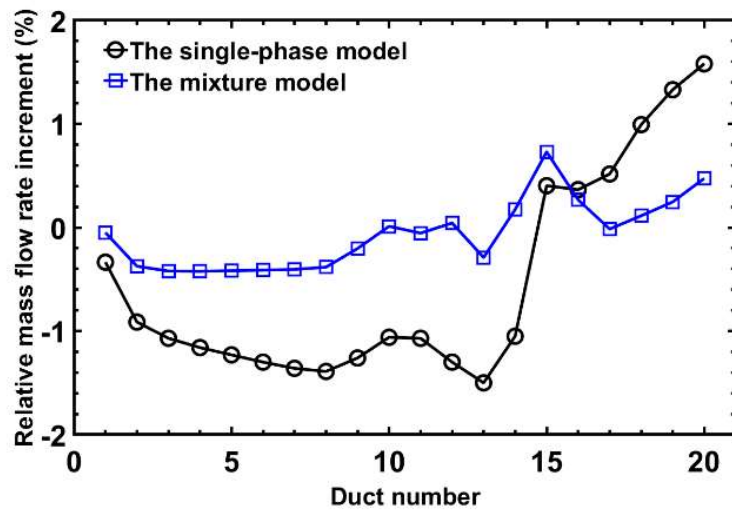
The nanofluid flow in the other pass is simulated and analyzed in the same manner. From the numerical results shown in Fig. 4.9(b), the effect that nanofluid has on the mass flow rate distribution is little, while the single-phase model derives a more pronounced solution. The differences between the heat transfer coefficients of discs calculated by these two models are less than 0.2%. Hence, the results of thermal field are roughly consistent for these two models, as shown in Fig. 4.9(a), and the improvement of thermal transfer performance is mainly generated by the enhanced thermal conductivity. Owing to the strong effect on density and the weak effect on flow field, the usage of nanofluid leads to a slight increase in the pressure drop through this pass (see Fig. 4.8).

Although the effect that nanofluids have on the flow fields is different, distinct temperature drops are generated by the enhanced thermal conductivity. In addition,

further improvement in the heat transfer performance may be produced by the adjusted mass flow rate distribution. The comparison of these two models strengthens the effectiveness of the numerical study by mutual authentication. In the following study one volume fraction, only the mixture model is considered, since it is reported to be more precise [D15, D16].

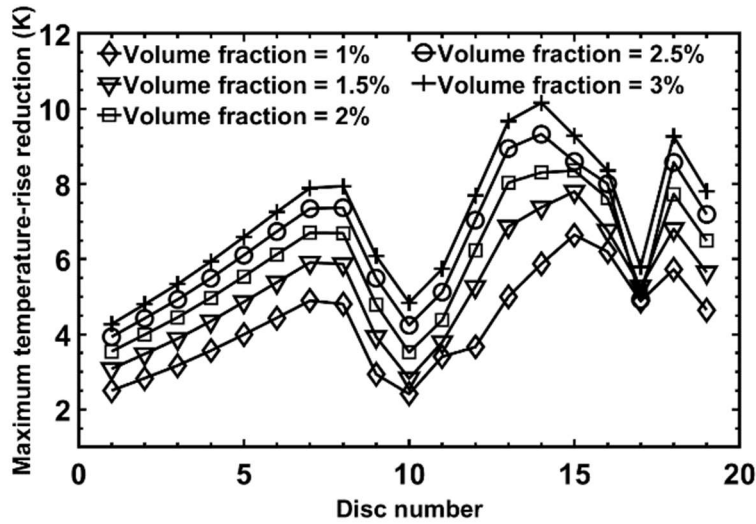


(a)

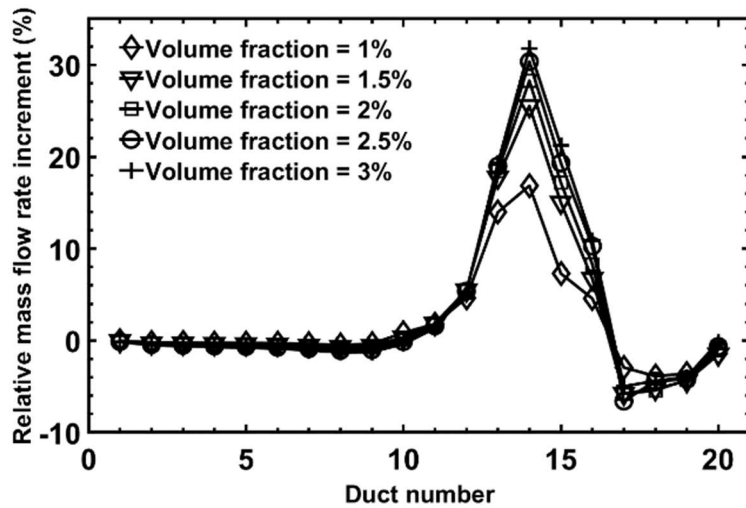


(b)

Fig. 4.9. (a) The maximum temperature-rise reduction and (b) relative mass flow rate increment for the pass with inlet on the inner vertical duct and nanofluid cooling.



(a)

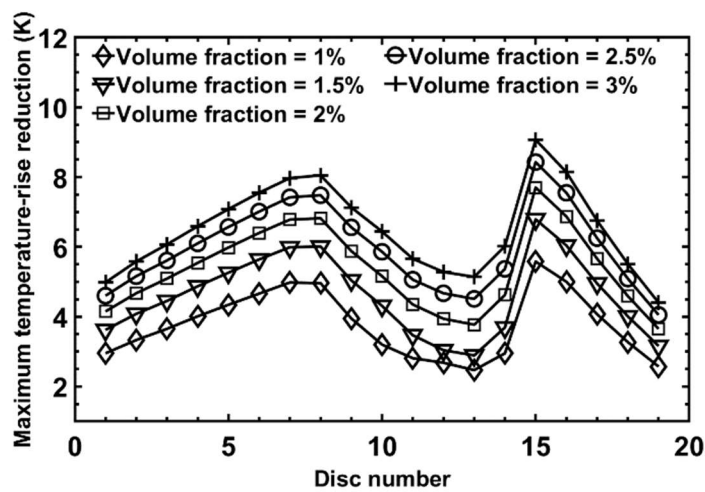


(b)

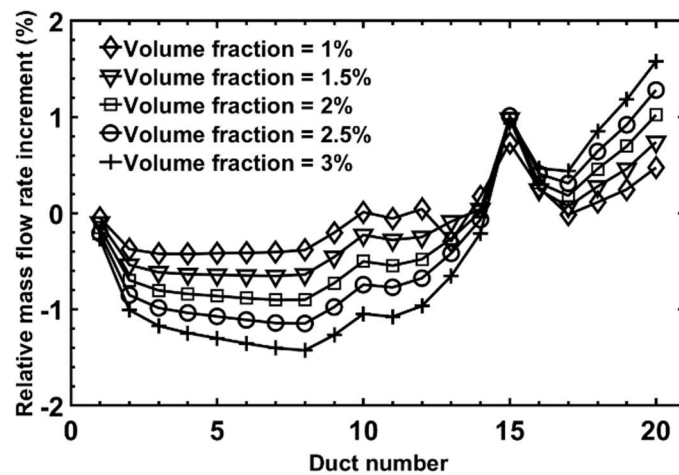
Fig. 4.10. (a) The maximum temperature-rise reduction and (b) relative mass flow rate increment for the pass with inlet on the outer vertical duct and cooled by nanofluids in different volume fraction.

In order to investigate the impact of volume fraction on the heat transfer performance, four more nanofluids with the concentration of 1.5%, 2%, 2.5%, and 3% are concerned in the study. Fig. 4.10 and Fig. 4.11 show the results of these four concentrations along with the results of 1% concentration for these two passes. The effect of nanofluids on the thermal and fluidic field is enhanced when increasing the volume fraction, while the overall tendency of these two evaluation parameters along the flow direction maintains. Hence, the correlation between the heat transfer

performance and the volume fraction is positive. A distinct drawback for increasing the volume fraction is the growing pressure drops (see Fig. 4.8), especially for the first pass. To compensate the increasing loss in the windings, more powerful pumps are needed. It can be concluded that all the variations in the thermal and fluidic field are correlated with the nanofluid properties, which are directly determined by the concentration of nanoparticles. To cope with the material cost and these mentioned factors, optimization algorithms combined with the numerical methods may be used to find the appropriate concentration for practical application.



(a)



(b)

Fig. 4.11. (a) The maximum temperature-rise reduction and (b) relative mass flow rate increment for the pass with inlet on the inner vertical duct and cooled by nanofluids in different volume fraction.

## 4.3 Numerical Study for the Entire Winding

In the former section, the convective heat transfer of nanofluid in disc-type windings are studied with the numerical model of one pass. Since the flows in adjacent passes are strongly coupled [D8], a complete numerical model, which contains all the passes of transformer windings, is built and simulated with the mixture model in this section. The solver, which is validated in the former section, is adopted.

### 4.3.1 The Numerical Model

As shown in Fig. 4.12, four passes divided by the oil washers are included in the low-voltage windings [D8]. All the passes, except the first one, contains 19 discs, and the first pass has an additional oil washer and 21 discs. With the commercial software package, we built a 2D and axisymmetric model for the low voltage windings. Like the numerical model for one pass, sticks and spacers are not concerned, and the insulation boards around the conductors are considered. For a better illustration, the passes, discs and horizontal ducts are numbered from the bottom to the top of the windings.

The cooled oil flows into the winding through these two inlets, and the oil is heated in the winding and then flows out from the outlet. Other circulation loops, such as the radiator, are excluded from the domain, and the boundary condition is obtained by the heat-run test. Hence, a complex heat transfer problem of the transformer is simplified to a simple convection problem in the windings. The inlet boundary condition is a homogeneous flow with the temperature  $319.85\text{ K}$  and the velocity of  $0.02695\text{ m/s}$ . The bottom surface of the first disc is specified with a convective boundary condition, and the heat transfer coefficient is  $100\text{ W m}^{-2}\text{ K}^{-1}$ . Other settings on the rest of the boundary conditions and the heat sources are identical to

those in section 4.2.

### 4.3.2 Results and Discussion

Before conducting the detailed analysis, the grid-independence is checked for this problem. The initial mesh, which is generated according to the criteria used in the former section, have about 4.7 million cells, and 26% extra cells are generated in the refined mesh after globally constraining the elements sizing. The difference in the disc average temperature is less than 1.1K, hence the initial mesh is feasible for this study.

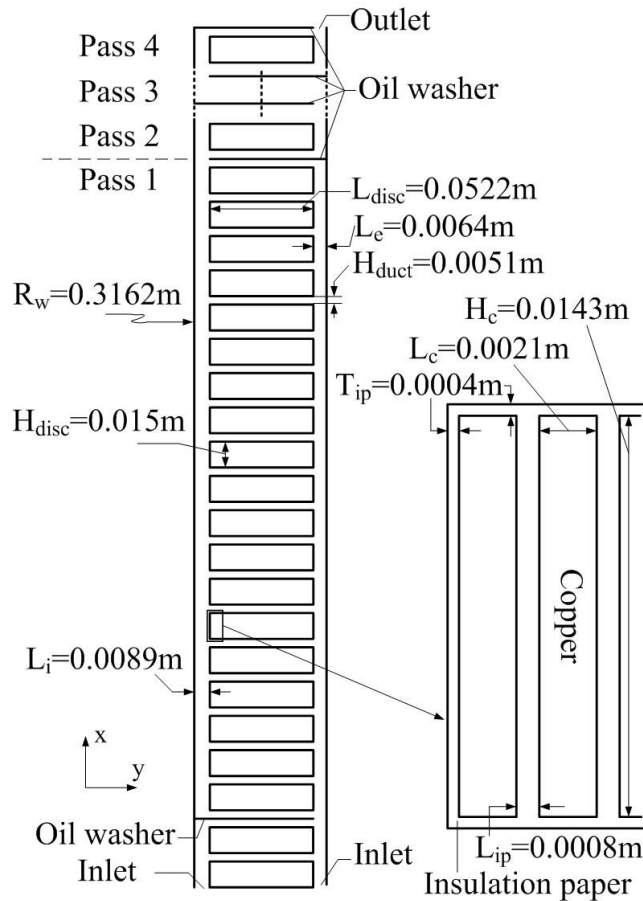


Fig. 4.12. The configuration of the low-voltage winding.

The temperature distribution of the nanofluid cooled winding is shown in Fig. 4.13, from which it is observed that the overall distribution is in good accordance with that of transformer oil cooled winding. In addition, the hot-spot location of the

winding is in the upper portions of pass three (see Fig. 4.14), which is also consistent with the result of transformer oil cooling. The variation trend of the disc temperature is directly related to the mass flow rate distribution, which is given in Fig. 4.15. From Fig. 4.13, it is observed that the inlet flows of pass 2 and pass 4 are inhomogeneous, and hot coolants flow into the ducts surrounding the bottom disc of these two passes. As a consequence, the first disc in these passes has a higher average temperature than the subsequent few discs.

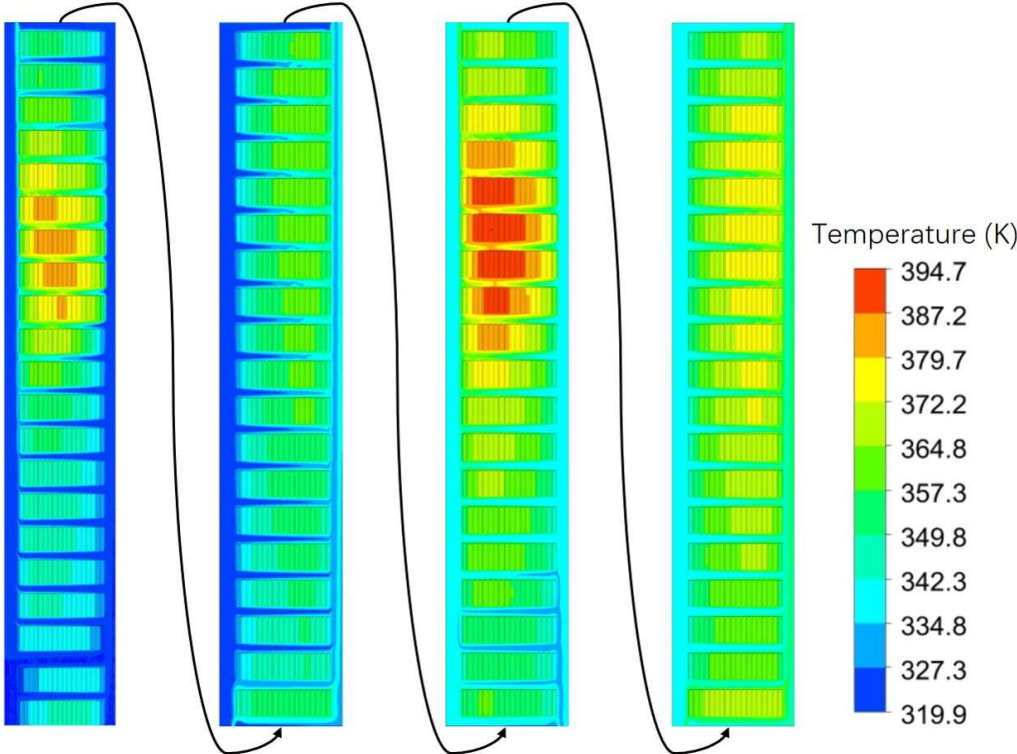


Fig. 4.13. The Contours of the temperature of the winding cooled by nanofluid.

As illustrated in Fig. 4.14, an overall temperature reduction is observed after using nanofluid. The variation in the heat transfer coefficient when compared to the coefficient in transformer oil cooled winding, as given in Fig. 4.16, is another reflection for the heat transfer performance improvement. The enhanced thermal conductivity is the main reason for the overall improvement, while the inhomogeneous temperature variation is produced by the effects that the usage of nanofluid has on the coolant temperature and the mass flow rate distribution. Since the variation of coolant

temperature is subtle in the first three passes, the related effects can be ignored.

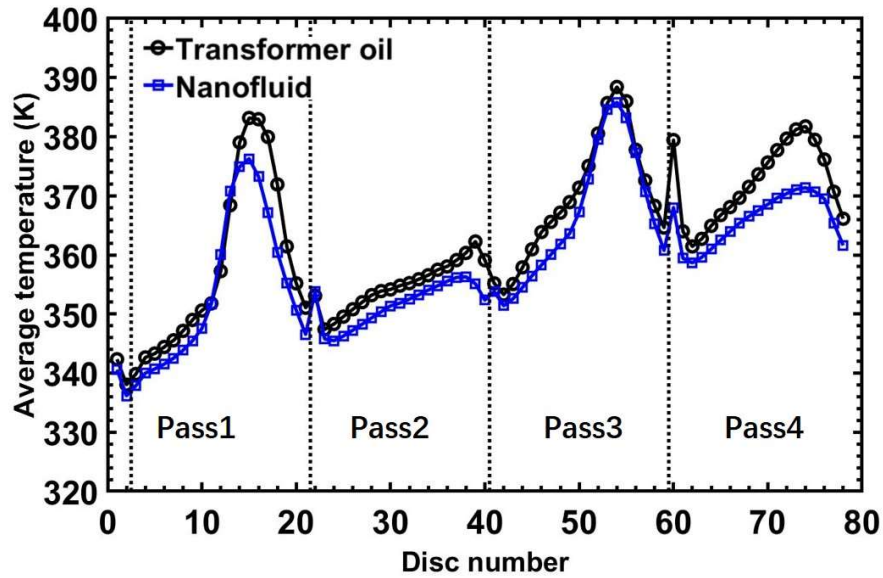


Fig. 4.14. The average disc temperature cooled by transformer oil and nanofluid.

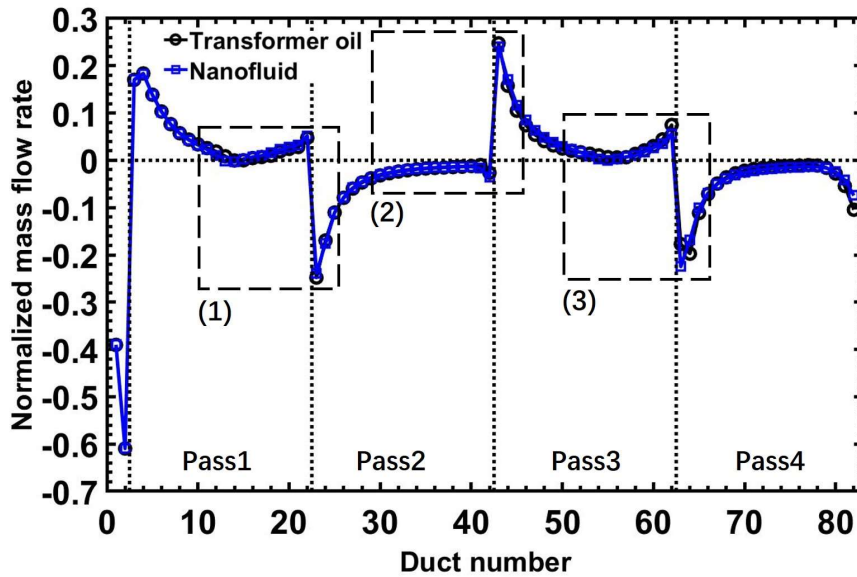


Fig. 4.15. The normalized mass flow rate through the horizontal ducts.

Overall, the variation in mass flow rate after using nanofluid is not appreciable (see Fig. 4.15), while the relative changes for those ducts with little mass flow rate are significant. For a better illustration, parts of the curves in Fig. 4.15, which are located in the dashed boxes, are enlarged and shown in Fig. 4.17. The mass flow rates in the middle ducts of pass one are reduced, while there are distinct increases in the mass

flow rates of the upper ducts. Since there is a positive correlation between the heat transfer coefficient and the mass flow rate, the temperatures of these corresponding discs vary reversely. For the remaining passes, the same analysis approach can be used. In addition, the heat transfer performance of pass four is further improved by the lower coolant temperature (see Fig. 4.14), and the maximum temperature-rise of this winding is reduced by 3.2K.

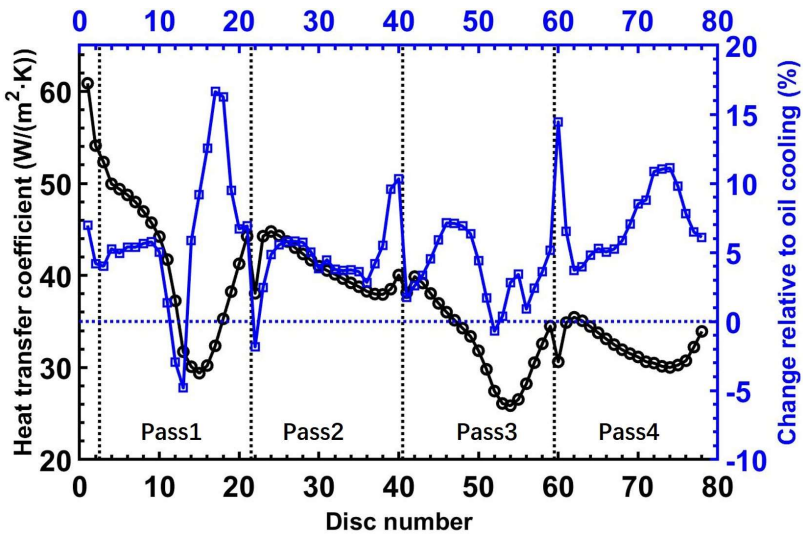


Fig. 4.16. The area-weighted average heat transfer coefficient of nanofluid cooling and its change relative to oil cooling.

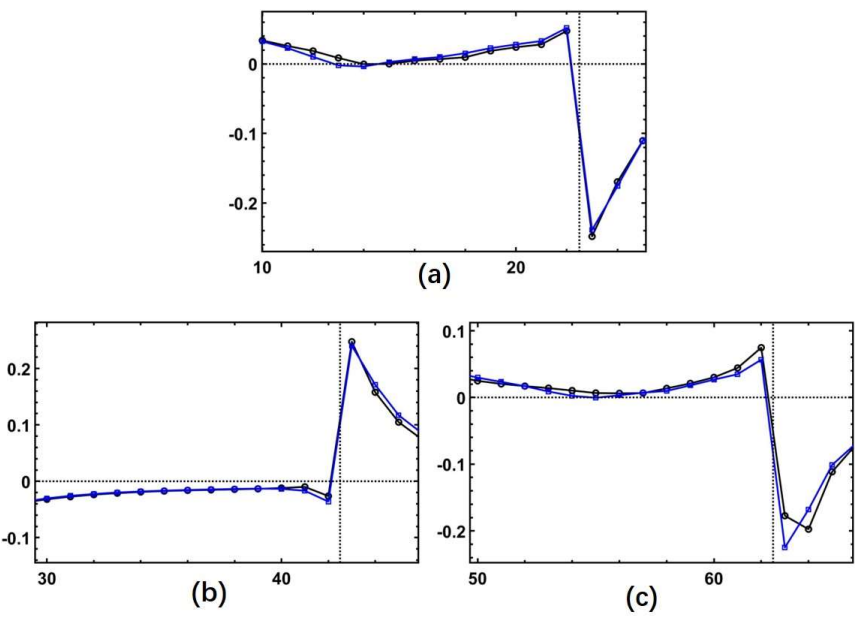


Fig. 4.17. The detailed mass flow rate at the joints of passes.

## 4.4 Experiment Study for the Nanofluid-filled Transformer

A single-phase transformer, which is rated at 500VA, 50Hz, and 220V/36V, are used to investigate the heat transfer performance of oil/ $\text{Al}_2\text{O}_3$  nanofluid. The experiment set up is shown in Fig. 4.18, and temperatures at eight points are measured (see Fig. 4.19). The experiment is conducted at rated and over-load conditions, and the heat transfer performance of nanofluid and transformer oil are compared. It takes roughly 9 hours for the transformer to reach a steady temperature (about  $50^\circ\text{C}$ ) after operation.

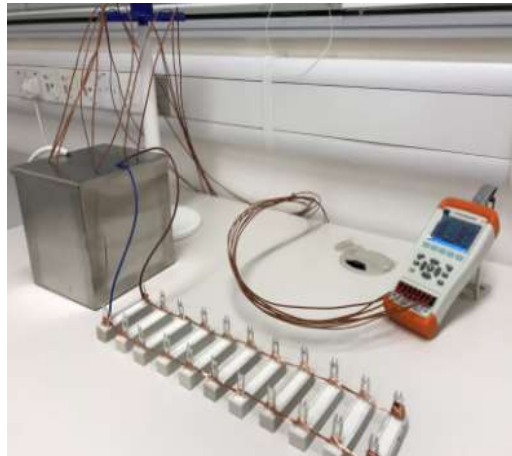


Fig. 4.18. The experiment set up for a nanofluid-filled transformer.

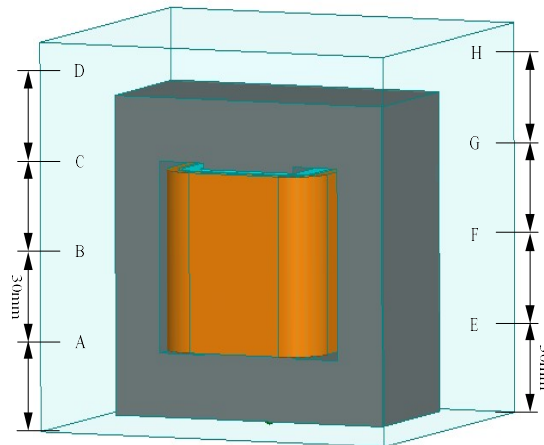


Fig. 4.19. The locations of thermocouples.

For these eight measurement points, the maximum temperature reduction after using nanofluid is 2.5 °C, while the corresponding value for rated condition is 1.8°C. The heat losses produced at over-load condition are increased when compared with the rated condition such that higher temperature rise of coolants is observed from the measured results. It can be concluded that the nanofluid has a better cooling capacity, and the performance of nanofluid can be enhanced to some extent with the increasing power.

## **4.5 Summary**

In this section, the convective heat transfer of nanofluid in disc-type windings is numerically studied by modelling one pass of the windings. Both the single-phase model and the multi-phase mixture model are used to represent the nanofluid, and results of these two models strengthen the effectiveness of the numerical study by comparison and mutual authentication. Despite of the varying effect of nanofluids on the flows, these two passes witness a distinct and comprehensive temperature drop after using the nanofluid. The heat transfer performance of nanofluid in the pass with inlet on the outer vertical duct is further enhanced by the ameliorative mass flow rate distribution. The effect of nanofluids on the thermal and fluidic field is enhanced by the increasing volume fraction of nanoparticles.

In addition, the entire winding is modelled to further investigate the convective heat transfer of nanofluid in disc-type windings. An overall reduction on the disc average temperature is observed after using nanofluids, while the temperature distribution along the flow direction is kept. Then enhanced thermal conductivity is the main reason for the heat transfer performance improvement, and the inhomogeneous temperature reduction of disc is produced by the variation of mass flow rate distribution. In addition, the effect of nanofluid is enhanced by the lower temperature in the fourth path.

## 4.6 Reference-Part D

- [D1] C. W. Group, "*Transformer Thermal Modelling*," CIGRE report, 2016.
- [D2] R. H. Gong, J. J. Ruan, J. Z. Chen, Y. Quan, J. Wang, and C. H. Duan, "Analysis and Experiment of Hot-Spot Temperature Rise of 110 kV Three-Phase Three-Limb Transformer," *Energies*, vol. 10, no. 8, Aug 2017.
- [D3] R. H. Gong, J. J. Ruan, C. B. Liao, L. Chao, and S. Jin, "3-D coupled electromagnetic-fluid-thermal analysis of 220kV three-phase three-limb transformer under DC bias," *2016 IEEE Conference on Electromagnetic Field Computation*, 2016.
- [D4] C. B. Liao, J. J. Ruan, C. Liu, W. Wen, and Z. Y. Du, "3-D Coupled Electromagnetic-Fluid-Thermal Analysis of Oil-Immersed Triangular Wound Core Transformer," *IEEE Trans. Magn.*, vol. 50, no. 11, Nov 2014.
- [D5] L. N. Li, S. X. Niu, S. L. Ho, W. N. Fu, and Y. Li, "A Novel Approach to Investigate the Hot-Spot Temperature Rise in Power Transformers," *IEEE Trans. Magn.*, vol. 51, no. 3, Mar 2015.
- [D6] F. Torriano, M. Chaaban, and P. Picher, "Numerical study of parameters affecting the temperature distribution in a disc-type transformer winding," *Appl. Therm. Eng.*, vol. 30, no. 14-15, pp. 2034-2044, Oct. 2010.
- [D7] F. Torriano, P. Picher, and M. Chaaban, "Numerical investigation of 3D flow and thermal effects in a disc-type transformer winding," *Appl. Therm. Eng.*, vol. 40, pp. 121-131, Jul. 2012.
- [D8] A. Skillen, A. Revell, H. Iacovides, and W. Wu, "Numerical prediction of local hot-spot phenomena in transformer windings," *Appl. Therm. Eng.*, vol. 36, pp. 96-105, Apr. 2012.
- [D9] R. Pendyala, S. U. Ilyas, L. R. Lim, and N. Marneni, "CFD Analysis of Heat Transfer Performance of Nanofluids in Distributor Transformer," *Proceeding of 4th International Conference on Process Engineering and Advanced Materials*, vol. 148,

pp. 1162-1169, 2016.

[D10] W. M. Guan et al., "Finite Element Modeling of Heat Transfer in a Nanofluid Filled Transformer," *IEEE Trans. Magn.*, vol. 50, no. 2, Feb 2014.

[D11] F. T. P. Picher, M. Chaaban, S. Gravel, C. Rajotte, B. Girard, "Optimisation of transformer overload using advanced thermal modeling," presented at *the CIGRE Conference*, Paris, France, 2010.

[D12] N. El Wakil, N. C. Chereches, and J. Padet, "Numerical study of heat transfer and fluid flow in a power transformer," *Int. J. Therm. Sci.*, vol. 45, no. 6, pp. 615-626, Jun. 2006.

[D13] V. Bianco, F. Chiacchio, O. Manca, and S. Nardini, "Numerical investigation of nanofluids forced convection in circular tubes," *Appl. Therm. Eng.*, vol. 29, no. 17-18, pp. 3632-3642, Dec. 2009.

[D14] M. Kalteh, A. Abbassi, M. Saffar-Avval, A. Frijns, A. Darhuber, and J. Harting, "Experimental and numerical investigation of nanofluid forced convection inside a wide microchannel heat sink," *Appl. Therm. Eng.*, vol. 36, pp. 260-268, Apr. 2012.

[D15] M. H. Fard, M. N. Esfahany, and M. R. Talaie, "Numerical study of convective heat transfer of nanofluids in a circular tube two-phase model versus single-phase model," *Int. J. Heat Mass Transf.*, vol. 37, no. 1, pp. 91-97, Jan. 2010.

[D16] R. Lotfi, Y. Saboohi, and A. M. Rashidi, "Numerical study of forced convective heat transfer of Nanofluids: Comparison of different approaches," *Int. J. Heat Mass Transf.*, vol. 37, no. 1, pp. 74-78, Jan. 2010.

[D17] W. Rashmi, A. F. Ismail, M. Khalid, and Y. Faridah, "CFD studies on natural convection heat transfer of Al<sub>2</sub>O<sub>3</sub>-water nanofluids," *Heat Mass Transfer.*, vol. 47, no. 10, pp. 1301-1310, Oct. 2011.

[D18] H. F. Oztop and E. Abu-Nada, "Numerical study of natural convection in partially heated rectangular enclosures filled with nanofluids," *Int. J. Heat Fluid Flow*, vol. 29, no. 5, pp. 1326-1336, Oct. 2008.

[D19] M. Manninen, V. Taivassalo, and S. Kallio, "On the mixture model for multiphase flow," *VTT Publications*, vol. 288, pp. 9-18, 1996.

[D20] A. N. L. Schiller, "A drag coefficient correlation," *Z. Ver. Deutsch. Ing.*, vol. 77, pp. 318–320, Jan. 1935.

[D21] Kalteh, A. Abbassi, M. Saffar-Avval, and J. Harting, "Eulerian-Eulerian two-phase numerical simulation of nanofluid laminar forced convection in a microchannel," *Int. J. Heat Fluid Flow*, vol. 32, no. 1, pp. 107-116, Feb. 2011.

# **Chapter 5 A Response Surface Optimization Method for Oil-immersed Transformer Cooling System Design**

In this chapter, a response surface optimization method is presented for the cooling system design of oil-immersed transformers. An accurate numerical simulation of the cooling system is realized firstly, based on which is a surrogate model is generated by the response surface method. With this surrogate model, the optimization efficiency is improved significantly, which is showcased with a numerical problem.

## **5.1 Introduction to the Optimization Methods Applied in Power Transformers Cooling System Design**

Analytical methods in combination with the specific coefficients developed for certain types of oil-immersed transformers are widely adopted in the cooling system design [E1]. This type of method is easily implemented and efficient in estimating the heat transfer capacity. However, these empirical coefficients are not universal and are difficult to acquire. The analytical methods have low accuracy when compared with numerical methods, and detailed results, such as the hot-spot temperature, are generally not be able to acquire by analytical methods.

With the development of computer technology and numerical methods, CFD have been introduced in the cooling system design of power transformers [E2-E6]. In the analysis process of heat transfer in transformers, several types of flow motions, such as laminar flow and turbulent flow, nonlinear material properties, temperature dependent parameters, and complex geometry may be encountered, and CFD can

handle all these circumstances and gives the detailed results of fields. CFD analysis is applied either in the optimization of entire cooling system or in optimizing certain section of transformers. In order to optimize the cooling system of a step-down 3-phase oil-immersed power transformer, a numerical model is built for one section containing a core and the wounded two windings, and six configurations with six inlet boundary conditions are studied [E3]. The active parts are however not included in the computational domain. In [E4], the cooling capacity of an ONAN power transformer radiator is determined by numerical simulation, and the section length and the space between sections are optimized. Compared with the existing design, the cooling capacity of the optimized radiator is improved by 14%. To minimize the hot-spot temperature rise in windings, the active parts is included in the computational domain and is solved along with the flow field. Based on a validated CFD model, the dimensions of cooling ducts and coils of an ANAN power transformer are optimized simultaneously using the Genetic Algorithm (GA) [E5, E6]. The power losses used in the thermal analysis are derived by a coupled CFD-electromagnetic model for each configuration. The optimized result indicates that the heat transfer performance can be improved by the nonuniform positioning of cooling ducts and coils. According to the literatures, it is found that the CFD analysis of power transformers requires enormous computational resources due to the high nonlinearity and the large scale mesh, and this limits its extensive applications in the optimization.

Response surface methods (RSMs) are introduced to many engineering problems, such as thermal analysis of multichip module [E7, E8], material properties prediction [E9], bidirectional flow passage components design [E10], and electromagnetic device design [E11, E12], to generate surrogate models, which are used to replace the numerical models in optimization. Hence, the RSMs are generally used in combination with optimization methods. The training data used in the RSMs are obtained by measurement or numerical simulation based on the design of experiment. Compared with the direct optimization method based on numerical model, the efficiency of RSM based optimization method is dramatically improved, while the sacrifice on accuracy is few.

## 5.2 The Response Surface Optimization Method

Two types of RSMs, namely, the Kriging method and the second order polynomial (SOP) method [12] [13], are introduced into the optimization process to produce the surrogate model. The CFD model, which is used to generate the training points for RSMs, is built firstly, and the grid independence of the simulation is verified. The surrogate model with smaller prediction error is incorporated in the optimization and the optimized result of a numerical problem is compared with the result of a direct optimization method to evaluate the performance of the proposed method.

### 5.2.1 CFD Modeling

The numerical problem is to optimize a three-phase OFAN transformer, which is rated at 30MW, 60 Hz, and 115-13.8kV. To reduce the computation burden, the transformer body is isolated from the external oil circulation path, such as the chillers, and the insulation boards and structural parts are neglected. Based on these simplifications, the CFD model of the initial design of this transformer is built, as shown in Fig. 5.1. Owing to the symmetry geometry, only half of the transformer is concerned with the middle section imposed on symmetry boundary conditions. Since the majority of heat in OF transformer is taken away by the heated oil, the heat radiation is neglected in the numerical model. The tank surface is specified with a fixed convective coefficient of  $5W/(m^2 \cdot K)$ , and the ambient temperature is assumed to be fixed at 293K. In addition, the inlet boundary condition is isothermal flow with the temperature of 293K and the velocity of 0.5m/s.

The losses are obtained at rated condition, and the losses distribution is assumed to be homogeneous in each part. The stray losses in the transformer are neglected. The heat density (HD) of these three active parts are listed in Table 5.1 along with the

corresponding material properties, i.e. density, specific heat capacity (SHC), thermal conductivity (TC). In addition, the properties of transformer oil, which are assumed to be temperature independent, are also included in Table 5.1.

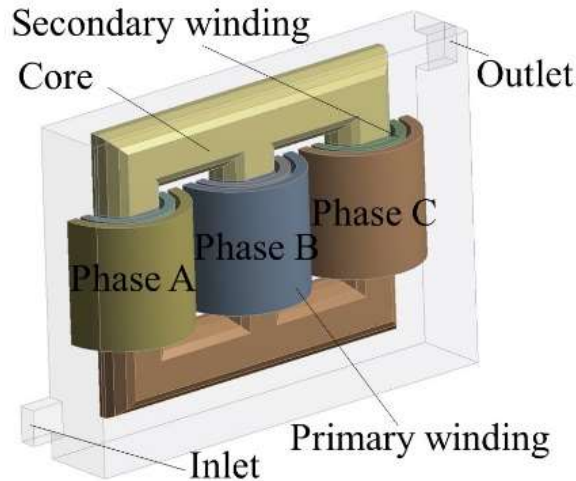


Fig. 5.1. The CFD model of the oil-immersed transformer.

Table 5.1 Material properties.

Part	Density <sup>a</sup> <i>kg/m<sup>3</sup></i>	SHC <sup>b</sup> <i>J/(kg · K)</i>	HD <sup>c</sup> <i>W/m<sup>3</sup></i>	TC <sup>d</sup> <i>W/(m · K)</i>	Viscosity <sup>e</sup> <i>Pa · s</i>
Core	7850	480	7000	50	-
Primary winding	8900	390	33320	250	-
Secondary winding	8900	390	44835	250	-
Oil	912.8	1621	-	0.15454	0.033396

It is well recognized that the results of CFD analysis are dramatically influenced by the mesh quality, and totally wrong solutions or convergence problems may be generated by a poor quality mesh. In addition, different fluid motions have distinctive requirements for the mesh quality. The Reynolds number is calculated to determine the fluid motion of the studied flow. The calculated Reynolds number is much larger than 4000, hence the oil flow in the transformer is turbulent. To deal with the viscous sublayer, in which turbulence is not fully developed, the mesh of fluid near wall surfaces is refined with hexahedron elements, as shown in Fig. 5.2(b). In addition, extra turbulent models are required to model the turbulence, and the standard k-epsilon

model is adopted in combination with the standard wall function. Except the general governing equations, two more equations related to turbulence are introduced by this model.

The Semi-Implicit Method for Pressure-Linked Equations (SIMPLE) scheme is used to solve the CFD problem with the convergence criterion specified for the energy equation and other governing equations as  $1.0 \times 10^{-5}$  and  $1.0 \times 10^{-3}$ , respectively. In addition, the temperature changes are concerned to monitor the convergence. When the transformer reaches the thermal equilibrium, the generated heat is equal to the dissipated heat, and the temperature of transformer is stable. The derived results should satisfy the conservation laws, such as the inlet-outlet mass flow. Moreover, the grid independence of the results is verified with refined meshes.



Fig. 5.2. Mesh of (a)core, windings, and (b) oil.

Table 5.2. Details of the mesh.

Object name	Element type	No. of element
Oil	Hexahedron, Tetrahedron	822636
Core	Tetrahedron	46138
Primary winding (A)	Tetrahedron	80959
Secondary winding (A)	Tetrahedron	89795
Primary winding (B)	Tetrahedron	82112
Secondary winding (B)	Tetrahedron	90072
Primary winding (C)	Tetrahedron	80712
Secondary winding (C)	Tetrahedron	90368

## 5.2.2 RSM and Optimization

Several types of RSMs, which are based on different algorithms, have been proposed, such as the regression method, neural network, space grid, Kriging and so on. For the transformer cooling problems, two types of RSMs, namely, the SOP method and the Kriging method, are tested and compared on the performance in this thesis. The SOP method is efficient in extracting the nonlinear characteristics from training data, and the Kriging method combines the regression model with extra corrections.

The general function for the SOP model [12] is formulated as

$$V = \alpha_0 + \sum_{i=1}^n \alpha_i x_i + \sum_{i=1}^n \alpha_{ii} x_i^2 + \sum_{i \neq j}^n \alpha_{ij} x_i x_j \quad (5-1)$$

where;  $x_i$  and  $V$  are the  $i^{th}$  design variable and the function of interest, respectively;  $\alpha$  is the polynomial coefficient;  $n$  is the number of design variables. The polynomial coefficients are calculated by the least-square regression with a set of design points. For a set in size of  $k$ , the equation (5-1) is rewritten as

$$\begin{pmatrix} V_1 \\ V_2 \\ \vdots \\ V_k \end{pmatrix} = \begin{pmatrix} 1 & x_{11} & \dots & x_{1n} & x_{11}^2 & \dots & x_{1n}^2 & x_{11}x_{12} & \dots & x_{1n}x_{1n-1} \\ 1 & x_{21} & \dots & x_{2n} & x_{21}^2 & \dots & x_{2n}^2 & x_{21}x_{22} & \dots & x_{2n}x_{2n-1} \\ \vdots & \vdots & \dots & \vdots & \vdots & \dots & \vdots & \vdots & \dots & \vdots \\ 1 & x_{k1} & \dots & x_{kn} & x_{k1}^2 & \dots & x_{kn}^2 & x_{k1}x_{k2} & \dots & x_{kn}x_{kn-1} \end{pmatrix} \cdot \{\alpha_0 \quad \alpha_1 \quad \dots \quad \alpha_n \quad \alpha_{11} \quad \dots \quad \alpha_{nn} \quad \alpha_{12} \quad \dots \quad \alpha_{nn-1}\}^T + \begin{pmatrix} \varepsilon_1 \\ \varepsilon_2 \\ \vdots \\ \varepsilon_k \end{pmatrix} \quad (5-2)$$

or

$$\mathbf{V} = \mathbf{x}\boldsymbol{\alpha} + \boldsymbol{\varepsilon} \quad (5-3)$$

where  $\boldsymbol{\varepsilon}$  is the error matrix. The coefficient matrix is derived by the following formula when the 2-norm of  $\boldsymbol{\varepsilon}$  is minimized

$$\boldsymbol{\alpha} = (\mathbf{x}^T \mathbf{x})^{-1} \mathbf{x}^T \mathbf{V} \quad (5-4)$$

The Kriging method [13] was proposed for geological problems and have been applied in many areas. In this method, the regression model is combined with local derivation as

$$V = f(x) + z(x) \quad (5 - 5)$$

where;  $f(x)$  is a polynomial equation;  $z(x)$  is the local derivation, which is derived by accomplishing a normally distributed Gaussian random process with zero mean,  $\sigma^2$  variance, and nonzero covariance. Hence the derived surrogate model is accurately fitted to all the design points, and the prediction error is zero for design points. The local derivation is formulated as

$$z(x) = \sum_{i=1}^k \lambda_i \gamma(x^i, x) \quad (5 - 6)$$

where;  $\gamma$  is the Gaussian correlation function;  $\lambda$  is the weighting coefficient. It is concluded that the global behavior is represented by the polynomial equation while the local characteristic is indicated by the derivation.

The initial design points, which are used as the training data for the RSMs, are chosen from the design space by the central composite design (CCD) method, and are solved by the CFD solver. Generally, the precision of the surrogate model derived based on the initial design points is low, and more refinement points are required to improve the precision. The performance of the surrogate model is estimated by comparing the predicted results and the numerical results of the verification points. The root mean square error (RMSE) and the coefficient of determination (CoD) are two common estimation parameters. Once an accurate surrogate model is obtained, the subsequent optimization is readily to implement and the time consumed is negligible.

Since excessive temperature rise accelerates the aging of insulating materials and reduces the transformer service life, the reduction of maximum temperature rise is taken as the optimization objective. Five continuous and independent design variables are included in the optimization, i.e. (1) the gap between the top surface of tank and the core center (P1, 1.35m-1.50m), (2) the gap between the undersurface of tank and

the core center (P2, 1.35m-1.50m), (3) the gap between the left side surface of tank and the core center (P3, 1.85m-2.00m), (4) the gap between the right side surface of tank and the core center (P4, 1.85m-2.00m), and (5) half thickness of the tank (P5, 0.65m-0.80m). To validate the effectiveness of the response surface optimization method, the direct optimization is conducted with the CFD model. Since the generation and the computation of surrogate model are not time-consuming, the number of CFD analysis is adopted to estimate the efficiency.

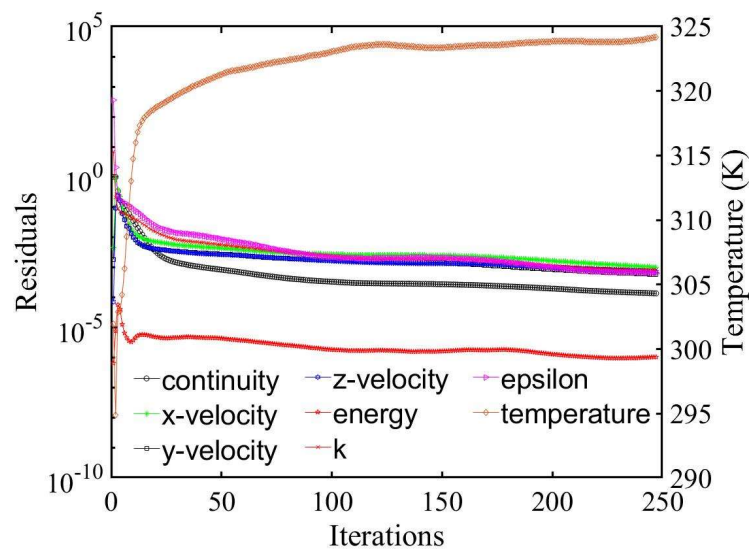


Fig. 5.3. The calculated residuals and temperature at origin.

### 5.2.3 Solutions of the Original Transformer

Before conducting the optimization process, the original transformer is solved firstly, and the grid-independence of the simulation is verified. The residuals of the governing equations are monitored along with the temperature at the center of core, as shown in Fig. 5.3. The nonlinear problem takes 247 iterations to converge, and the monitored temperature has stabilized at 324K. The temperature distribution of this transformer is given in Fig. 5.4(A), from which it is found that the hot spot is located in the upper middle of secondary windings. In addition, the conservation between the generated heat and the dissipated heat is verified. Two refined meshes, which have

1627743 elements and 1691506 elements respectively, are generated by constraining the element sizing globally, and the temperature distributions derived based on these two meshes are in good agreement with the results of the initial mesh, as shown in Fig. 4. Hence, the initial mesh is feasible for this specific problem.

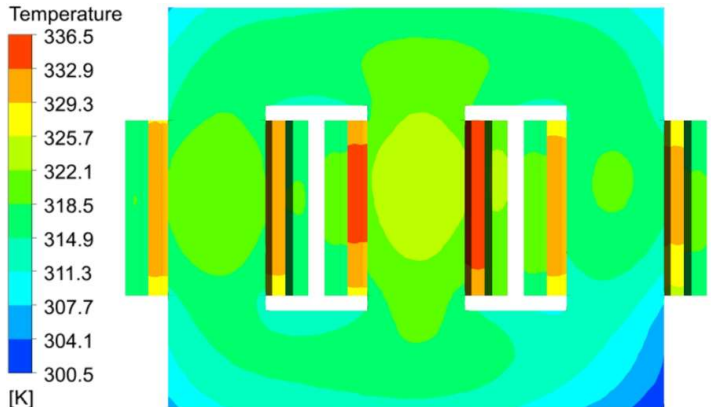
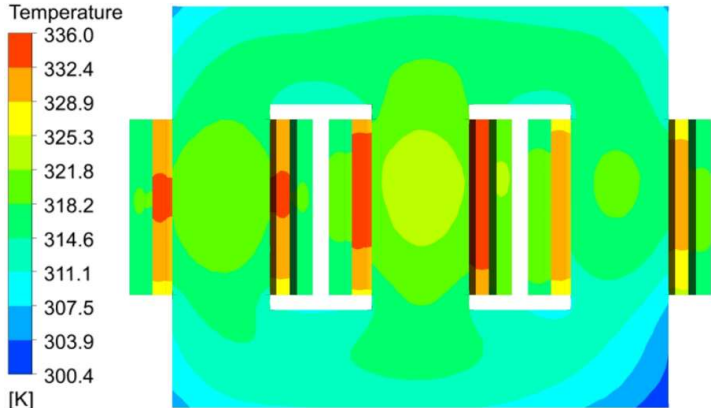
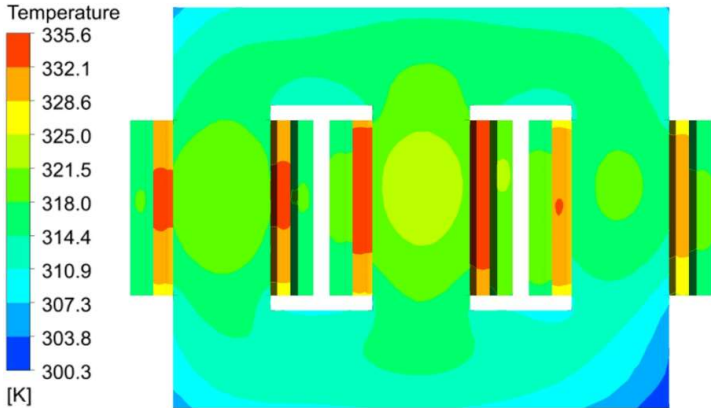


Fig. 5.4. The calculated temperature of active parts with (a) the first mesh, (b) the second mesh, and (c) the last mesh.

## 5.2.4 Analysis of RSMs and Optimization Results

With the CCD method, 27 initial design points are generated for this optimization problem with five design variables. The initial surrogate models are produced with these two RSMs, and both these two models have large forecast errors. Hence 35 refinement points are gradually added to the design point set to improve the performance of surrogate model, and two more surrogate models are obtained finally. The goodness of fit of these two SOP models is given in Fig. 5.5(a) and (b), from which it is found that the distribution of design points on either side of the centerline is almost average. As introduced in the former section, the Kriging model fits the design points perfectly, as shown in Fig. 5(c) and (d). Since the derivations used in the Kriging method can characterize the local behavior, the Kriging method is expected to generate more accurate models, and this is validated by the comparison of the goodness of fit of these four models produced by these two RSMs. In addition, the RSMs of the SOP models are always larger than that of the Kriging model, as listed in Table 5.3. Compared with the initial surrogate models, the precision of the final surrogate models is improved. The RMSE of the surrogate model produced by the Kriging method is reduced from 0.76K to 0.43K.

Table 5.3. Error analysis of the surrogate models.

Method	Point Set	CoD	RMSE
SOP	Design points	0.775/0.803 <sup>a</sup>	0.76/0.87
	Verification points	-	0.84/0.53
Kriging	Design points	1/1	2.6E-8/5.2E-7
	Verification points	-	0.76/0.43

<sup>a</sup>Data in front of and behind the slash are the values for response surfaces before and after adding refinement points, respectively.

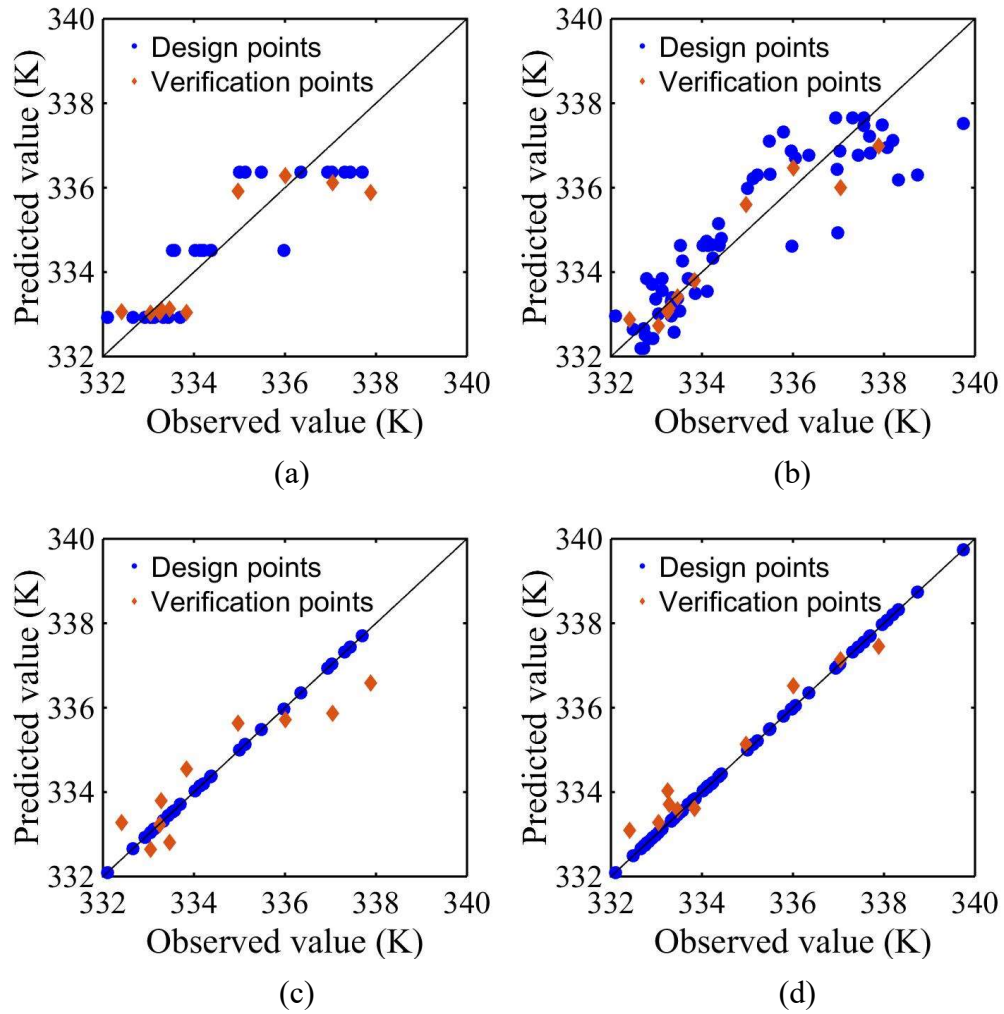


Fig. 5.5. Goodness of fit for (a) the initial SOP model, (b) the final SOP model, (c) the initial Kriging model (d) the final Kriging model.

Table 5.4. Optimized solutions.

Method	P1/m	P2/m	P3/m	P4/m	P5/m	T/K	No. <sup>a</sup>
RSM	1.37	1.42	1.85	1.98	0.65	332.5	62+10 <sup>b</sup>
Direct	1.49	1.42	1.86	1.97	0.66	332.2	120

<sup>a</sup>No. represents the No. of CFD analysis.

<sup>b</sup>10 is the number of CFD analysis for final validation.

Based on the final Kriging model, the problem is optimized by the screening method. The optimization generates ten candidates, and CFD analysis is invoked to verify these candidates, based on which the optimized solution is selected. Meanwhile,

a direct optimization is conducted by the adaptive single-objective method combined with the CFD model. The optimized solutions derived by these two methods are listed in Table 5.4. It is found that there is a large discrepancy between the first variable P1 of these two optimized solutions. A sensitivity analysis of this variable is conducted with the response surface. P1 varies with a small interval of  $6.25E-3m$ , while other four variables are fixed at the dimensions given in Table 5.4. 25 cases are generated based on the strategy, and the maximum discrepancy among the calculated object functions of these cases is 0.5 degree centigrade. It could be concluded that the correlation between the objective function and the first variable is weak. In addition, the temperature distributions in the active parts are almost identical for these two optimized solutions, and a small net error, about 0.04 degree centigrade, is obtained for the average temperature of active parts. The time consumed by the proposed optimization method is roughly 60% of that consumed by the direct method.

### **5.3 Summary**

Based on the accurate numerical modelling of oil-immersed transformers and the CCD method, surrogate models are produced by the SOP method and the Kriging method. The Kriging model, which is validated to be more accurate, is used in the RSM based optimization process. Direct optimization method combined with the CFD model is conducted for comparison, and the effectiveness of the proposed response surface optimization method is showcased by an oil-immersed transformer optimization problem.

## 5.4 Reference-Part E

- [E1] Shenyang Transformer LLC. *Design handbook of oil-immersed power transformer*. Shenyang: Shenyang Transformer LLC, 1999, pp. 162-203.
- [E2] L. N. Li, S. X. Niu, S. L. Ho, W. N. Fu, and Y. Li, "A novel approach to investigate the hot-spot temperature rise in power transformers," *IEEE Trans. Magn.*, vol. 51, no. 3, Mar 2015.
- [E3] N. El Wakil, N. C. Chereches, and J. Padet, "Numerical study of heat transfer and fluid flow in a power transformer," *Int. J. Therm. Sci.*, vol. 45, no. 6, pp. 615-626, Jun. 2006.
- [E4] S. Anishek, R. Sony, K. J. Jayadeep, and P. M. Kamath, "Performance Analysis and Optimisation of an Oil Natural Air Natural Power Transformer Radiator," *International Conference on Emerging Trends in Engineering, Science and Technology*, vol. 24, pp. 428-435, 2016.
- [E5] J. Smolka and A. J. Nowak, "Shape optimization of coils and cooling ducts in dry-type transformers using computational fluid dynamics and genetic algorithm," *IEEE Trans. Magn.*, vol. 47, no. 6, pp. 1726-1731, Jun 2011.
- [E6] J. Smolka, "CFD-based 3-D optimization of the mutual coil configuration for the effective cooling of an electrical transformer," *Appl. Therm. Eng.*, vol. 50, no. 1, pp. 124-133, Jan 2013.
- [E7] H. C. Cheng, W. H. Chen, and I. C. Chung, "Integration of simulation and response surface methods for thermal design of multichip modules," *IEEE Trans. Compon. Packag. Technol.*, vol. 27, no. 2, pp. 359-372, Jun 2004.
- [E8] Y. J. Cheng, G. W. Xu, D. P. Zhu, W. J. Zhu, and L. Luo, "Thermal analysis for indirect liquid cooled multichip module using computational fluid dynamic simulation and response surface methodology," *IEEE Trans. Compon. Packag. Technol.*, vol. 29, no. 1, pp. 39-46, Mar 2006.
- [E9] M. Hemmat Esfe, M. H. Hajmohammad, P. Razi, M. R. H. Ahangar, and A. A. Arani, "The optimization of viscosity and thermal conductivity in hybrid nanofluids

- prepared with magnetic nanocomposite of nanodiamond cobalt-oxide (ND-Co<sub>3</sub>O<sub>4</sub>) using NSGA-II and RSM," *Int. Commun. Heat Mass*, vol. 79, pp. 128-134, Dec 2016.
- [E10] X. P. Gao, Y. Tian, and B. W. Sun, "Multi-objective optimization design of bidirectional flow passage components using RSM and NSGA II: A case study of inlet/outlet diffusion segment in pumped storage power station," *Renew. Energ.*, vol. 115, pp. 999-1013, Jan 2018.
- [E11] L. Jolly, M. A. Jabbar, and Q. H. Liu, "Design optimization of permanent magnet motors using response surface methodology and genetic algorithms," *IEEE Trans. Magn.*, vol. 41, no. 10, pp. 3928-3930, Oct 2005.
- [E12] X. Y. Liu and W. N. Fu, "A dynamic dual-response-surface methodology for optimal design of a permanent-magnet motor using finite-element method," *IEEE Trans. Magn.*, vol. 52, no. 3, Mar 2016.
- [E13] S. An, S. Yang, and O. A. Mohammed, "A Kriging-Assisted Light Beam Search method for multi-objective electromagnetic inverse problems," *IEEE Trans. Magn.*, vol. 54, no. 3, Mar 2018.

# Chapter 6 Conclusion and Future Work

## 6.1 Conclusion

In order to tackle the existing problems in transformer cooling, the transformer analysis and design method are investigated along with the novel coolants, nanofluids. An adaptive DoFs FEM solver is developed for the 3D nonlinear magnetic field analysis, thermal field analysis, and coupled magneto-thermal field analysis, and coupled analysis is based on the independent solvers for magnetic field and thermal field. In the adaptive DoFs FEM, the system reduction is realized by eliminating the redundant DoFs from the unknown list rather than removing the corresponding nodes. Hence the rearrangement of mesh data and the storage space for the former mesh are avoided. The slave-master technique is used in the elimination process in combination with the constraint proposed for 3D field. One set of FEM mesh is used in the coupled magneto-thermal analysis to build the FE spaces of these two fields, and the DoFs in each field are adjusted separately according to the field's requirement in discretization. Hence, the different discretization requirements of these two fields are met with one set of mesh, and the mapping algorithms for different meshes are no longer needed. Several numerical examples are solved to showcase the effectiveness of this method in terms of efficiency and accuracy.

Winding is the common hot-spot location in transformers, and the hot-spot temperature rise in transformers is critical for the safe operation. In order to apply this novel coolant, i.e. nanofluid, in transformer cooling, the convective heat transfer of oil/SiC nanofluid in disc-type transformer windings is numerically investigated. The numerical model and method used in the study is validated with the existing results of oil cooled transformer windings. One pass of the winding is modelled numerically, in which the changes in inlet position are concerned. This is the first time to employ the

multi-phase mixture model to analyze such a nanofluid field, and the single-phase model is also used for comparison and mutual authentication. Although the effects that the oil/SiC nanofluid of 1% concentration has on the flows in windings vary, comprehensive temperature drop over these two passes is observed after using the nanofluid. For the pass with inlet in the internal vertical duct, the heat transfer performance is further improved by the ameliorative mass flow rate distribution. In addition, there is a positive relation between the volume fraction of nanoparticles and the effect on the thermal and fluidic field. To further investigate the nanofluid flow in disc-type transformer windings, a numerical mode is built for the entire winding. The results show that there is an overall reduction on the disc average temperature after adding nanoparticles, and the temperature distribution along the flow direction is maintained. It can be concluded that the heat transfer improvement is mainly produced by the enhanced thermal conductivity, and the changes in mass flow rate distribution produce the inhomogeneous temperature reduction of discs. In addition, the lower coolant temperature enhances the effect of nanofluid in the fourth pass.

A response surface optimization method is proposed for the cooling system design of oil-immersed transformers. Based on the accurate numerical modeling and the CCD method, surrogate models to be used in the optimization are produced by these two adopted response surface methods, the SOP method and the Kriging method. Refinement points are gradually added into the set of design points until the derived surrogate models meet the predefined criterion. The surrogate model obtained with the Kriging method, which is validated to be more accurate, is adopted in the response surface optimization process, and the direct optimization method combined with the CFD model is also adopted for comparison. An oil-immersed transformer optimization problem is employed to showcase the effectiveness of the proposed method.

## **6.2 Future Work**

Since fluid coolants are involved in many devices, more accurate field can be

obtained when the fluid field is concerned in the analysis. Hence, the adaptive DoFs FEM can be further extended to solve the coupled magneto-thermal-fluidic field. In this coupled analysis, the thermal interaction between solid and liquid parts should be handled. In addition, the fluid field solver should be developed according to the flow characteristics, such as laminar flow, turbulent flow, single-phase model, and multi-phase flow. In order to further improve the computation efficiency, other numerical techniques, such as domain decomposition methods, model order reduction methods, and machine learning algorithms, can be introduced into the adaptive method.

Based on the numerical analysis of transformers, co-design method for the electromagnetic, thermal and insulation design can be developed. Since the numerical analysis process is time-consuming and massive design points need to be estimated, surrogate model can be introduced into the optimization to improve design efficiency. In addition, the emerging artificial methods, such as deep learning, can be applied in the rapid field calculation.

In order to accurately reflect the reality, 3D models should be developed for the nanofluid cooled transformer. In addition, different types of transformers or transformers under different operation status should be investigated. Except the thermal properties, other properties of oil based nanofluids, such as dielectric characteristics, breakdown voltage, will be studied based on the transformer application. The effect of volume fraction and nanoparticle should be included in the study. To promote the industrial application, efficient nanofluids preparation method should be developed.